The role of the electrolyte on the lithium-sulfur battery electrochemistry

Zur Erlangung des akademischen Grades eines

DOKTORS DER NATURWISSENSCHAFTEN

(Dr. rer. nat.)

von der KIT-Fakultät für Chemie und Biowissenschaften

des Karlsruher Instituts für Technologie (KIT)

genehmigte

DISSERTATION

von

Herrn Lucas Lodovico

1. Referent: Prof. Dr. Stefano Passerini
2. Referent: Prof. Dr. Helmut Ehrenberg
Tag der mündlichen Prüfung: 10. Dezember 2018

Chaos is order yet undeciphered
Saramago, J.

Aos Meus

Abstract

Sulfur has attracted great attention due to its potential application as high-energy cathode material in next generation batteries. Sulfur is environmentally friendly, abundant, and possess very high theoretical capacity, around 1675 mAh g^{-1}. The chemistry and electrochemistry of sulfur, however, are much more complicated than those of the commonly used insertion materials for lithium-ion batteries. The reduction of sulfur in lithium-sulfur cells happens through a multi-step mechanism involving chemical disproportionation reactions leading to the formation of multiple soluble intermediaries as well. Solubilization of the active material is very detrimental to the cell, since it unavoidably leads to capacity loss. This also means that in Lithium-Sulfur batteries the electrolyte plays a key role beside the simple ion carrier.

In this thesis, the decomposition of the state-of-the-art electrolyte for lithium-sulfur batteries is studied, which is shown to have a great impact on the sulfur electrochemistry. In the first part, the effect of electrolyte decomposition due to the presence of oxygen is examined, from which more detailed information of the reactions taking place inside the cell can also be derived. In the second part, the effect of the high activation potentials needed to activate lithium sulfide, the fully lithiated cathode material, is studied, with particular focus in the changes of its electrochemistry due to electrolyte reactions. In order to do so, a novel lithium sulfide-based material was synthesized, composed of ethylenediamine embedded into the crystal structure of lithium sulfide. Being amorphous instead of crystalline, this material demonstrates an extremely low activation potential, which also helps understanding the factors governing the reactivity of lithium sulfide

Zusammenfassung

Schwefel-basierte Elektroden haben wegen ihrer möglichen Anwendung in der nächsten Generation Akkumulatoren große Aufmerksamkeit auf sich gezogen; insbesondere da Schwefel ein umweltfreundliches und reichlich vorhandenes Element ist, das für die reversible elektrochemische Reaktion mit Lithium eine theoretische Kapazität von ungefähr 1675 mAh g^{-1} hat. Die Elektrochemie des Schwefels ist aber deutlich komplizierter als die der häufig angewandten Insertionsmaterialien in Lithium-Ionen-Akkumulatoren. Die elektrochemische Reduktion des in Lithium-Schwefel-Zellen enthaltenden Schwefels geschieht durch einen stufenweisen Mechanismus, bei dem lösliche Polysulfide gebildet werden. Das Auflösen von aktivem Material ist für die Zelle allerdings sehr schädlich, da dies mit einem Kapazitätsverlust der Elektrode einhergeht. Das bedeutet, dass dem Elektrolyten in diesem Akkumulator-Typ eine besonders wichtige Rolle zukommt – wichtiger noch als in anderen Systemen, in denen er nur ein Ionenleiter ist. In der nachfolgenden Arbeit werden die Zersetzungsreaktionen des am häufigsten verwendeten Elektrolyten für Lithium-Schwefel-Akkumulatoren studiert. Es ist bekannt, dass diese Reaktionen eine große Auswirkung auf die Elektrochemie des Schwefels haben. Der erste Teil dieser Arbeit besteht aus der Untersuchung von Zersetzungsreaktionen des Elektrolyten aufgrund gelösten Sauerstoffes. Dadurch wird ein tieferes Verständnis der Schwefel-Elektrochemie erhalten. In dem zweiten Teil dieser Arbeit wird der Effekt der höhen Spannung während der Lithiumsulfid-Aktvierung studiert, mit Fokus auf deren Auswirkung auf die Elektrolytzersetzung. Lithiumsulfid ist die vollständig lithiierte Form des Schwefels und entspricht somit dem entladenen Kathodenmaterial. Um diese Auswirkung zu analysieren, wurde ein neuartiges Lithiumsulfid-basiertes Material entwickelt, nämlich Lithiumsulfid mit eingebetteten Ethylendiamin-Molekülen. Dieses Material zeigt eine sehr niedrige Aktivierungsspannung, was dabei helfen kann, den Zersetzungsmechanismus des Elektrolytes wegen hoher Spannungen zu erklären.

Contents

Abstract I
Zusammenfassung III
Contents V
Acronyms VII
1 Introduction 1
1.1 Lithium-ion batteries electrochemistry 1
1.2 Alternative cathode materials 7
1.3 Sulfur-based cathodes 11
1.3.1 The sulfur electrochemistry 11
1.3.2 Challenges of lithium-sulfur batteries 14
1.3.3 Role of the electrolyte in LSBs 17
1.3.4 Lithium sulfide-based cathodes 20
2 Motivation and objectives 23
3 Theoretical background 25
3.1 Constant current methods 25
3.2 Constant voltage methods 28
3.3 Scanning voltage methods 29
3.4 Electrochemical impedance spectroscopy 34
3.5 Vibrational spectroscopic methods – Infrared and Raman 50
3.6 X-ray photoelectron spectroscopy 56
3.7 Scanning electron microscopy 59
3.8 Powder x-ray diffraction 61
3.9 Elemental determination – combustion analysis and atomic emission. 63
4 Results and discussion 65
4.1 Effect of dissolved air in the electrolyte 65
4.1.1 Experimental procedures 66
4.1.2 Electrochemistry of sulfur in different electrolytes 71
4.1.3 Reactions of the electrolyte – EIS studies 78
4.1.4 *Post mortem* analysis of the cathode 89
4.2 Ethylenediamine-embedded lithium sulfide – characterization and carbonization 96
4.2.1 Experimental procedures 96
4.2.2 Infrared characterization of Li2S-En 99
4.2.3 Carbon coating of lithium sulfide 101
4.3 Effect of aged electrolyte in lithium sulfide-based cells 111
4.3.1 Experimental procedures 111
4.3.2 Ageing of the electrolyte – impact on lithium sulfide electrochemistry 115
4.3.3 Impact of activation potential on the electrochemistry of lithium sulfide 122
4.3.4 Passivation layer formation on the different electrolytes 127

5 Conclusions 130
6 Bibliographical references 133
Acknowledgements 145

Acronyms

AC/S	Activated carbon/sulfur composite
ATR-FTIR	Attenuated total reflectance FTIR
CE	Counter electrode (auxiliary electrode)
CPE	Constant phase element
CV	Cyclic voltammetry
DMA	Dimethylacetamide
DMC	Dimethyl carbonate
DME	Dimethoxyethane
DME air	DME-based electrolyte stored under dry air
DME Ar	DME-based electrolyte stored under dry argon
DME:DOL air	DME:DOL-based electrolyte stored under dry air
DME:DOL Ar	DME:DOL-based electrolyte stored under dry argon
DOL	1,3-Dioxolane
EC	Ethylene carbonate
EIS	Electrochemical impedance spectroscopy
EMImTCM	1-butyl-3-methylimidazolium tricyanomethanide
En	Ethylenediamine
ESW	Electrochemical stability window
FTIR	Fourier-transform infrared spectroscopy
HF	High frequency
ICP-AES	Inductively couple plasma atomic emission spectroscopy
IL	Ionic liquid
IR	Infrared
LF	Low frequency
LFP	$LiFePO_4$
Li_2S-CC	Carbon-coated lithium sulfide

Li_2S-En	Ethylenediamine-embedded lithium sulfide
LIB	Lithium-ion battery
LiTFSI	Lithium bis(trifluoromethane)sulfonimide
LSB	Lithium-sulfur battery
MF	Middle frequency
NMP	N-methyl-2-pyrrolidone
OCP	Open circuit potential
PIB	Polyisobutylene
PVdF	Polyvinylidene fluoride
$Pyr_{1,4}TCM$	1-butyl-1-methylpyrrolidinium tricyanomethanide
Ref	Reference electrode
SEI	Solid electrolyte interphase
SEM	Scanning electron microscopy
TEGDME	Tetraethylene glycol dimethyl ether
THF	Tetrahydrofuran
WE	Working electrode
XPS	X-Ray photoelectron spectroscopy
XRD	Powder X-ray diffraction

1 Introduction

1.1 Lithium-ion batteries electrochemistry

Energy storage has always played a pivotal role in human life, from the development of food storage techniques, through the damming of rivers, to extraction of petroleum and coal. This is because energy demand in our civilization does not always match where and when that energy is produced. However, over the centuries our civilization overcome this hurdle by developed the ability to keep energy stocked for use at a different time and/or place. Lately, electrochemical energy storage has sparked a lot of interest[1–3], since they offer practical means to reliably supply electric energy, which can be easily converted into mechanical energy, thermal energy, and, most importantly, it can be used to power electronics.

One of the most notorious electrochemical energy storage devices is the battery, an electrochemical (galvanic) cell for which spontaneous chemical reactions occurring at the two electrodes produces a flow of electrons in an outside circuit.

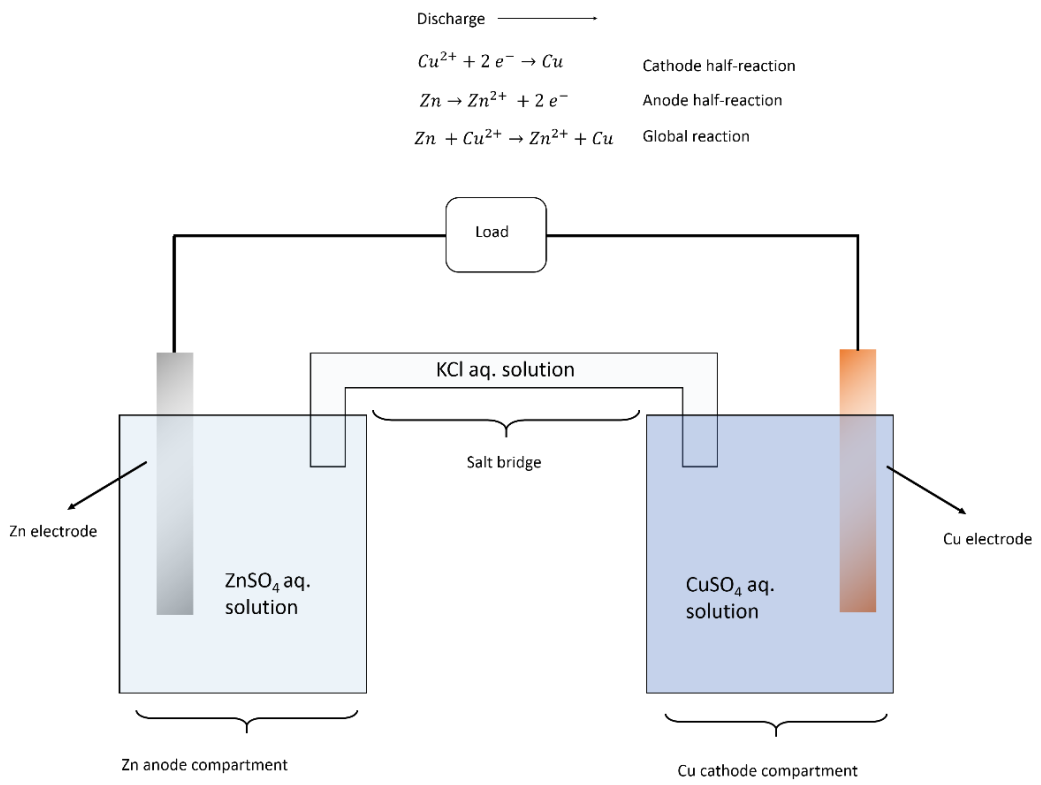

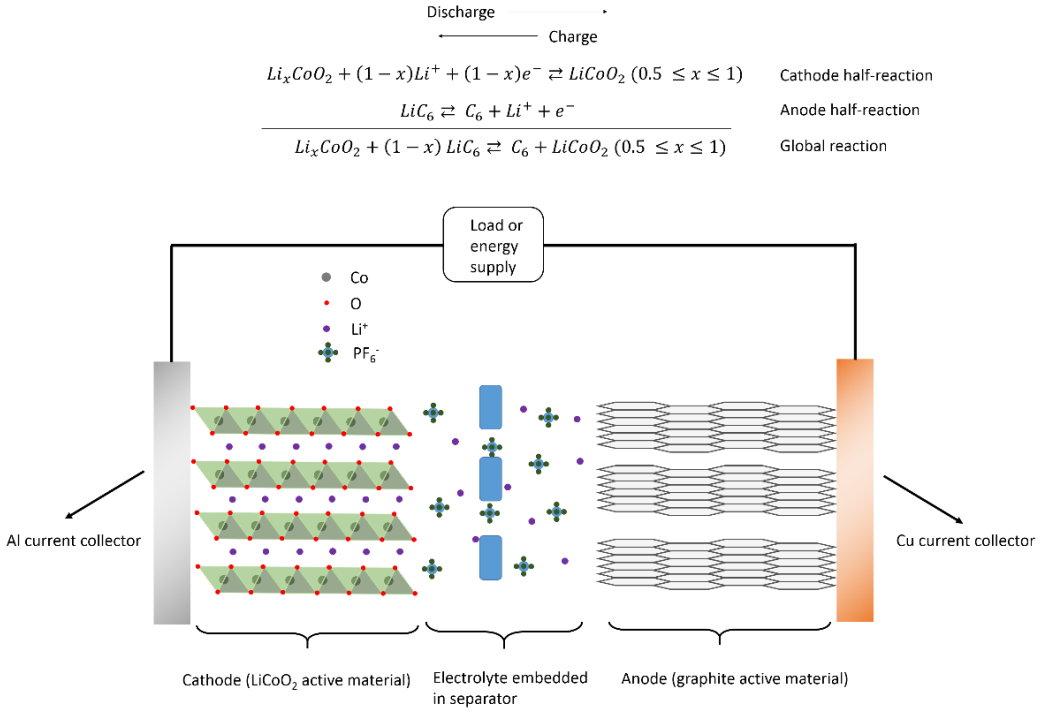

Figure 1.1.1. Simple schematics of a Daniell cell (above) and a modern lithium-ion battery (below), with the corresponding reactions shown above them.

The very first galvanic cells were relatively simple, consisting of a Cu and a Zn metal electrodes separated by a piece of paper embedded in a sodium chloride solution acting as electrolyte. The first efficient galvanic cell was, however, the so-called "Daniel cell" (Figure 1.1.1 above), featuring two distinct electrolyte compartments, one containing $CuSO_4$ in contact with the Cu electrode, and another one containing $ZnSO_4$ in contact with the Zn electrode. To ensure electrical neutrality, the two compartments are brought in contact through an ionic conductor, such as tube filled with a potassium chloride solution or an ionic conducting membrane. In the case of a Daniel cell, the spontaneous reaction is that between Zn metal and Cu^{2+} ions in solution, since Cu^{2+} is more electronegative than the Zn atoms. In one of the compartment, the Cu^{2+} ions accept electrons. This side of the cell where the reduction occur is called the cathode. The opposite happens on the Zn side, where the metal loses its electrons (gets oxidized). This compartment is called the anode. The key aspect of this cell is that both these reactants are not in direct contact. This means that the reaction only happens once the electrons leave the zinc electrode, with release of Zn^{2+} ions in solution. On the other side, the Cu^{2+} ions in solution accept those electrons, being reduced to metallic Cu, which is deposited on the Cu electrode. These two reactions are individually called half-reactions, and the two species that undergo a change in their oxidation state (depending on the direction of reaction) form the redox couple. As the reaction proceeds, the Zn electrode is consumed, and the Cu^{2+} ions in cathode compartment reduced to metallic Cu, such that the amount of one or both reactants drops to zero.

State-of-the-art lithium-ion batteries (LIBs) work following the same principles, but the electrode materials have been changed to improve the overall battery's performance (Figure 1.1.1, below). The cathode is usually composed of a lithium-containing layered oxide (such as, e.g., $LiCoO_2$), with a carbon additive to render the electrode more conductive. A polymeric binder is used to hold all of the components

together, and to keep them adhered to a current collector, usually an Al foil. The anode is made mainly of graphite, but also contains a conductivity enhancer and a binder. The current collector in this case is a Cu foil instead of aluminum, to avoid any undesirable alloying reaction between Al and lithium. Since both the reactants in this case are solids, it is easier to keep them physically separated. This is accomplished by using a polymeric separator between the electrodes avoiding a short circuit. The separator is soaked in a liquid electrolyte, usually a mixture of organic carbonates (e.g., ethylene carbonate and propylene carbonate) with a lithium salt (e.g., $LiPF_6$ or $LiClO_4$) dissolved in it.

The components of the cell as assembled ($LiCoO_2$ and graphite) are in their respective discharged state, which are less reactive and easier to handle then their charged, energetic counterparts. During charge, the Co^{3+} ions in the $LiCoO_2$ crystals get oxidized to Co^{4+}. Simultaneously, lithium is deintercalated to balance the charge. As in the case of the Daniel cell, the electrolyte promotes ionic contact between cathode and anode, and ensures that neutrality is kept. On the other side, graphite is reduced, accepting one electron for every six membered carbon ring (C_6). As graphite is reduced, lithium ions are inserted between the graphene layers to balance the electrical charge. This process represents two great advantages of LIBs compared to the Daniell cell. First, the same ion that is removed from one electrode is inserted into the other ("rocking chair" battery), such that only one type electrolyte is necessary. Second, charging of the cell can be accomplished by applying an appropriate voltage between the two electrodes and reversing the electron flow in the cell (compared to the spontaneous discharge), a process which is not possible in the case of the Daniell cell.

During discharge the two half-reactions are reversed, with Co^{4+} accepting one electron to be reduced to Co^{3+}, with simultaneous insertion of lithium in between the CoO_2 slabs, and the C_6 rings of graphite lose an electron, followed by removal of the intercalated lithium ions. Just like in the previous case, the spontaneous reaction here

happens between the Co^{4+} ions and the LiC_6 moieties in the lithiated graphite, with the former being more electronegative than the latter.

Though very well developed, this technology is not without its shortcomings. The $LiCoO_2$ cathode material can be thought of as a layered compound, with layers comprised of CoO_2 groups alternating with intercalated lithium ion layers[1]. Removal of the lithium cations bring the oxygens from the CoO_2 closer together, which start repelling each other and destabilizes the structure[4]. This destabilization can lead to the evolution of O_2 [1] which, in turn, can react with the organic electrolyte leading to fire and, potentially, explosion. For this reason, $LiCoO_2$ materials are never fully de-lithiated, with the charge stopped at 4.2 V vs. Li/Li^+, at which point the material contains approximately half of the original amount of lithium ($Li_{0.5}CoO_2$)[5]. This leads to an effective loss of capacity, since only around 140 mAh g^{-1} of the 280 mAh g^{-1} total theoretical capacity of $LiCoO_2$ can be reversibly accessed. Besides this problem, Co is a costly and environmentally unfriendly metal, which not only raises the cost of LIBs, but also poses concerns about its availability in the future[6].

Besides the problems cited with the cathode, there are other issues involving the other cells components too For example, the electrolyte are composed of a lithium salt dissolved in alkyl-carbonates. The most common formulation consists of a 1:1 mixture of ethylene carbonate (EC) and dimethyl carbonate (DMC), with lithium hexafluorophosphate ($LiPF_6$) dissolved in it[7,8]. This electrolyte is very stable towards oxidation by high electrochemical potentials, usually up to 5 V vs. Li/Li^+, mainly due to the highly oxidized carbonate moiety[3]. This property makes them specifically suitable to the $LiCoO_2$ cathode, which operates at a much lower voltage than the anodic stability of the electrolyte. On the other hand, this highly oxidized state of the electrolyte decreases its cathodic stability, shifting it to higher potentials, and making it more prone to be reduced. However, the reduced species are insoluble in the electrolyte, and form what is

known as the solid electrolyte interphase (SEI)[9]. The SEI is shown to be composed mostly of inorganic and organic lithium salts, such as lithium carbonates, lithium fluoride, lithium organic carbonates, polyesters and polycarbonates[9–12]. A good SEI is both an electronic insulator and an ionic conductor, allowing lithium ions diffusion while preventing further decomposition of the electrolyte by the low potential of the electrode. It also forces the lithium ions to lose their solvating shell before reaching the graphite particles, preventing the intercalation of solvated lithium into the graphite, which can lead to exfoliation of the negative electrode. Despite these positive attributes, the SEI formation is not without negative impacts to LIBs. Since the cells are assembled in the discharged state, no reaction happens between the graphite and the electrolyte until the first charge, when the potential of the graphite anode is lowered[13]. This effectively consumes part of the lithium from the cathode, leading to an inactive mass that lowers the gravimetric capacity of the cell. Also, if the SEI is not stabilized through the use of appropriate additives[14,15], it can lose its electronically insulating properties by detachment from the electrode and/or appearance of cracks, leading to continuous electrolyte degradation.

Despite the abovementioned drawbacks, LIBs have been optimized to such a level that the practical capacity is rapidly approaching the theoretical one[2], mostly pushed by better manufacturing processes and cell designs. In order to improve even further the energy density LIBs, new electrode and electrolyte materials are therefore required.

1.2 Alternative cathode materials

In order to improve the energy density of LIBs, a lot of effort has been put on developing cathode active material with larger specific capacity, higher operating potential, increased safety and reduced costs. One straightforward approach is using alternative layered compounds with the general formula $LiMO_2$, similar to $LiCoO_2$, but partially or totally replacing Co with other transition metal(s) M.

$$LiMO_2 \rightleftarrows Li_{1-x}MO_2 + x\,Li^+ + x\,e^- \quad \textbf{[1.2.1]}$$

A lithium metal oxide with the formula $Li[Ni_{0.5}Mn_{0.5}]O_2$, where the Co ions are substituted by Mn and Ni, was reported to perform very well[16], with up to 200 mAh g^{-1} practical reversible capacity[17]. This improvement was shown to be mainly due to defects where Ni ions are present in the lithium layer, which keeps the MO_2 layers stable[18,19]. Ni also serves as the redox pair in $Li[Ni_{0.5}Mn_{0.5}]O_2$ [20], being converted between Ni^{2+} and Ni^{4+} in the region between 3.6 and 4.3 V vs. Li/Li^+. While beneficial for the structural integrity of the cathode material, the presence of Ni ions in the lithium containing layer has a negative effect on the lithium mobility[21], considerably decreasing rate capability of the electrode, leading to trade-off between rate capability and specific capacity for different materials. This is more evident when some of the transition metals are substitute again with Co. One of the first examples was the $Li[Ni_{0.33}Mn_{0.33}Co_{0.33}]O_2$, also known as NMC-111[22], using a 1:1:1 ratio of Ni:Mn:Co, but other ratios have also shown improved rate capability[23]. The redox couple were shown to be Ni^{2+}/Ni^{4+} and Co^{3+}/Co^{4+}. Co^{3+} oxidation to Co^{4+} is allowed to happen only partially due to Co^{3+}/Co^{4+} electronic bands partially overlapping with the O^{2-} bands[24–26], which can lead to oxygen evolution, similar to pure $LiCoO_2$. The next advance in layered oxides involved the substitution of some of the transition metals in the transition metal layer for lithium ions[1,27]. This happens, for example, by incrementally substituting Ni^{2+} in $Li[Ni_{0.5}Mn_{0.5}]O_2$ for the appropriate amount of Li^+ and Mn^{4+} cations, until all Ni is substituted, forming a compound with the

formula $Li[Li_{0.33}Mn_{0.66}]O_2$ (alternatively, Li_2MnO_3). This was initially thought to be inactive, but activation to 4.8V vs. Li/Li^+ was shown to render it electrochemically active[28]. The exact mechanism through which this occurs is still under investigation, but all evidence point towards the partial loss of Li_2O (from Li_2MnO_3) to form $LiMnO_2$ [1,27], which is electrochemically active, while the remainder of Li_2MnO_3 stabilizes the MnO_2 structure, thus grant improved capacity retention.

Another class of promising lithium metal oxides is that belonging to the spinel group, with general formula LiM_2O_4. Spinels have a similar structure to layered lithium metal oxides, but some of the MO_6 octahedra are shifted to the lithium layer plane. This rearrangement provides increased structural stability, as well as improved lithium diffusion, since the lithium ions can now diffuse in any of the three dimensions. The first such spinel to be used as an insertion cathode was $LiMn_2O_4$ [29,30]. This material was, however, found to show strong capacity fading due to Mn dissolution into the electrolyte[31]. Attempts to minimize this issue been made by partially substituting Mn for other transition metals, with the best results being achieved when using Ni, to form $Li[Ni_{0.5}Mn_{1.5}]O_4$ [32–35]. This material still suffers from high surface reactivity, which leads to capacity fading[36]. To counter that, several coating materials have been used to separate the spinel and the electrolyte, and thus avoid decomposition reactions, but they suffer from the disadvantage of increasing the deadweight of the electrode[37].

The final class of insertion materials to draw interest as cathodes are the phospho-olivines with general formula $LiMPO_4$. The first such materials to be successfully employed in LIBs was $LiFePO_4$ (LFP)[38,39].

$$LiFePO_4 \rightleftarrows FePO_4 + Li^+ + e^- \qquad \textbf{[1.2.2]}$$

LFP also contains transition metal layer, in the form of FeO_6 octahedra. However, such layers are separated by another one containing both lithium and phosphate ions[40], with lithium diffusion being mostly one dimensional[40,41]. Discharge is

also peculiar in that it occurs through the formation of two phases, one composed of $LiFePO_4$, and one of only $FePO_4$ [39,42,43], yielding a very stable discharge plateau. Despite good theoretical capacity of 170 mAh g^{-1}, LFP shows intrinsically poor electronic conductivity, requiring the use of conductive additives, like carbon coatings, to fully access the expected capacity[44]. Besides, the relatively low working discharge potential of 3.3 V vs. Li/Li^+ penalizes the energy density of the LIB, compared to $LiCoO_2$. Still, the environmental friendliness and availability of the raw materials make this an attractive cathode material.

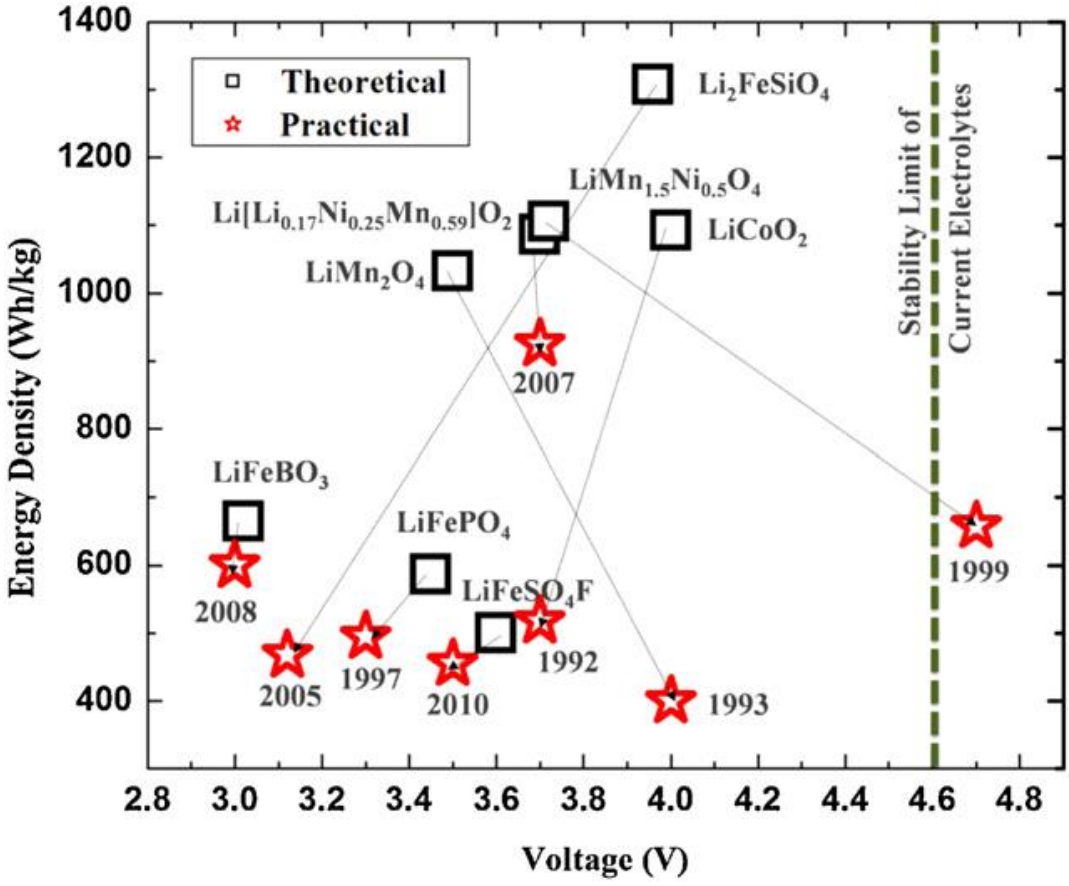

Figure 1.2.1. Theoretical and practical energy densities and operating voltages of different insertion cathodes. Picture reproduced with permission from reference 1.

In general, insertion type cathode materials are the most researched ones in the last couple of years, and, as a result, one of the most mature technologies. A direct result of this is that, in various cases, their practical capacity is approaching the theoretical one, leaving limited room for improvement (Figure 1.2.1). Increasing the theoretical

capacity is not a trivial task though, as these materials present a series of similarities that hinder further development. In most cases, their electrochemistry is restricted to a one-electron process per unit formula, limiting the amount of charge they can hold. Besides, transition metals themselves tend to have a high atomic weight, and must be coupled with an anion, further increasing the inactive mass, and decreasing specific capacity. For this reason, it is expected that future batteries will steer away from insertion materials, and focus on conversion-type electrode materials[2]. These include systems such as an oxygen cathode, in which oxygen from the air is reduced to form lithium peroxide, Li_2O_2. The advantages of this over insertion materials are immediately clear. The reduction process involves two electrons, and both oxygen atoms are reduced, i.e., there are no atomic species that do not participate in the reaction. In particular to oxygen, it can be extracted directly from the air, decreasing even further the amount of material that must be packed in the battery. Oxygen-based cathodes, however, are still in their infancy, with the greatest challenge being the three phases involved in the reduction, where gaseous oxygen must react in contact with the liquid electrolyte to form a solid discharge product, as well as the high reactivity of the intermediary radicals formed[45]. Another candidate for conversion cathodes is elemental sulfur, which will be discussed in detail in the next section

1.3 Sulfur-based cathodes

Sulfur has long been recognized as a possible cathode material for lithium batteries[46]. The following section explores a little more in depth some of the available literature regarding this material

1.3.1 The sulfur electrochemistry

The global reaction occurring in lithium-sulfur batteries can be summarized as:

$$S_8 + 16\,Li \rightleftarrows 8\,Li_2S \qquad [1.3.1]$$

This reaction gives it its high theoretical capacity of around 1672 mAh g^{-1}, making sulfur a very attractive material. Indeed, despite the low average discharge voltage of only ~2 V vs. Li/Li^+, the specific energy of a Li-S battery is still substantially higher than LIBs, i.e., about 2600 Wh kg^{-1}.

Despite the simplicity of the overall cell reaction, sulfur presents a complex, multi-phase reduction mechanism[47–50].

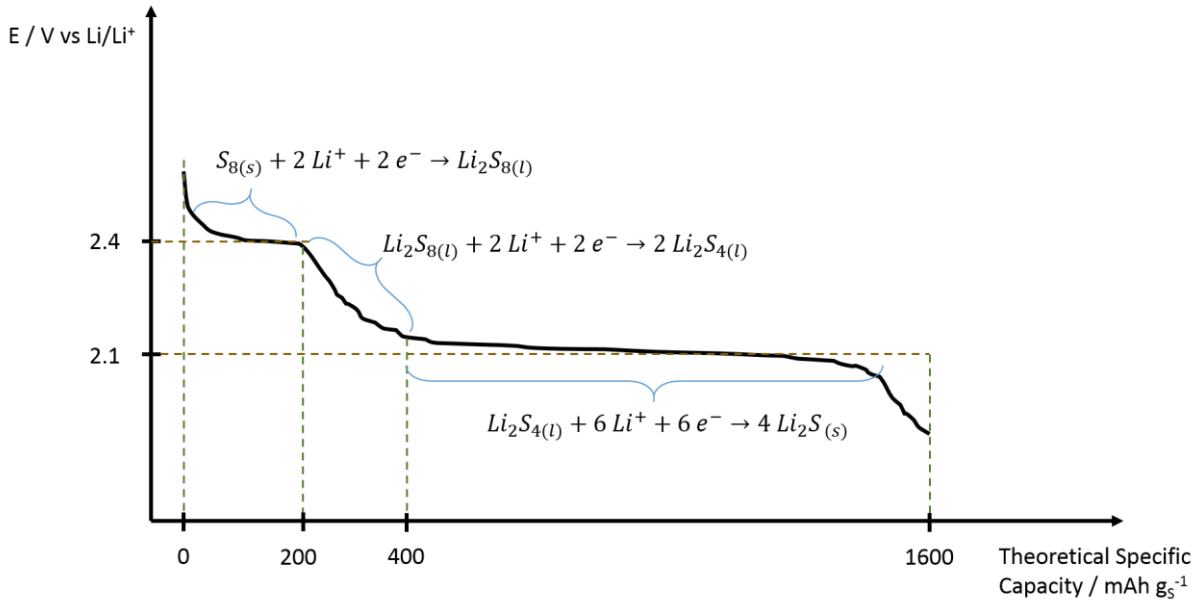

Figure 1.3.1. Scheme of a theoretical discharge curve of a sulfur-based cathode.

Figure 1.3.1 schematically shows the theoretical voltage profile of a typical sulfur electrode during discharge. The discharge curve is characterized by two discharge

plateaus, a short, high voltage one at around 2.4 V vs. Li/Li^+, and a long, low voltage plateau at around 2.1 V vs. Li/Li^+. Between these two plateaus, another short, sloping region is present. The exact nature of the reactions is not completely understood yet, and a matter of intense debate in literature. Still, some agreement has been reached regarding the main steps of the mechanism. The first plateau corresponds to the transformation of solid S_8 into dissolved polysulfide according to the following equation:

$$S_{8(s)} + 2\,Li^+ + 2\,e^- \rightarrow Li_2S_{8(l)} \qquad \textbf{[1.3.2]}$$

Commonly this plateau has an equivalent charge of around 200 mAh g_S^{-1}, which corresponds to the transfer of two electrons per mole of S_8 molecules, which is in line with the proposed formation of a long-chain polysulfide. A second important point relates to the shape of the plateau in this reaction. Just like temperature or pressure, electrochemical potential is an intensive property. The number of such properties that can be independently varied without affecting the others is described by the Gibbs' phase rule:

$$F = C - P + 2 \qquad \textbf{[1.3.3]}$$

Where F is the number of degrees of freedom (i.e., the maximum number of independently variable intensive properties), C is the number of components (chemical species), and P is the number of phases in the system, which are assumed to be in thermodynamic equilibrium. In the abovementioned case, there are two chemical components, S_8 and Li_2S_8, such that C = 2, as well as two phases, solid and liquid (solution), such that P = 2. This means that F = 2, i.e., the system has only two degrees of freedom. There are, however, three intensive properties relevant to an electrochemical cell, temperature, pressure, and electrochemical potential, such that only two of those properties can be arbitrarily changed, and the third is a function of the other two. Experiments are often done at constant pressure and temperature, such that two-phase two-components electrochemical cells present a constant voltage as their composition

change[51] (i.e., during either discharge or charge of the material). This explains the constant voltage often observed during the first discharge of sulfur electrodes.

The second, sloping region, corresponds to the shortening of the polysulfide chains according to:

$$Li_2S_{8(l)} + 2\,Li^+ + 2\,e^- \rightarrow 2\,Li_2S_{4(l)} \quad \textbf{[1.3.4]}$$

The precise composition of the products generated in this potential region are still a matter of debate, with many different lengths of polysulfides having been observed experimentally[47,49,52]. The sloping nature indicates that it is no longer a two-phase two-component process. Instead, it is in line with a single-phase, two-component system, the components being the oxidized and reduced species, and the phase being the solution. Through analysis of Gibbs' phase rule, this would give three degrees of freedom, such that, even if the temperature and pressure are kept constant, the voltage can still freely vary.

The third and final step is then the formation of the solid discharge products as it follows:

$$Li_2S_{4(l)} + 2\,Li^+ + 2\,e^- \rightarrow 2\,Li_2S_{2(s)} \quad \textbf{[1.3.5]}$$

$$Li_2S_{4(l)} + 6\,Li^+ + 6\,e^- \rightarrow 4\,Li_2S_{(s)} \quad \textbf{[1.3.6]}$$

As is the case of the sloping region, the exact composition of the final discharge products is not precisely controlled, with a mixture of Li_2S and Li_2S_2 formed[53], which can decrease the total capacity of this region. Just like in the high voltage plateau, this region is characterized by a two-component two-phase process, resulting once again in a constant voltage during reduction.

1.3.2 Challenges of lithium-sulfur batteries

Lithium-sulfur batteries (LSBs) are plagued by a variety of problems intrinsic to the material's electrochemical behavior, which will have to be solved before the system can be commercialized. The main ones are the low electronic conductivity of both sulfur and lithium sulfide, which makes it harder to fully access the theoretical capacity[54], and the dissolution of the polysulfides, which drains active material from the electrode into electrolyte. One widely used strategy to minimize these is to intimately mix sulfur with different kinds of host materials[55–64]. Activated carbon is an ideal material for this type of application due to its usually high specific area, high electronic conductivity, as well as morphological and chemical tunability. For example, activated carbons can comprise macropores (pore diameter > 50 nm), mesopores (50 to 2 nm) and/or micropores (< 2 nm). Changing the pore size can have a huge impact on the behavior of the sulfur cathode. For example, large macropores show a very poor capacity compared to mesopores[61], a problem that can be mainly ascribed to the relatively lower specific area of the former, which decreases the amount of solid products that can be deposited before all the surface is blocked by the insulating products. For the same reason, mesoporous carbon has been intensively investigated as carbon host for sulfur[55,57,58,60,65], as mesopores offer enough volume and surface area to adequately host sulfur. Finally, microporous carbon has also shown some interesting results when used as host for sulfur[59,66,67]. Micropores in the activated carbon can be made smaller than the average size of the S_8 molecule, the so-called ultra-micropores. The average size of the S_8 molecule is around 0.7 nm[68]. Using pores of with an average size of 0.55 nm, for example, means the S_8 molecules do not fit inside the pores[69]. Instead, the molecules must break down into smaller ones with less sulfur atoms, such as $S_{2\text{-}4}$, in order to be able to access the pores[69]. This completely changes the electrochemistry of sulfur, avoiding its dissolution in the electrolyte. The

price to pay is a decreased electrode potential, as well as limited sulfur loading achievable due to the smaller pore volume.

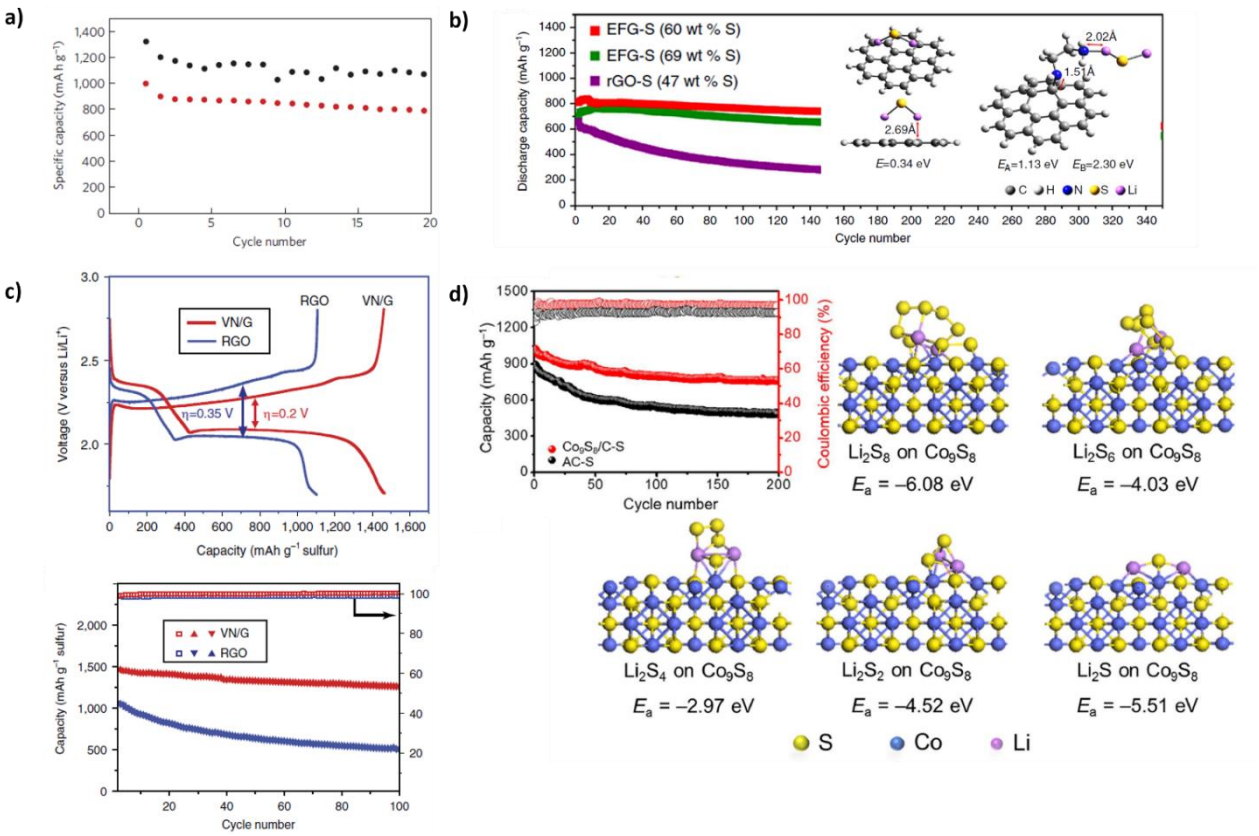

Figure 1.3.2. a) Cycling stability comparison of CMK-3/S-polyethyleneglycol (upper points, in black) versus CMK-3/S (lower points, in red) at 168mA g-1 at room temperature. Adapted from reference 60. *b) Cyclability of EFG–S nanocomposite (60 and 69 wt.% S) and rGO–S composite (47 wt.% S). Inset: DFT calculation showing the interaction between Li2S cluster and single-layer graphene or amino-functionalized graphene. Adapted from reference* 70. *c) Galvanostatic charge–discharge profiles of the vanadium nitride-reduced graphene oxide (VN/G) and reduced graphene oxide (RGO) cathodes at 0.2 C (upper pane) and Cycling performance and coulombic efficiency of the VN/G and RGO cathodes at 0.2 C for 100 cycles (lower pane). Adapted from reference* 71. *d) Cycling performances and corresponding Coulombic efficiencies of Co_9S_8/C-S and AC-S cathodes at 0.5 C, and Calculated adsorption energies (E_a) of and Li_2S_x (x = 1, 2, 4, 6 or 8) species on the (202) planes of Co_9S_8 crystals. Adapted from reference* 72.

Another strategy to reduce polysulfides dissolution is to chemically modify the cathodes' surface in order to increase compatibility between polysulfides and the host material. This is often done by making the electrode more hydrophilic, either by changing the carbon host, the binder, using additional components as acting as polysulfide traps, or a mixture of these. For example, it has been shown that introducing polar chemical moieties to the carbon can help trapping long-chain polysulfides on the cathode[60,70] (Figure 1.3.2a and b), thus avoiding active material loss to the electrolyte. Positive results can also be observed by using more hydrophilic binders. The most commonly used binder in sulfur cathodes is polyvinylidene fluoride (PVdF), the same as used in LIB electrodes. Binders with more polar groups have been shown to improve both specific capacity and capacity retention[73–76], and molecular dynamic calculations point in the direction that this is a direct result of improved interactions between the binder and the (poly-)sulfides formed[73]. As an added benefit, such hydrophilic binders can be often processes in water, while PVdF requires N-methyl-2-pyrrolidone (NMP), a toxic and expensive solvent. Finally, adding inorganic compounds, such as transition metal oxides, sulfides, or nitrides[71,72,77–84], has also been shown to be an effective strategy (Figure 1.3.2c and d). They usually show highly polar bonds on the surface of the particles which interact well with polysulfides. Promoting these strong interactions works not only by trapping the soluble polysulfides in the cathode[71,72,77–81,83–85], but also seems to enhance the kinetics of the reduction reaction[71,72,82,86]. The mechanism of kinetic enhancement has not been fully explained yet, but analysis of the available literature indicates that they can favor lithium sulfide formation, which would shift the equilibrium towards the polysulfide reduction and sulfide formation.

1.3.3 Role of the electrolyte in LSBs

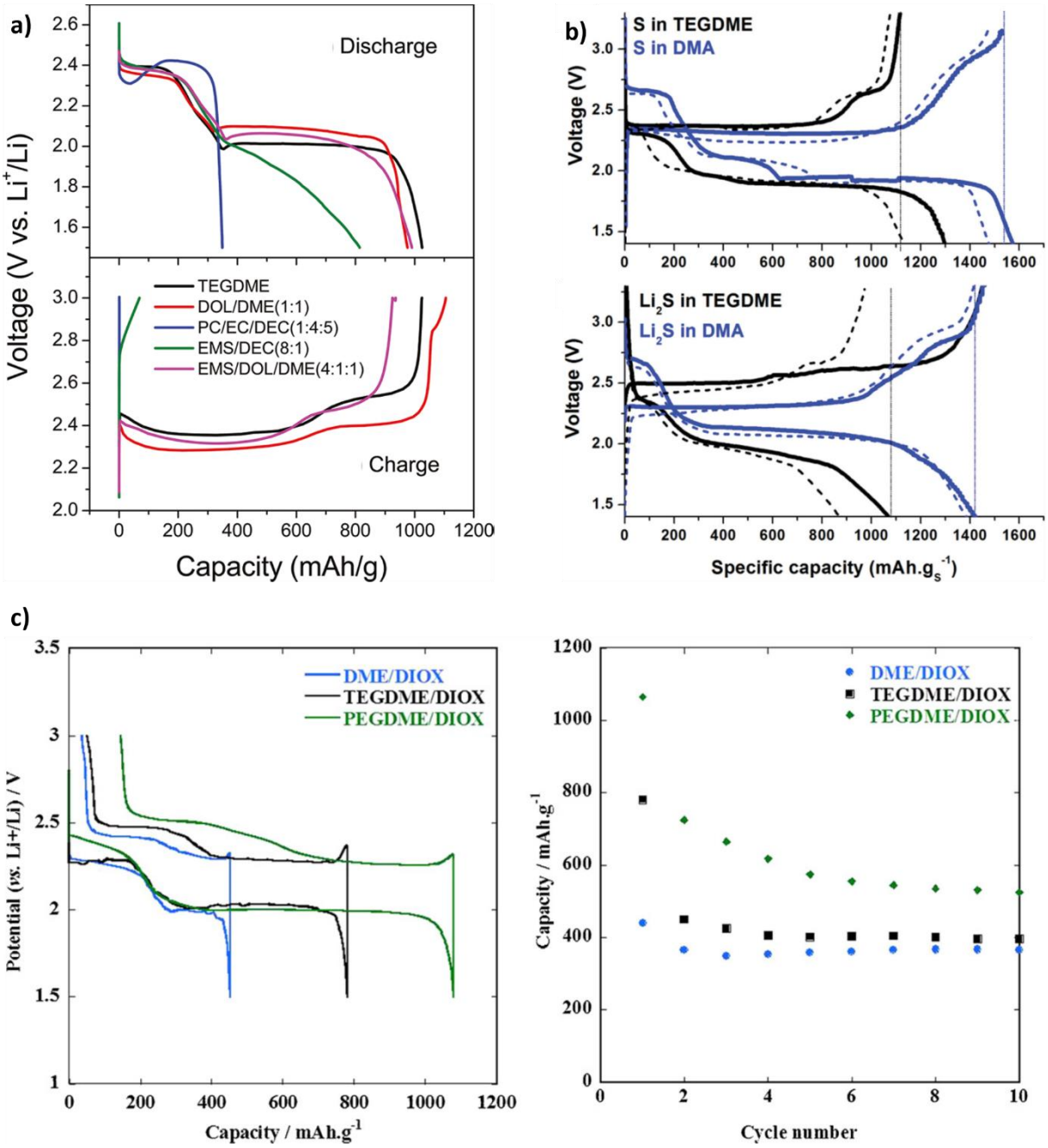

Figure 1.3.3. a) Discharge and charge voltage profiles of sulfur-based cathode using 1 mol L^{-1} $LiCF_3SO_3$ in different solvents as electrolytes. Adapted from reference 87. *b) First (solid lines) and second (dashed lines) discharge and charge voltage profiles of sulfur and Li_2S based cathodes using 1 mol L^{-1} $LiClO_4$ in different solvents as electrolyte. Adapted from reference* 48. *c) First discharge and charge profiles of sulfur-based cathode using 1 mol L^{-1} LiTFSI in different solvents as electrolyte. Adapted from reference* 88.

The electrolyte itself is also a key element that dictates the behavior of sulfur batteries[54,68,89,90]. This is expected, as sulfur reduction leads to the formation of soluble

polysulfides, an the their complexation and electrochemical activity is highly dependent on the electrolyte components[91]. For example, when cycling sulfur cathodes with carbonate-based electrolytes (Figure 1.3.3a) the cells present very poor electrochemical performance[87,92]. This is due to the high nucleophilicity of the polysulfides formed during discharge, which readily react with the carbonyl groups of the electrolyte solvents, forming electrochemically inactive thio-carbonates. Some improvements were observed, however, using dimethylacetamide (DMA) as solvent (Figure 1.3.3b)[48], possibly due to its much less electrophilic amide group. The change in solvent lead to an apparently different mechanism of sulfur reduction, with the slopping region being extended in comparison to the control ether-based electrolyte, as well as a more pronounced formation of $S_3^{\bullet-}$, likely due to the more extensive formation and disproportionation of polysulfides, as observed by X-ray absorption near edge structure (XANES). Overall, cyclability was poor due to exposure of the electrolyte to the lithium metal, requiring the introduction of a membrane to protect the anode from the liquid electrolyte. This problem is avoided altogether when using cathodes based on sulfur encapsulated in ultramicropores[66,67], since no polysulfides, allowing carbonate electrolytes to be used.

Ultimately, given their limited reactivity towards polysulfides, ether-based solutions demonstrated to be the most suitable class of electrolytes for sulfur batteries (Figure 1.3.3a and c). Early works mostly focused on single solvents, such as tetrahydrofuran (THF)[91], but eventually started branching into ethylene glycols of varying chain lengths[93–95]. Successively, great improvements were achieved by addition of 1,3-dioxolane (DOL) as co-solvent[96], This was found to help with the sulfur electrochemistry by decreasing viscosity and, in turn, increasing the ionic conductivity of the electrolyte. DOL was also found to polymerize on the lithium anode, forming a stable SEI[97,98]. Eventually, the use of dimethoxyethane (DME) and DOL in a 1:1 mixture (or

tetraethylene glycol dimethyl ether (TEGDME) and DOL in the same ratio) became the standard electrolyte formulation for lithium-sulfur cells[99,100].

As mentioned, DOL was found to be beneficial due to its ability to form a stable SEI on lithium. However, additives have also been proposed for further improving the formed passivation layer, such as $LiNO_3$[101], P_2S_5[102], or LiI[103]. Of those, $LiNO_3$ is definitely the most commonly used. Nitrate ions can be reduced below 1.7 V vs. Li/Li^+, which means that they spontaneously react when in contact with lithium metal[104]. The decomposition mechanism is still not entirely known. However, the composition of the SEI formed in presence of $LiNO_3$ has been studied in detail[105,106]. When nitrate is present in the electrolyte, there is the formation of reduced nitrogenated species (such as Li_3N and LiN_xO_y), which seem to form a good SEI. The nitrate ions seem to have another positive property in that they oxidize the other components formed by reductive decomposition over the lithium metal. This is seen as an increase in the amount of groups such as carbonyls, carboxylates, and carbonates in the SEI. There is also oxidation of sulfides eventually formed over the lithium surface, turning them into more oxidized LiS_xO_y species. The result is a more compact and impermeable SEI, which decreases the amount of polysulfides coming in direct with lithium metal. The improved SEI has a positive impact on the cathode cyclability, as it decreases the sulfur loss due to reactions with the anode. The reactivity of $LiNO_3$ towards sulfides can also be detrimental for the sulfur cathode, in particular if the cell is discharged below the reduction potential of nitrate[107]. Though the cause is not yet clear, it is reasonable to expect that the nitrate ions oxidize the lithium sulfide formed during discharge, leading to loss of active material.

1.3.4 Lithium sulfide-based cathodes

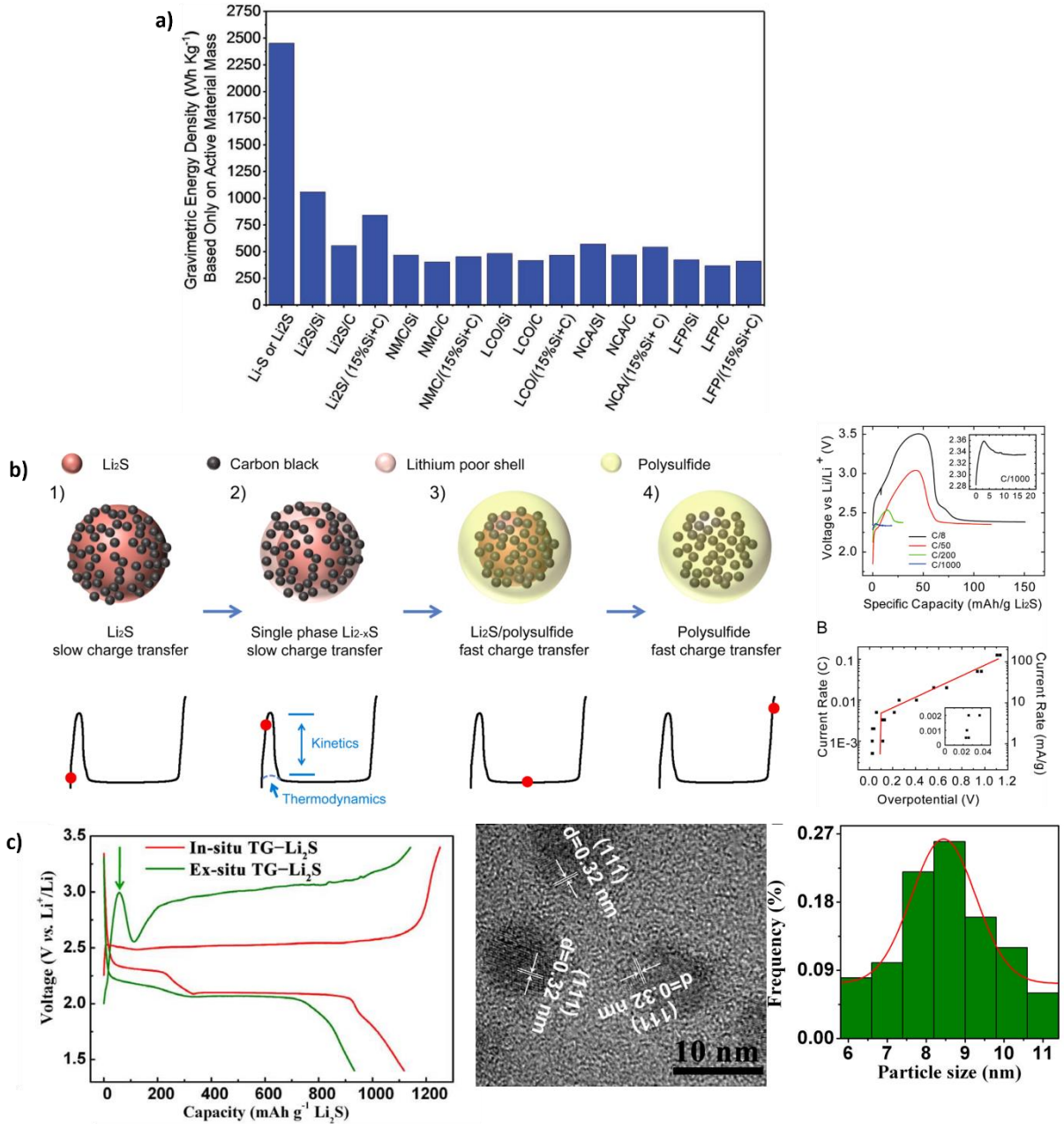

Figure 1.3.4. a) Theoretical energy densities of different battery configurations. Adapted from 108. *b) Activation mechanism and activation potential dependency on charging rate for lithium sulfide particles. Adapted from* 109. *c) Effect of nanosizing lithium sulfide particles on the activation potential. Red voltage profiles, TEM and particle size distribution correspond to nanosized lithium sulfide. Green voltage profile corresponds to commercial lithium sulfide. Adapted from reference* 110.

Despite all the improvements in the field, in regards of lithium protection, there is still a lot of apprehension regarding using metallic lithium in rechargeable batteries. This is because lithium has a strong tendency to unevenly deposit upon charge, resulting

on dendrites' growth[111–115] which can lead to short circuits with possibly catastrophic results. The consequence of this for sulfur batteries is that there has been a growing interest in using Li_2S, the final discharge product of sulfur cathodes, as active cathode material[116]. Lithium sulfide is already in the lithiated state, and can be used with lithium-free anodes, such as graphite or Si, without the need of expensive and complicated lithiation procedures, greatly improving the ease of assembly of S-based lithium-ion batteries[108]. Li_2S also possess some other advantages compared with sulfur. In fact, it can be processed at higher temperatures, while sulfur tends to sublimate if heated and/or exposed to vacuum. Also. It is already in the fully expanded state, such that no additional void space needs to be incorporated into the electrode to buffer the volumetric changes. Lithium sulfide has disadvantages in comparison to sulfur too, like being extremely sensitive to air and moisture, which requires the electrode processing to be carried out under inert atmosphere. The main disadvantage, however, is that lithium sulfide requires a first cycle activation [116,117], due to a kinetically slow first lithium extraction[109]. During the first charge, lithium ions have to be extracted from the highly crystalline lithium sulfide, which is a very slow process. The large overpotential requires to perform the first activation at very low current, and up to 4 V vs. Li/Li^+ to ensure the full charge (whereas normal cycling is conducted up to 3 V vs. Li/Li^+ or lower). However, charging up to 4 V may be very detrimental to the cell performance , since electrolytes containing DOL are only reasonably stable up to around 3.6 V vs. Li/Li^+ [118]. This triggers a series of problems in the cells, among which are a low coulombic and energy efficiency in the first charge, and decomposition of the electrolyte, which can have a negative impact on cell lifetime. Considerable efforts have been done to decrease the activation barrier of lithium sulfide. The most commonly used and successful approach is the concomitant reduction of the lithium sulfide particles' size, followed by intimately embedding them in a carbon matrix[110,119–122]. It owes its success to the increased specific

surface area of nanoparticles, which improves lithium extraction, as well as a fast electron transport due to the conductive matrix tightly surrounding the particles. Other attempts to solve this include annealing commercial lithium sulfide[116], which removes most of the electronically insulating native layer (such as LiOH, LiSH, Li_2CO_3) formed over the Li_2S particles when exposed to humid air, or the incorporation of redox mediators in the electrolyte[123], which increase the charge transfer rate between current collector and active particles.

2 Motivation and objectives

As discussed in the Introduction, the electrochemistry of LSBs is very different from that of LIBs, since the active material on the former unavoidably dissolves in the electrolyte during its normal operation. This means, among other consequences, that the electrolyte plays a much bigger role in LSBs than other, more common systems. This work aims to explore in detail the effect of decomposition of the state-of-the-art electrolyte on the performance of sulfur and lithium sulfide-based cathodes.

In the first part, the impact of dissolved oxygen in the electrolyte on the operation of LSBs will be evaluated. Specifically, the impact of oxygen coming from a dry air environment can be of great interest to both researchers and manufacturers. In fact, the cell assembly can be made easier, and cheaper, if the use of completely inert atmosphere (for example, dry argon atmosphere) is avoided. Moreover, oxygen from air is an easy to find contaminant, and knowing how to recognize its effect, if any, can be an important information. Finally, oxygen is known to form very reactive radicals, which can serve as a model to understand the repercussion of this class of chemicals on the electrolyte of LSBs.

On the second part, the impact of high activation potentials, which are often used on lithium sulfide-based cathodes, will be studied. To do so, firstly a novel kind of amorphous lithium sulfide possessing a reduced activation barrier, is synthesized and characterized. This material is used as a tool to asses the impact of varying the activation potential on the performance of Li_2S cathodes, but also might pave the way to a new class of active materials for LSBs.

Finally, the effect of ageing-induced electrolyte polymerization is evaluated, and correlated with the surface chemistry of different Li_2S-based cathodes with varying activation potentials. The results obtained can hopefully aid, not only to gain a deeper

fundamental understanding of this complicated electrochemistry, but also help for the practical development of commercial cells in the near future.

3 Theoretical background

In this section, the working principle of some of the main techniques used to realize this work are briefly explained.

3.1 Constant current methods

One of the simplest electrochemical experiments is to allow a constant current to flow though the cell, and measure the voltage change in the system as a function of time.

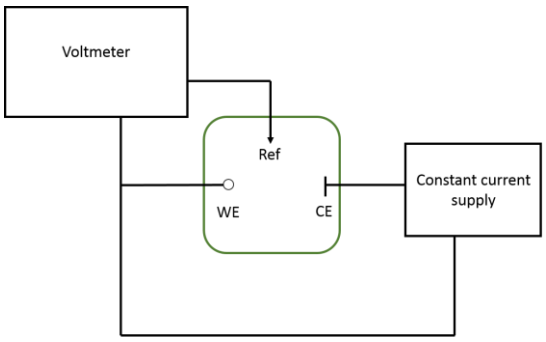

Figure 3.1.1. Scheme of a simple galvanostat.

Figure 3.1.1 shows an example of a simple galvanostat for conducting constant current experiments. In this simple setup, a current flows through the working and the counter electrodes. The flow of current though the system can have two effects on the measured potential. Firstly, the injected charge leads to a change in the state of the double-layer that is formed between the electrodes and the ions in solution, which happens throughout the length of the experiment. These changes in the double-layer, which can be understood as an effective charge of the capacitor that is formed on the electrode/electrolyte interface, have an effect on the potential of the electrode, which can be seen in the voltage over time curves. Secondly, the injected charges can lead to the oxidation/reduction of any electroactive species in contact with the electrodes. By changing the amount of these species, the potential of the electrode will change accordingly, with the potential shifting to lower values as more of the reduced species is

formed, and more positive as more of the oxidized species is formed. Besides these influences on the electrode potential, a flowing current in a cell can create an electric field between the working and reference electrode, since ions are moved from the bulk of the solution to the surface of the electrodes, and electrical neutrality is locally broken. This is often compared to an ohmic resistor (a resistor which obeys Ohm's law), and the change in potential caused by this phenomenon is called ohmic drop. All these changes are measured as the difference in voltage between the working electrode, which actually undergoes several reactions and changes potential during the experiment, and the reference electrode, which ideally is able to keep a fixed potential throughout the length of the experiment. Similar results can be obtained in a two-electrode setup, where the voltage is measured between the working electrode (WE) and the counter electrode (CE). Since current is flowing through the CE in this case, the electrode should be chosen carefully to guarantee negligible polarization. This setup is not preferred, since any change in the measured voltage can be caused by either changes in the potential of the WE, of the CE, or both at once, making the measured values less reliable.

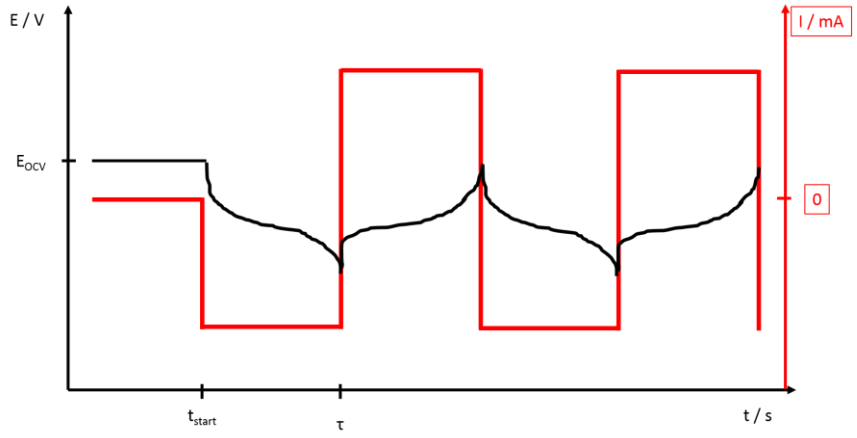

Figure 3.1.2. Sketch of a galvanostatic charge/discharge experiment. Red curve corresponds to the applied current, while black curve is measured voltage.

Figure 3.1.2 shows a sketch of a constant current experiment for an ordinary 1-electron reaction of electroactive species dissolved in the electrolyte. The actual voltage profile of the constant current experiment changes depending on the experimental conditions being used and the material being investigated. The voltage profiles also offer relevant information pertaining to the electrochemistry of the material under these conditions, and can be used to better understand the system. The voltage profile that is recorded is, in this case, a function of both the kinetics of the electrode reactions and current applied to the system. As pointed out above, the current in a diffusion-controlled system is correlated to the concentration gradient $^{\partial C_a}/_{\partial x}$ close to the surface of the electrode. For two systems containing different species with similar diffusion coefficients, if the same current is applied to them, the same concentration gradient should be formed on the surface of the electrode, i.e., they should have the same surface concentration at any given time. In case one of the species has a lower kinetic constant than the other, the former would require a more positive overpotential than the latter for a positive current, or a more negative overpotential in the case of a negative current, as per the Butler-Volmer equation. This difference in overpotential would be recorded in the potential profile, and can be used to estimate differences in electrochemical kinetics of the two species. Under these circumstances, the experiment would proceed until the surface concentration drops to zero, after which the concentration gradient cannot be affected by changing the applied potential. The potential would then sharply increase (for positive currents) or decrease (for negative currents) until a new reaction starts taking place, or a limit in the hardware is triggered. The time τ that it takes for the system to reach this state is independent of the kinetics of the electrode, and depends only on the flux of species from the bulk of the solution to the electrode. In the case of an electrochemically active species dissolved in solution, this time can be used to calculate the diffusion coefficient of the electroactive species by using the Sand equation:

$$\tau^{½} = \frac{n\,F\,A\,\pi^{½}}{2} * \frac{C_a D_a^{½}}{i} \qquad \textbf{[3.1.1]}$$

Where τ is the specific time, in s, n is the number of electrons involved in the reaction, F is Faraday constant, 96485 C mol^{-1}, A is the area of the electrode, in cm^2, C_a is the concentration of the species *a*, in mol cm^{-3}, D_a is the diffusion coefficient of the species *a*, in $cm^2\ s^{-1}$, and i is the absolute value of the current, in A.

Adapted from reference 124.

3.2 Constant voltage methods

Analogously to constant current experiments, electrochemical experiments can be performed where the voltage applied between the working and reference electrodes is kept constant, and the current flowing through the system is varied. This is done with a potentiostat, which is analogous to the galvanostat in Figure 3.1.1, except that now the voltage is being controlled, while the current is measured. When the experiment is started, the jump in potential has the effect of creating a momentary electric field in the solution, which in turn attracts or repels ions in solution, according to the values of the field and the charge of the ions. This is, once again, charging of the double-layer that is formed between the electrode and the electrolyte. Contrary to the case of constant current experiments though, the fixed potential means that the double-layer remains the same through out the experiment, and that there is no ohmic current in the electrolyte. It also means that the concentration of the active species on the surface of the electrode remains constant throughout it, usually being 0 if a high or low enough overpotential is applied. This is because the overpotential applied to the electrode is usually enough to oxidize/reduce all species that come in contact with the electrode. The current flowing through the electrode is then limited only by the supply of electroactive species, which in turn happens only by diffusion. The current over time curve in this case is described by the Cottrell equation:

$$i(t) = \frac{n\,F\,A\,C_a\,D_a^{½}}{\pi^{½}t^{½}} \qquad [3.2.1]$$

Where i is the current, in A, n is the number of electrons involved in the reaction, F is Faraday constant, 96485 C mol^{-1}, A is the area of the electrode, in cm^2, C_a is the concentration of the species *a*, in mol cm^{-3}, D_a is the diffusion coefficient of the species *a*, in $cm^2\ s^{-1}$, and t is the time, in s.

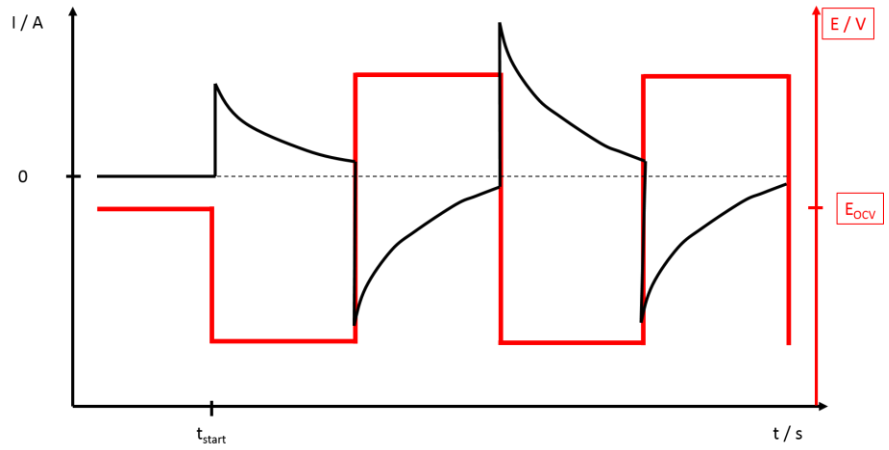

Figure 3.2.1. Sketch of a constant voltage experiment. Red curve corresponds to the applied voltage, while black curve is the measured current.

In the case of Figure 3.2.1, the current decays proportionally to $t^{-½}$, which is typical of diffusion-controlled processes. As the experiment goes on, the species must diffuse from farther and farther away from the surface of the electrode. This leads to a decrease in supply of the electroactive species, which in turn leads to a decrease in current. Unlike the case of controlled current method, kinetic effects are often not present in controlled voltage methods, only being observed as a decrease in the overall current if an insufficient overpotential is used.

Adapted from reference 124.

3.3 Scanning voltage methods

A third class of methods often employed in electrochemistry involve a varying potential over time applied on the working electrode, while recording the current flowing

through it. In this case, a potentiostat is also used to perform the experiment, with the difference that the applied voltage is not constant.

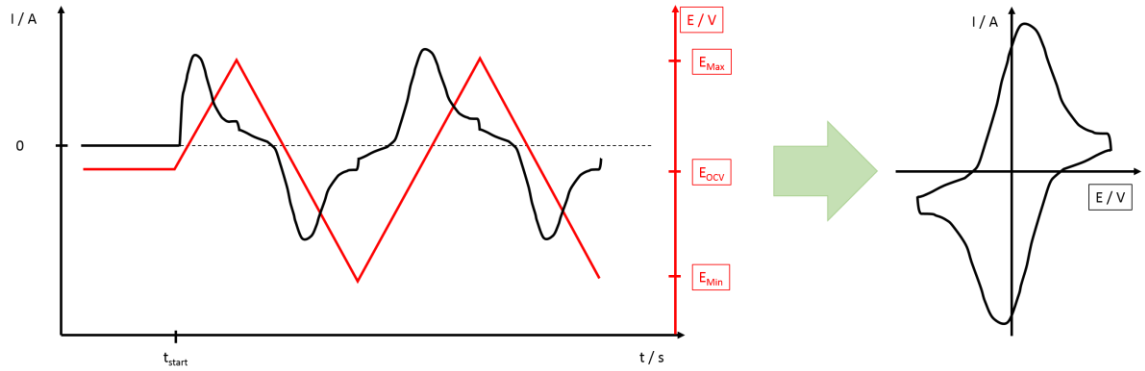

Figure 3.3.1. Sketch of a cyclic voltammetry experiment. Left: Experiment evolution over time. Red curve corresponds to the applied voltage, while black curve is the measured current. Right: I vs. E representation of the same experiment.

Figure 3.3.1 shows a schematized representation of one such experiments: a cyclic voltammetry (CV). In a CV, the potential applied to the working electrode is varied linearly between a minimum and a maximum predetermined value. This variation in potential leads to variations in current over time, both due to both Faradaic and capacitive processes. In the case of capacitive currents, the cause is similar to the one previously pointed out for constant current methods. Changing the potential of the electrode changes the double layer formed on its surface. This happens because of the electrical potential that is formed at the electrolyte when the electrode is (dis-)charged. This attracts ions of the opposite charge of the electrode in order to balance and neutralize its charge. In the case of a cyclic voltammetry, the current due to this capacitor-like behavior can easily be calculated by:

$$i_{cap} = C\,\nu \qquad \textbf{[3.3.1]}$$

Where i_{cap} is the capacitive current, in A, C is the capacitance of the electrode, in F, and v is the scanning rate of the cyclic voltammetry, in V s^{-1}. As hinted by the above equation, the cyclic voltammogram of an ideal capacitor would show a constant line

through all potential values, depending solely on the capacitance of the electrode and the scan rate used.

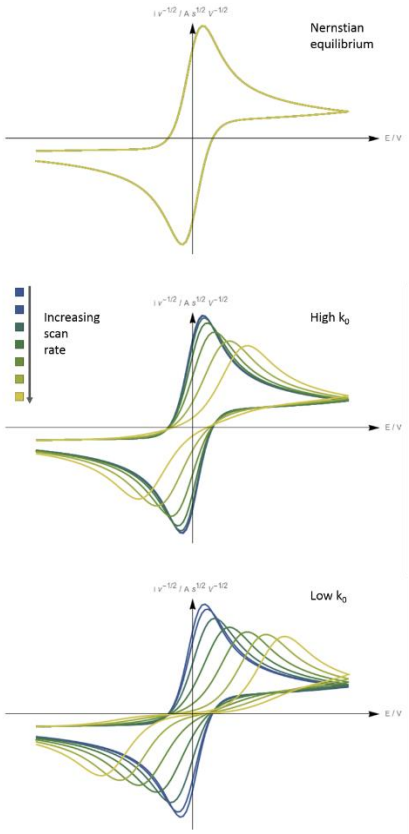

Figure 3.3.2. Simulated cyclic voltammograms for a system under Nernstian equilibrium (top), and with high (middle) and low (bottom) values of kinetic constant. Current values have been normalized by the square root of the scan rate. Capacitive currents not present. Anodic scan first. Axis centered on the equilibrium potential.

The faradaic currents of a typical voltammogram can be seen in Figure 3.3.2. For cyclic voltammetry, both the kinetics of the reaction over the electrode and the diffusion of active species are important when analyzing the curves. As seen in Figure 3.3.2, the voltammograms show a peak in both scanning directions, first when going from lower to higher potentials (anodic scan), and then when going from higher to lower potentials (cathodic scan). At low enough scan rates all systems behave as if they were under Nernstian equilibrium (Figure 3.3.2 top). In this case, the concentration of the electroactive species always follows the expected equilibrium concentration, i.e., the concentration as expected by Nernst's equation:

$$E = E_{eq} - \frac{R\,T}{n\,F}\ln\frac{C_R}{C_O} \qquad [3.3.2]$$

Where $C_{R/O}$ is the concentration of the reduced/oxidized species, respectively, in mol L^{-1}. In this case, the reactions at the electrode are deemed to be instantaneous, such that the kinetics of the electrode's reaction do not play a role. The current is, then, always limited by the diffusion of the species to the surface of the electrode. In the beginning of the experiment enough of the reagent is present on the surface of the electrode, such that the gradient of diffusion is low due to the small difference in concentration between the surface of the electrode and the bulk of the solution. As the potential increases, more and more of the reagent is consumed, until its concentration on the surface reaches zero. Once this happens, the current has reached its maximum value. This happens because the difference in concentration between bulk and surface is at its maximum, and hence the gradient is at its maximum. Afterwards, i.e., in the region after the maximum of the peak, the current is limited by the increase in the diffusion layer on the surface of the electrode. The current starts to decrease, as the active species must diffuse from farther and farther away to reach the electrode and react, and the diffusion gradient decreases because of this increased distance. When the scan direction is reversed, the reverse scenario happens. The species that was previously the product of the electrochemical reaction becomes the reagent, and its concentration is at the highest on the surface of the electrode, since it was being constantly formed on the previous scan. As the potential decreases, it starts being consumed in the reverse reaction, and the same scenario presents itself, with the current increasing (in the opposite direction) until all molecules on the surface are consumed, and starts decreasing as they must diffuse from the bulk of the solution. The fact that, for all scan rates in Figure 3.3.2 top, the voltammograms overlap when the current is normalized by $v^{1/2}$ is a clear indication that the current

throughout the experiment is diffusion controlled, since it means that the current is always proportional to $v^{1/2}$, typical of diffusion-limited systems.

For real systems at high scan rates, the current before the peaks is limited by the kinetics of the reaction. In this case, the current before the peak is also limited by the slow kinetics of the electrochemical reaction. This means that the surface concentration is not dictated by Nernst equation anymore, but rather by how fast the electroactive species can be consumed by the electrochemical reaction. As the scan rate increases, the time allowed for the reaction to happen decreases, and a higher overpotential is necessary in order for all of the species on the electrode's surface to be consumed. This means that the peaks are shifted further apart as the scan rate increases. After the peak, the system is once again diffusion-limited. The fact that the system is no longer diffusion-controlled in the beginning can be seen by the fact that the current is no longer proportional to $v^{1/2}$.

This combination of kinetic and diffusion control over the current response of electrode is what makes cyclic voltammetry a versatile tool for analyzing electrochemical reactions. As shown in Figure 3.3.2 middle and bottom for example, high and low values of the electrode kinetic constant can be told apart by analyzing how the system responds to increasing the scan rate at which the experiment is performed. For a fast enough scan rate, the oxidation and reduction peaks will be separated further apart than for a system under Nernstian state, for which the separation is 59/n mV, with n being the number of electrons involved in the reaction. This effect is more pronounced on reactions with lower kinetics than on reactions with faster kinetics, since slower reactions need more time and/or higher overpotentials to happen at the same extent as faster reactions. This allows for a qualitative analysis of the electrode kinetics.

If, however, the experiment is performed at slow enough rates such that the system is in a quasi-Nernstian state, important information about the diffusion of the

active species can be determined. This is usually done through the Randles–Sevcik equation:

$$i_p = 0.4463 \left(\frac{n^3 F^3}{R T}\right)^{½} A C_a^0 D_a^{½} v^{½} \quad \textbf{[3.3.3]}$$

Where i_p is the peak current, in A, n the number of electrons involved in the reaction, F is Faraday's constant, 96485 C mol^{-1}, R the gas constant, 8.314 J K^{-1} mol^{-1}, T the temperature, in K, A the area, in cm^2, C_a^0 the concentration of species a in the bulk, in mol cm^{-1}, D_a the diffusion coefficient of species a, in cm^2 s^{-1}, and v the scan rate of the experiment, in V s^{-1}. This equation allows the determination of the diffusion coefficient of a species if its concentration is known, for example.

Adapted from reference 124.

3.4 Electrochemical impedance spectroscopy

All the methods described so far involve drastically changing the potential of the working electrode away from equilibrium (typically several hundreds of mV), either by imposing a potential change, or forcing a current to flow through the system, which leads to a change in potential. Instead of using such large perturbations to the system, another approach can be used, where the potential of the electrode is perturbed by a small amount (~10 mV), and the response of the electrode can be measured close to the equilibrium. This is the reasoning behind the electrochemical impedance spectroscopy (EIS). This kind of technique has the ability to probe the electrode without forcing electrochemical reactions to occur, which can be irreversible at times. It also allows for a more in depth analysis of the electrode under different potentials, where the electrode is studied by any ordinary electrochemical technique, and when a potential of interest is reached, the technique is halted, EIS of the electrode is measured, and the previous technique allowed to continue once EIS is finished. This can be done several times during any technique, and often the results of both are combined to better understand what happens in the cell.

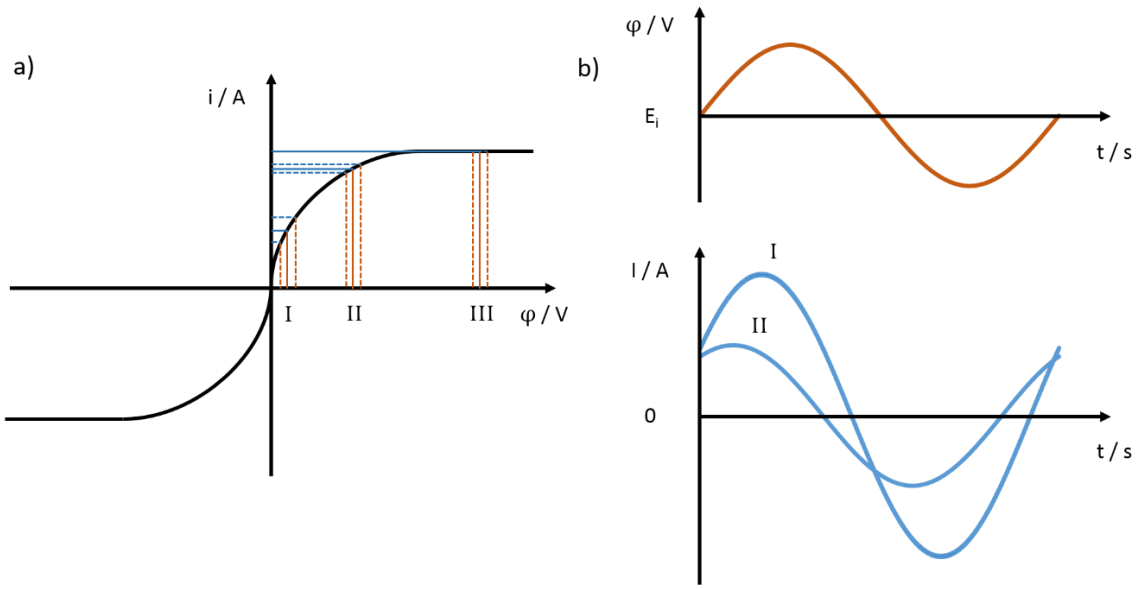

Figure 3.4.1. a) Scheme of a mass transfer limited polarization curve for an ordinary redox couple in solution (black).When a small perturbation (brown dotted lines) is applied in the vicinity of a potential (solid brown line), a corresponding perturbation (blue dotted line) in the current (solid blue line) is measured. b) Sinusoidal potential perturbation (brown) around potential E_i, and different current responses (blue) for the different regions in a).

Figure 3.4.1a shows that when a small perturbation in the potential is applied in the potential of an electrode, a perturbation of the current is also measured, and this changes according to the starting potential.

In a typical EIS experiment, the potential is varied sinusoidally, with different frequencies (hence the name spectroscopy), typically going from 10^6 to 10^{-2} Hz, and the current response measured. The current response also takes a sinusoidal form (Figure 3.4.1b). The shape of the potential perturbation and the current response as a function of time can be expressed, respectively, as:

$$\varphi(t) = \Delta E \sin(2\,\pi\,f\,t) \qquad \textbf{[3.4.1]}$$

$$i(t) = \Delta i(f) \sin(2\,\pi\,f\,t - \theta(f)) \qquad \textbf{[3.4.2]}$$

Where φ(t) and i(t) are, respectively, the potential, in V, and the current, in A, as a function of time t, in s, Δi(f) is the maximum amplitude of the current sine wave, in A, as a function of the frequency f, in Hz, and θ is the phase shift. The current function can be separated into a sine and a cosine function:

$$i(t) = c_1(f)\sin(2\,\pi\,f\,t) + c_2(f)\cos(2\,\pi\,f\,t) \quad \textbf{[3.4.3]}$$

$$c_1(f) = \Delta i(f)\cos\theta(f) \quad \textbf{[3.4.4]}$$

$$c_2(f) = -\Delta i(f)\sin\theta(f) \quad \textbf{[3.4.5]}$$

Where:

$$\Delta i(f) = \sqrt{c_1(f)^2 + c_2(f)^2} \quad \textbf{[3.4.6]}$$

$$\theta(f) = \tan^{-1}\left(-\frac{c_2(f)}{c_1(f)}\right) \quad \textbf{[3.4.7]}$$

$$Z_{total}(f) = \frac{\Delta E}{\Delta \mathrm{i}(f)} \quad \textbf{[3.4.8]}$$

The total impedance is then used, together with the phase values, to calculate the real and imaginary impedances:

$$Z_{Re}(f) = Z_{total}(f)\,\cos\big(\theta(f)\big) \quad \textbf{[3.4.9]}$$

$$Z_{Im}(f) = Z_{total}(f)\,\sin\big(\theta(f)\big) \quad \textbf{[3.4.10]}$$

Where $Z_{Re}(f)$ and $Z_{Im}(f)$ are the real and imaginary impedances as function of frequency, respectively, in Ω. This separation allows the impedance spectra to be plotted as a Nyquist plot, with Z_{Re} as the x-axis, and Z_{Im} as the y-axis.

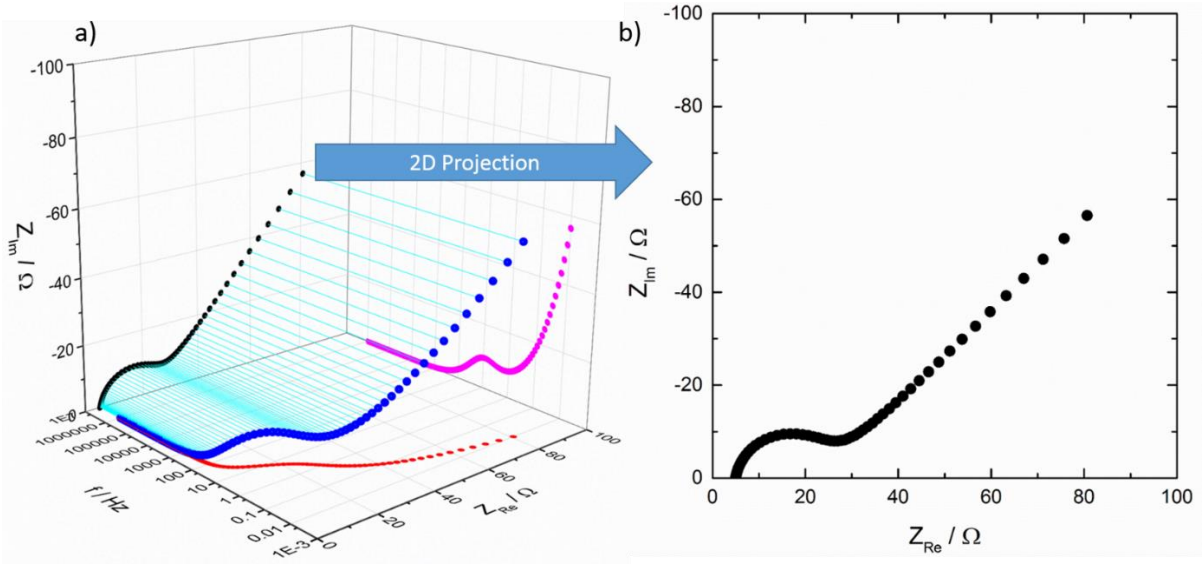

Figure 3.4.2. The impedance response of a typical electrochemical system with O and R dissolved in an electrolyte. a) 3D graph showing the real and imaginary impedances as a function of the frequency. b) The 2D projection of the measured points forms the Nyquist plot.

As shown in Figure 3.4.2, the Nyquist plot is obtained by omitting the frequency values, for clarity's sake, and the frequency values for points of interest can be indicated in the Nyquist plot instead.

It is important to know how do the different electrode processes behave when an oscillating potential is applied to the electrode. The most common processes involved in an electrochemical reaction are two involving the electrochemically active redox couple, namely charge transfer and diffusion, and two involving mainly the support electrolyte, namely double layer charging and ionic migration.

Ions migrate in solution when an electric field is present, since ions are charged particles. In the case of an electric field generated by applying an external potential to a planar electrode in solution (taken to be the origin), and assuming the electric field is uniform, such that only the position of the particle in the x-axis away from the electrode matters, the force on a charged particle in the solution can be described as:

$$F_{e,a}(l) = -\, z_a\, e_0\, \overrightarrow{E(l)} = -\, z_a\, e_0\, \frac{d\varphi}{dx}\bigg|_{x=l} \qquad \textbf{[3.4.11]}$$

Where $F_{e,a}$ is the electrostatic force on the particle a, in N, z_a is the charge of the particle a, e_0 is the elementary charge, 1.602 10^{-19} C, and $\overrightarrow{E(l)}$ is the electric field at a distance l from the electrode, in V m^{-1}, and can be calculated as the local derivative of the electrode potential φ, in V, by the distance to the electrode x, in m, at a distance l. When the particle is in movement, the only forces acting on it are the electrostatic force and the friction force:

$$F_{f,a} = - f_a \, v_{d,a} \qquad \textbf{[3.4.12]}$$

Where $F_{f,a}$ is the friction force on particle a, in N, f_a is the friction coefficient of particle a, in N s m^{-1}, and $v_{d,a}$ is the drift velocity of particle a, in m s^{-1}. Under steady state conditions, the net force over the particle is zero, such that:

$$v_{d,a} = - z_a \frac{e_0}{f_a} \left.\frac{d\varphi}{dx}\right|_x = - \mu_a \left.\frac{d\varphi}{dx}\right|_x \qquad \textbf{[3.4.13]}$$

Where μ_a is the electrical mobility of particle a, in m^2 V^{-1} s^{-1}. The total current flowing through the cell due to ion migration can then be calculated by summing the flux of all species on the surface of the electrode (x = 0) multiplied by the respective charges:

$$i_{mig} = A \left.\frac{d\varphi}{dx}\right|_{x=0} \sum_a (- z_a \, \lambda_a \, C_a) \qquad \textbf{[3.4.14]}$$

Where λ_a is the molar conductivity of the species a, in S cm^2 mol^{-1}. The migration current is then a function of potential profile inside the electrolyte, which can be thought of as being linear between the working and reference electrodes. The migration current then becomes:

$$i_{mig}(E) = A \frac{\Delta\varphi}{d} \sum_a (- z_a \, \lambda_a \, C_a) \qquad \textbf{[3.4.15]}$$

For an oscillating potential $\Delta\varphi(t) = \Delta E \sin(2 \pi f t)$, the current response will be:

$$i_{mig}(t) = \left(A \frac{\Delta E}{d} \sum_a (- z_a \, \lambda_a \, C_a) \right) \sin(2 \pi f t) \qquad \textbf{[3.4.16]}$$

The response of the migration current is also sinusoidal, and the values of c_1 and c_2 can be calculated, from which the values of Δi, $Z_{total,mig}$ (the total impedance due to migration), and θ can be calculated:

$$\Delta i = c_1 = \left(\frac{A}{d}\sum_a (-z_a \lambda_a C_a)\right)\Delta E \quad \textbf{[3.4.17]}$$

$$Z_{total,mig} = \frac{\Delta E}{\Delta i} = \left(\frac{A}{d}\sum_a (-z_a \lambda_a C_a)\right)^{-1} \quad \textbf{[3.4.18]}$$

$$\theta(f) = \tan^{-1}\left(-\frac{0}{c_1}\right) = 0 \quad \textbf{[3.4.19]}$$

This result is similar to the results obtained when using a resistor with resistance R that follows Ohm's law:

$$i(t) = \frac{E(t)}{R} = \frac{\Delta E}{R}\sin(2\pi f t);\ c_1 = \frac{\Delta E}{R}; c_2 = 0 \quad \textbf{[3.4.20]}$$

$$\Delta i = c_1 = \frac{\Delta E}{R} \quad \textbf{[3.4.21]}$$

$$Z_{total,R} = \frac{\Delta E}{\Delta i} = R \quad \textbf{[3.4.22]}$$

$$\theta(f) = \tan^{-1}\left(-\frac{0}{c_1}\right) = 0 \quad \textbf{[3.4.23]}$$

This means that the behavior of ions migrating through a solution can be effectively simulated by as a resistor. The conductivity of an electrolyte can also be calculated in this way:

$$R = \kappa^{-1}\frac{d}{A} = \left(\sum_a (-z_a \lambda_a C_a)\right)^{-1}\frac{d}{A} \quad \textbf{[3.4.24]}$$

$$\kappa = \sum_a (-z_a \lambda_a C_a) \quad \textbf{[3.4.25]}$$

Where κ is the conductivity of the solution, in S m^{-1}. It is also important to notice that, since the phase is always equal to zero, a pure resistor should only show real impedance, as expected from equations **[3.4.9]** and **[3.4.10]**.

The second process involving the electrolyte describes the behavior of ions when they reach an electrified interface, forming an electrical double-layer. The first and simplest mathematical approach to describe such a layer on the surface of a conducting electrode was first described by Helmholtz[125], and assumes that ions will migrate to the surface and form a two-dimensional plane of ions that completely neutralize the electrical charge of the electrode, i.e., the electrical field in solution after this first plane is essentially null. This layer of ions is commonly called the outer Helmholtz plane, as opposed to ions that chemically adsorb on the surface, forming the inner Helmholtz plane.

The surface of the electrode can be imagined as being an infinite plane in comparison to the ion sizes. The electric field felt by the ions in solution can then be calculated as:

$$\vec{E}_{ele} = \frac{q_{ele}}{2\,A\,\varepsilon} = \left.\frac{d\varphi}{dx}\right|_x \qquad \textbf{[3.4.26]}$$

Where $\vec{E}_{ele}$ is the electric field due to the electrode, in V m^{-1}, q_{ele} is the charge in the electrode, in C, A is the area of the electrode, in m^2, and ε is the permittivity of the medium, in F m^{-1}. The double-layer can also be imagined as a plane bigger than the individual ions that form it, such that the electric field it generates is equal to that of the electrode. The total charge in the electrode is then a function of the electrode's potential as:

$$q = \frac{A\,\varepsilon}{d}\varphi \qquad \textbf{[3.4.27]}$$

Where d is the double-layer thickness, in m. The current in such a system can be easily calculated as the change in charge over time:

$$i(t) = \frac{A\,\varepsilon\,\Delta E}{d} 2\,\pi f\ \cos(2\,\pi\,f\,t) \qquad \textbf{[3.4.28]}$$

$$\Delta i = \ c_2(f) = \frac{A\,\varepsilon}{d}\Delta E\ 2\,\pi f \qquad \textbf{[3.4.29]}$$

$$Z_{total,dl} = \frac{\Delta E}{\Delta i} = \frac{d}{A\,\varepsilon}\,\frac{1}{2\,\pi\,f} \quad \textbf{[3.4.30]}$$

$$\theta(f) = \tan^{-1}\left(\lim_{c_1 \to 0^+} -\frac{c_2(f)}{c_1}\right) = \tan^{-1}(-\infty) = -\frac{\pi}{2} \quad \textbf{[3.4.31]}$$

This is similar to the results obtained for a parallel-plate capacitor, for which:

$$i(t) = C\,\frac{dE(t)}{dt} = \Delta E\; C\; 2\,\pi f\; \cos(2\,\pi\,f\,t) \quad \textbf{[3.4.32]}$$

$$\Delta i = c_2(f) = C\;\Delta E\;2\,\pi f \quad \textbf{[3.4.33]}$$

$$Z_{total,C} = \frac{\Delta E}{\Delta i} = \frac{1}{C\;2\,\pi\,f} \quad \textbf{[3.4.34]}$$

$$\theta(f) = \tan^{-1}\left(\lim_{c_1 \to 0^+} -\frac{c_2(f)}{c_1}\right) = -\frac{\pi}{2} \quad \textbf{[3.4.35]}$$

Where C is the capacitance of the parallel-plate capacitor, in F, such that:

$$C_{dl} = \frac{A\,\varepsilon}{d} \quad \textbf{[3.4.36]}$$

This means that the double-layer formed between the electrode and the electrolyte effectively behaves like a capacitor, similar to how the migration of ions through the electrolyte behaves like a resistor. Also similar to the Ohmic resistor, a pure capacitor does not show any impedance on the real axis, having only imaginary impedance, as expected from equations **[3.4.9]** and **[3.4.10]**.

The third process which involves species in the solution regards charge transfer to the electrochemically active species. Since the perturbation in the system is small, the concentrations over the electrode surface do not change significantly compared to the concentration in the bulk, such that the current due to a faradaic reaction is related to the potential through the Butler-Volmer equation. For small perturbations, the behavior of the current is approximately linear with the change in voltage, such that:

$$i(\eta) = i_0\,\frac{F\,\eta}{R\,T} \quad \textbf{[3.4.37]}$$

For an oscillating overpotential $\eta(t) = \Delta E\ \sin(2\,\pi\,f\,t)$:

$$i(t) = i_0 \frac{F\,\Delta E}{R\,T} \sin(2\,\pi\,f\,t) \quad \textbf{[3.4.38]}$$

$$\Delta i = c_1 = i_0 \frac{F\,\Delta E}{R\,T} \quad \textbf{[3.4.39]}$$

$$Z_{total,ct} = \frac{\Delta E}{\Delta i} = \frac{R\,T}{F\,i_0} \quad \textbf{[3.4.40]}$$

$$\theta(f) = \tan^{-1}\left(-\frac{0}{c_1}\right) = 0 \quad \textbf{[3.4.41]}$$

As in the case of ion migration in the electrolyte, the charge transfer to and from an electrode behaves like a resistor, and:

$$R_{ct} = \frac{R\,T}{F\,i_0} \quad \textbf{[3.4.42]}$$

Where R_{ct} is the charge transfer resistance, in Ω.

The final process is the diffusion of the active species from the bulk of the electrolyte to its surface. The first solution to such a problem was derived by Warburg[126], which lead the impedance due to diffusion to also be called Warburg impedance. The equation was solved under the boundary condition that the system is in a Nernstian state, such that any variation in potential leads to an immediate change in surface concentration of the active species. It was also solved assuming that the only small overpotentials are used, such that the change in surface concentration is small in comparison to the original concentration of the active species. Under such circumstances, the current response, due to diffusion, to a sinusoidal potential is:

$$i_{diff} = \frac{\Delta E\,\sqrt{2\,\pi\,f}}{2\,\sigma} \sin(2\,\pi\,f) + \frac{\Delta E\,\sqrt{2\,\pi\,f}}{2\,\sigma} \cos(2\,\pi\,f) \quad \textbf{[3.4.43]}$$

Where σ is the so called Warburg coefficient:

$$\sigma = \frac{R\,T}{A\,n^2F^2\sqrt{2}}\left(\frac{1}{D_O^{½}\,C_O^0} + \frac{1}{D_R^{½}\,C_R^0}\right) \quad \textbf{[3.4.44]}$$

With $D_{O/R}$ being the diffusion coefficient for the oxidized/reduced species, in $cm^2\ s^{-1}$, and $C^0_{O/R}$ the bulk concentration of the oxidized/reduced species, in mol cm^{-3}. From equation **[3.4.43]**, the impedance and phase shift can be calculated:

$$\Delta i = \frac{\Delta E \sqrt{\pi f}}{\sigma} \qquad \textbf{[3.4.45]}$$

$$Z_{total,diff} = \frac{\Delta E}{\Delta i} = \frac{\sigma}{\sqrt{\pi f}} \qquad \textbf{[3.4.46]}$$

$$\theta(f) = \tan^{-1}\left(-\frac{\frac{\Delta E \sqrt{2\,\pi f}}{2\,\sigma}}{\frac{\Delta E \sqrt{2\,\pi f}}{2\,\sigma}} \right) = \tan^{-1}(-1) = -\frac{\pi}{4} \qquad \textbf{[3.4.47]}$$

The Warburg impedance has a distinctive characteristic in the fact that its phase is shifted by -π/4, which is unlike that of any electrical component. The impedance response of diffusion can be, however, simulated by an electric circuit similar to that of a transmission line, using a series of resistors in series with parallel capacitors[127]. A simpler approach is to use a constant phase element (CPE). The CPE is a circuit element invented to simulate the real-world impedance behavior of electrochemical systems. Its main characteristic is that its phase can have any value between 0 and –π/2, and, like for other simple, single components, the phase is independent of the frequency. Its impedance can be calculated by:

$$Z_{total,CPE} = \frac{1}{Q_0(2\,\pi\,f)^n} \qquad \textbf{[3.4.48]}$$

$$\theta(f) = -\frac{\pi}{2}\,n \qquad \textbf{[3.4.49]}$$

Where Q_0 and n are adjusting parameters, with Q_0 having units of $s^n\ \Omega^{-1}$, and n being a pure number between 0 and 1. When used to simulate the diffusion impedance, the adjusting parameters take the following values:

$$Q_{0,diff} = \frac{1}{\sigma\sqrt{2}}\ ;\ n = \frac{1}{2} \qquad \textbf{[3.4.50]}$$

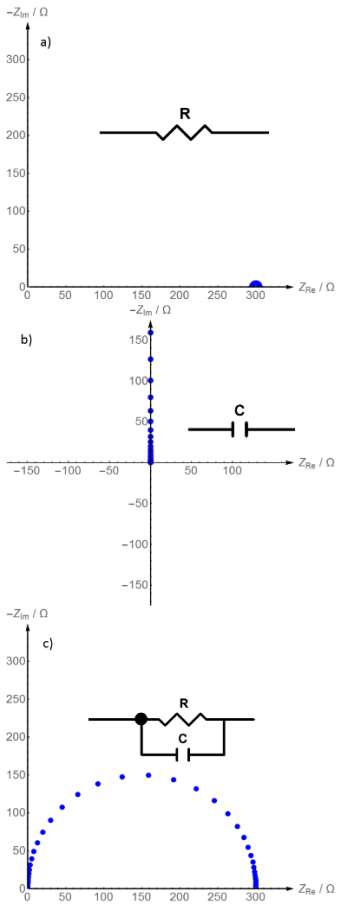

Figure 3.4.3. Impedance spectra of a) a resistor (R = 300 Ω), b) a capacitor (C = 1 mF), and c) a parallel combination of both elements.

So far, all electrochemical processes have been described in terms of equivalent electric components. Just as in the case of a normal electrical circuit, these components can be combined to simulate more complex systems, where various processes take place at once. This means that a real electrochemical system can be simulated by the proper arrangements of different electrical components in an equivalent circuit. A simple example of an arrangement like this is when a resistor and a capacitor are connected in parallel to one another (Figure 3.4.3). In this case, they both are subjected to the same electric potential $\Delta E \sin(2\pi f t)$, such that the current through the resistor and the capacitor are given by equations **[3.4.20]** and **[3.4.32]**, respectively. Since they are connected in parallel, the total current through the circuit is a sum of both currents:

$$i_{parallel}(t) = \frac{\Delta E}{R}\sin(2\,\pi\,f\,t) + \Delta E\;C\;2\,\pi f\;\cos(2\,\pi\,f\,t) \quad \textbf{[3.4.51]}$$

Using equations **[3.4.3]** through **[3.4.10]**, the total impedance, phase shift, and real and imaginary impedances as a function of frequency for this system can be calculated as:

$$Z_{parallel,total}(f) = \frac{R}{\sqrt{1 + (R\;C\;2\,\pi\,f)^2}} \quad \textbf{[3.4.52]}$$

$$\theta(f) = \tan^{-1}(-R\;C\;2\,\pi\,f) \quad \textbf{[3.4.53]}$$

$$Z_{parallel,real}(f) = \frac{R}{1 + (R\;C\;2\,\pi\,f)^2} \quad \textbf{[3.4.54]}$$

$$Z_{parallel,imaginary}(f) = -\frac{R^2\;C\;2\,\pi\,f}{1 + (R\;C\;2\,\pi\,f)^2} \quad \textbf{[3.4.55]}$$

It is interesting to notice that, although, for example, the impedance of the resistor is the only one with a real component in the parallel circuit, and it does not change with frequency, the impedance of the circuit as whole shows a dependence of both the real and imaginary part with frequency. The impedance spectrum of a circuit can have a completely different shape as would be expected from just looking at the individual components alone.

A more straightforward way of calculating the impedance of circuits is the complex number notation for them. In this case, the impedance $Z_{complex}$ of an element is equal to:

$$Z_{complex} = Z_{Re} + j\,Z_{Im} \quad \textbf{[3.4.56]}$$

Where Z_{Re} and Z_{Im} are the real and imaginary impedances, respectively, and j is the imaginary unit, $\sqrt{-1}$. In this case, the complex impedances of different elements can be combined as for a normal electrical circuit, with the impedance of elements connected in series being added directly, and those in parallel being added inversely:

$$Z_{complex,series} = \sum_i Z_{complex,i} \quad \textbf{[3.4.57]}$$

$$Z^{-1}_{complex,parallel} = \sum_i Z^{-1}_{complex,i} \qquad \textbf{[3.4.58]}$$

With this in mind, the equivalent circuit of an electrochemical system can be easily calculated.

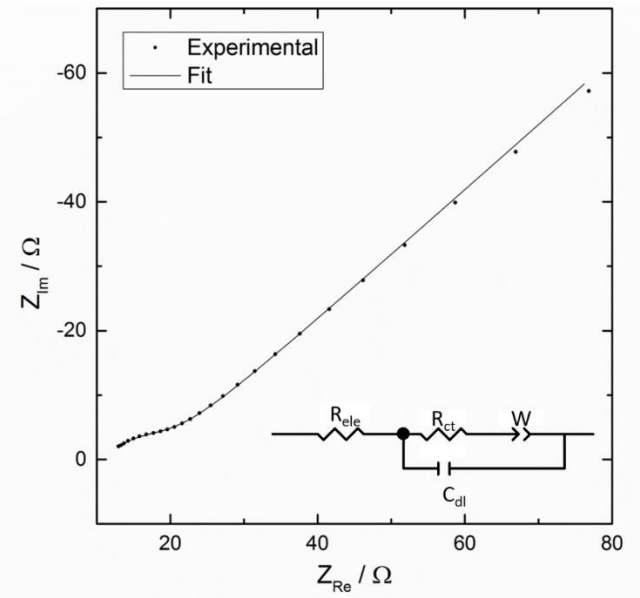

Figure 3.4.4. Electrochemical impedance spectrum of a reversible electrochemical pair, as well as the fitted values using the Randles equivalent circuit (inset)

Figure 3.4.4 shows the equivalent circuit of an electrode similar to the one described in Figure 3.4.2. This circuit was first proposed by Randles[128], such that it is often called a Randles circuit. It is important to understand the layout of this circuit, as it is physically related to the processes previously described. The first and often most important part is the charge transfer, which, as shown in equation **[3.4.42]**, behaves like a resistor (R_{ct}). As pointed out in Figure 3.4.2, after the reaction takes place, there will be a difference in concentration of the species on the electrode's surface in relation to the concentrations of the unperturbed system. This means that the consumed species must diffuse from the bulk of the electrolyte to the surface of the electrode, and the generated species from the surface to the bulk. As such, the diffusion process is always coupled to the charge transfer process. In the equivalent circuit, this coupling is represented by

adding different elements in series, such that the CPE representing the diffusion process (W) is in series with R_{ct}.

The charge and discharge of the double layer capacitor is independent of the charge transfer reactions between dissolved species and the electrode. In the same way that coupled reactions are represented by electrical elements in series, independent reactions are represented by parallel ones. As such, the capacitor representing the double-layer is placed parallel to the elements that compose the charge transfer circuit.

Lastly, in order for both of these processes to happen, there must be the migration of ions to and from the bulk of the solution in order to keep the system electrically neutral. In the case of the double-layer capacity, this happens because the ions in solution are attracted or repelled by the injection or removal of electrons in the electrode. For the charge transfer reactions, there is injection/withdraw of electrons to/from the solution, causing a local charge imbalance. This causes ions around the species that gained/lost electrons to move away or towards via migration. In this way, both the double-layer and the charge transfer processes are coupled with electrolyte migration, such that the resistor that represents the electrolyte (R_{ele}) is placed in series with the parallel circuit.

The Randles circuit is a very common equivalent circuit, which can appropriately describe the behavior of simple systems like the one pointed above, such as an electrochemically active pair dissolved in a high concentration, highly conducting electrolyte. In practice, systems will often be more complicated, with electroactive species in the solid state, for example, or where a passivating film can form over the electrode, or inhomogeneities are present on the electrode, to name a few. All these differences will change the way the system behaves towards the oscillating potential.

One of the most common adjust that has to be made for real systems is that the electrodes are usually not perfectly flat, but rather show a rough surface morphology.

This roughness means that, for example, the double-layer forms at different time intervals, depending on how easy or hard it is for the ions of the electrolyte to approach the electrode's surface. Simulating this inhomogeneity would require using a circuit with many parallel capacitors, representing the different areas, with resistors connecting them, which represent the increased distance the ions have to migrate. Such an arrangement is similar to a transmission line, as was the case of the Warburg element. Just like in that case, this transmission line is more easily represented by a CPE, such that, for real systems, the double-layer capacitor in Figure 3.4.4 is changed to a CPE. In this case, the inhomogeneity of the electrode can be qualitatively measured by the value of n of the CPE. An ideal capacitor is a CPE with n = 1, such that a double-layer CPE with n close to 1 indicates a relatively homogeneous surface, whereas a lower value will mean a rougher surface.

Finally, another electrical component that can appear in electrochemical systems must be discussed, the inductor. In electrical systems, an inductor is often described as a coil of wire wrapped around a core material. Its electrical impedance is given by $Z_{total,ind} = 2\,\pi\,f\,L$ and the phase shift by $\theta(f) = +\frac{\pi}{2}$, where L is the inductance of the material, in H. The impedance of the inductor has a behavior opposite to that of the capacitor, with impedance decreasing for lower perturbation frequency. The most notable feature, however, is that it has a phase shift of $+\pi/2$, while all other elements described so far have a phase shift between 0 and $-\pi/2$. As such, the presence of an inductor can be easily recognized in an electrochemical impedance spectrum, appearing as positive values of Z_{Im} in the Nyquist plot (Figure 3.4.2). Unlikely the case of the capacitor or a resistor, the electrochemical processes that lead to an inductor-like behavior are not so well understood. It is generally accepted that this is due to the presence of intermediate species adsorbed into the surface of the electrode[129,130], but no

simple equation relating the rate of adsorption with the value of the inductance, for example, has been derived.

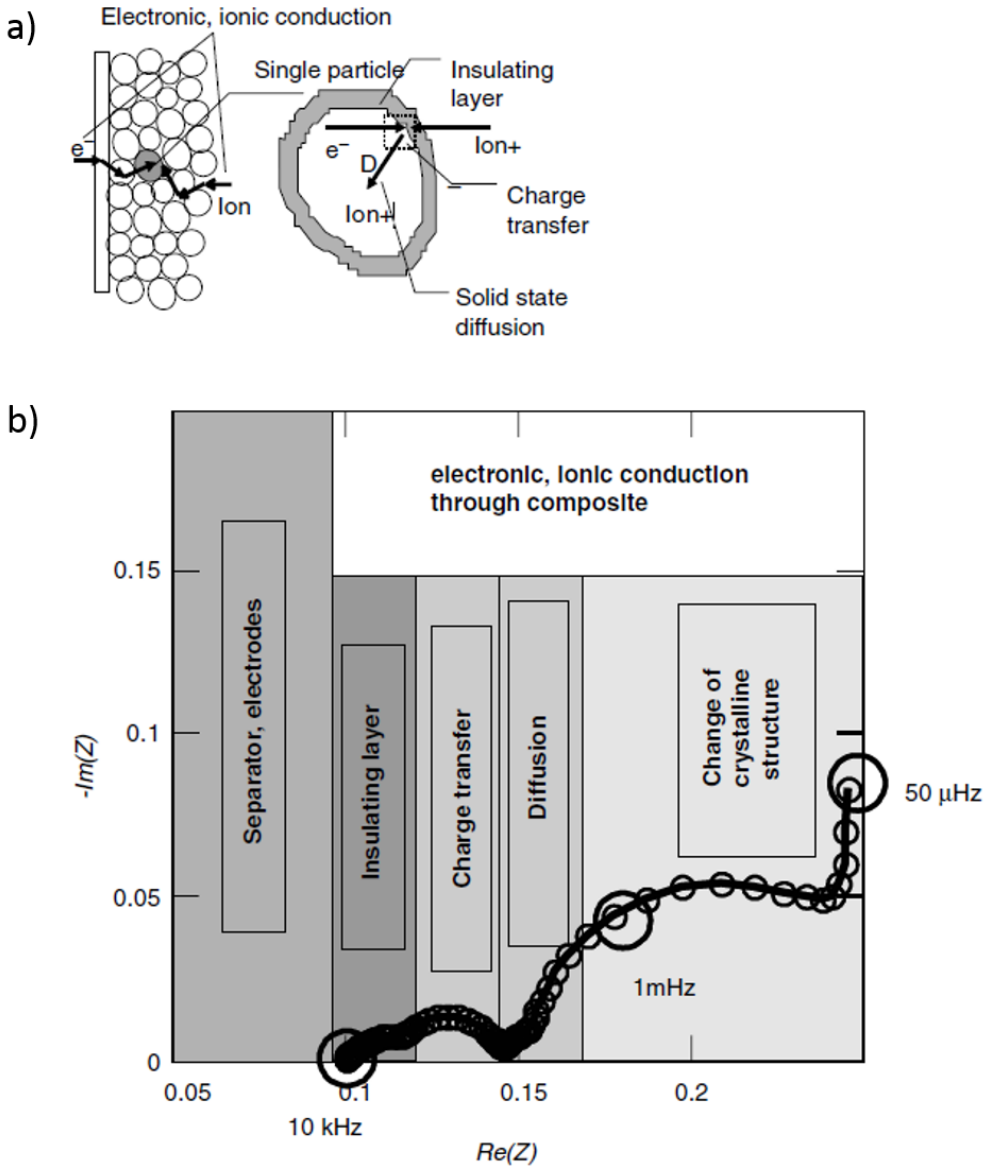

Figure 3.4.5. a) Typical processes involved in charge transfer for insertion-type electrode materials and b) the corresponding impedance spectrum related to these processes.

So far, the system described was assumed to have the electroactive species dissolved in the electrolyte. Some systems, however, do not behave as such, having rather the electroactive species in the solid state. One such system, which is of great interest to electrochemists, is that of solid insertion materials, which are often used as active material for the electrodes of lithium-ion batteries. The processes and impedance of such

system differ greatly from those of liquid systems (Figure 3.4.5). In a typical insertion electrode, both the electron, and the ion which compensates for the electron charge (and is inserted into the material) must travel through the porous network which makes the electrode. The material particle is then partially reduced (it accepts one electron), and the ion is inserted into it. The ion has to diffuse until it reaches the electroactive center which was previously reduced (Figure 3.4.5a). All these processes have impedances related to them, such that the resulting spectrum is different then, for example, the one for the Randles circuit, as seen in Figure 3.4.5b.

Adapted from references 131 and 132.

3.5 Vibrational spectroscopic methods – Infrared and Raman

Vibrational spectroscopy is a very powerful tool for studying most materials. It is based on the fact that the atoms in a chemical bond, for example, have a natural tendency to vibrate, and the energy with which they vibrate depends, among others, on the kinds of atoms present in the bond, the type of bond (single, double, etc.), and the environment around the bond.

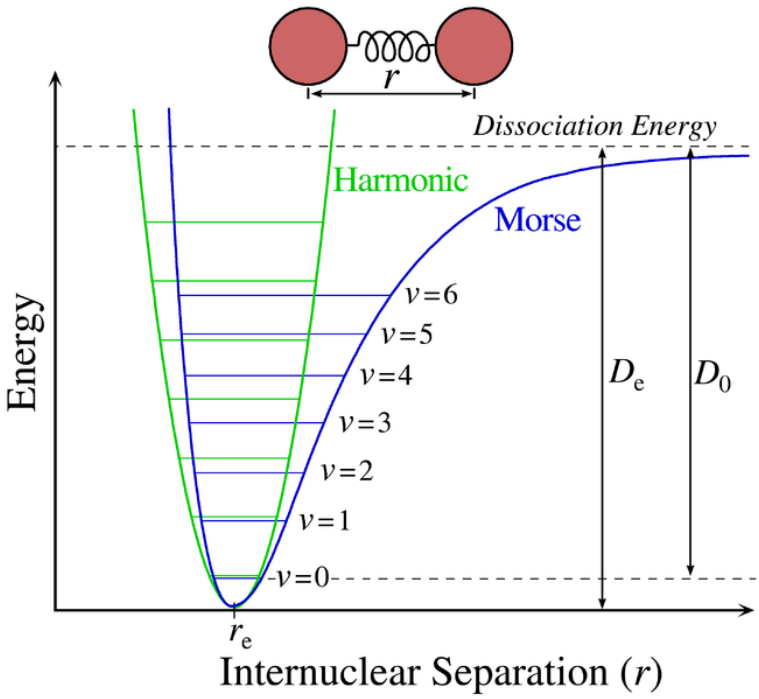

Figure 3.5.1. Potential curves and energy levels for a classical harmonic oscillator (green) and for an oscillator following the Morse potential (blue). In these approximations a diatomic molecule can be approximated to two weights held together by a spring (inset, above).

A very common way to model molecules is to consider atoms as weights held together by a mass-less spring. In this case, a simple diatomic molecule (for example H_2) would be modeled as two weights being held together by a spring (Figure 3.5.1, inset). In this case, the molecule could be approximated to a classical oscillator (Figure 3.5.1, green), the energy of which is given by $E = k\,(r - r_e)^2$, where k is strength of the spring, in N m^{-1}. This is however a very unrealistic, albeit simple, model to a real chemical bond. This can be specially noted at big displacements from equilibrium (r_e). If the atoms of a molecule get too close, they will start repelling each other, such that the energy needed to bring them closer starts increasing much more rapidly than what the harmonic oscillator predicts. On the other side, if the atoms get pulled too far apart, the bond will break, and no energy will be needed to drive them further away from each other. In this sense, the Morse potential (Figure 3.5.1, blue), is a much better approximation to the

behavior of a real molecule, the energy of which is calculated as $E = D_e\left(1 - e^{-\sqrt{\frac{k}{2D_e}}(r-r_e)}\right)^2$. In both cases, the potential curve can be used in the Schrödinger's equation, which yields the separation between the different vibrational energy levels. This separation between the energy levels depends on the nature of the atoms involved in the bond, the strength of the bond, and the environment around the bond, since all these parameters can affect k and/or D_e. As such, each kind of bond has different vibrational energy levels, and can be distinguished from other ones. Moreover, the different kinds of bonds identified in a vibrational spectrum can be put together to puzzle out what the compound under investigation consists of.

Finally, the key aspect of this type of spectroscopy is that the energy uptake and release are quantized, and followed by the absorption or emission of a photon, respectively. This means that the energy transitions can be studied by analyzing the energy of the photons involved in these processes. For most molecules, these transitions are in the same energy range as electromagnetic radiation in the mid-infrared part of the spectrum (wavenumbers between 4000 and 400 cm^{-1}).

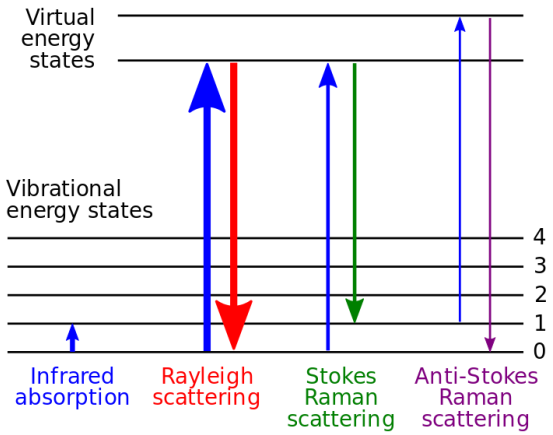

Figure 3.5.2. Scheme of transition between different vibrational states through direct (infrared absorption) and indirect (Raman scattering) transition.

Figure 3.5.2 shows the different ways a compound can interact with electromagnetic radiation and change its energy state. Infrared spectroscopy takes advantage of the direct transition, whereby the compound absorbs the energy from the electromagnetic radiation and is excited to the next level. In this case, the sample is illuminated with infrared light with different wavelengths, and the absorption of the sample at each wavelength measured. In Raman spectroscopy, the excitation is indirect. Light with much more energy than the one required for the vibrational transition (usually in the ultraviolet-visible part of the spectrum) is used, which brings the compound to a virtual state well above the energy of the vibrational states. It then releases this energy also in the form of light. For the most part, the molecule will come back to the ground vibrational state, and the light that was absorbed is released with the same, through a process called Rayleigh scattering. Some of the molecules, however, will fall back to an excited state, and the energy of the light emitted will be equal to the light absorbed minus the energy required to make the vibrational transition, which is the key process that enables Raman spectroscopy. This process is also called Stokes scattering, and has a much lower prevalence than Rayleigh scattering. Finally, some of the molecules are naturally already in an excited stated. Those molecules can also absorb radiation, fall back to the ground state, and emit it back with more energy than the original one, corresponding to the energy of the original radiation plus the energy of the transition. This process is called an anti-Stokes scattering, and has an even smaller prevalence than Stokes scattering.

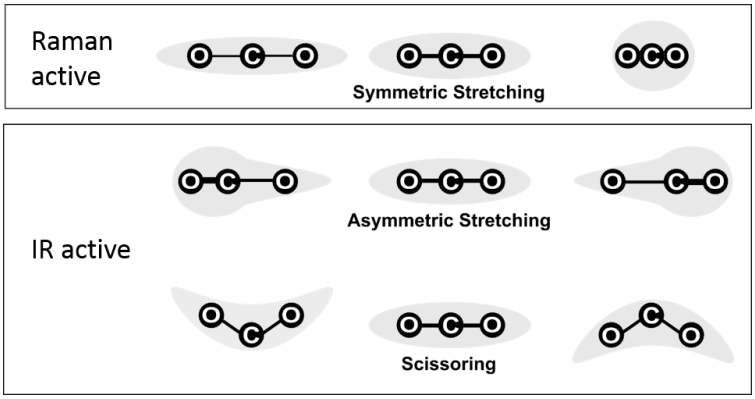

Figure 3.5.3. Example of the three vibration modes of a CO_2 molecule, showing which are present in the Raman spectrum (above) and which are present in the infrared spectrum (below). The grey area around the molecule schematically represents its electronic cloud.

One key difference between Raman and infrared (IR) transitions is that they have different selection rules, with different vibrations being active for each technique. In the case of IR active transitions, a change in the dipole moment of the molecule must happen in order for that vibration mode to be active in IR. Figure 3.5.3 shows two vibration modes of the CO_2 molecule which are IR active, asymmetric stretching and scissoring, as well as the electronic cloud around the molecule during each vibration. For Raman active vibrations, an asymmetric change in polarizability of the molecule is required instead.

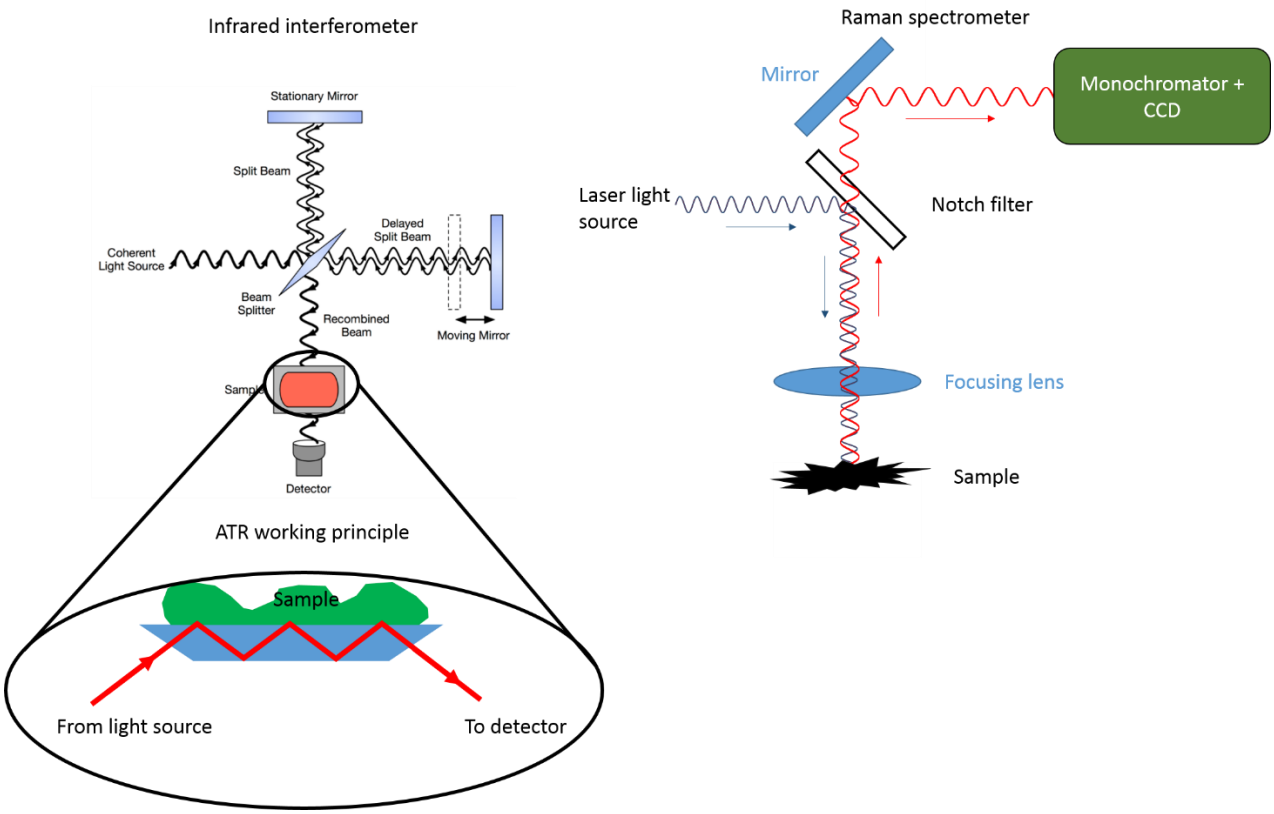

Figure 3.5.4. Scheme of an infrared interferometer with attenuated total reflectance (FTIR-ATR, left) and a Raman spectrometer (right).

Figure 3.5.4 shows a schematic representation of how the devices for both measurements work. Infrared spectra are often obtained through Fourier-transform infrared spectroscopy (FTIR), where the light source emits light with all the wavelengths to be tested. The beam is then split into two paths, and in both cases the new beams are reflected back by mirrors to be recombined at the beam splitter. The recombined beam is then shone through the sample and analyzed by the detector. One of the mirrors can be shifted back and forth, changing the actual path length in that branch, and hence the nature of the recombined beam. When both branches have the same length, all the wavelengths interfere constructively, and the recombined beam has the maximum intensity. When the length of one of the branches changes, the interference at each wavelength will be different, creating changes in intensity on the recombined beam. Finally, the intensity at each mirror position gives rise to an interferogram, which can

be analyzed by means of a Fourier transform to calculate the absorption at each wavelength and yield the final spectrum.

The most straightforward way to perform FTIR is in the attenuated total reflectance (ATR) mode (Figure 3.5.4, left). In it, the sample is placed over a crystal, in which the infrared beam is shined. Due to the incident angle, the beam suffers total reflectance, and bounces back and forth in the crystal. A certain amount of photons from the beam gets absorbed by the sample each time the beam reflects from the crystal face in contact with it, until it exits the crystal and is analyzed by the detector. This mode allows for simple sample preparation, since the only requirement is that it has a good contact with the face of the crystal.

In the case of Raman spectroscopy, the approach is more straightforward and similar to other dispersive spectroscopic methods. Light from a monochromatic laser source is shone through a notch filter, which acts both like a mirror and filter, redirecting the light to a lens before going to the sample. The sample absorbs the light and emits it back in many directions, and the lens focus it back to the appropriate path so it can go back to the notch filter. In this case, the filter removes light of a specific wavelength, usually the wave length of the excitation laser. This is done to remove the signal coming from Rayleigh scattering, which is usual much stronger than that of the Stokes scattering. Finally, the filtered signal goes through a monochromator (usually a grating or prism), which separates the incoming signal according to wavelength, and is analyzed by a charge-coupled device. One interesting aspect of Raman spectroscopy is that the focusing lens can be that of a microscope, which allows the Raman spectrum to be obtained from a single point in the sample, i.e., the spectrum can be obtained for different points in space of the sample allowing mapping.

Adapted from 133.

3.6 X-ray photoelectron spectroscopy

X-Ray photoelectron spectroscopy (XPS) is a very useful technique to analyze the surface composition of different samples, yielding information both on the types of atoms that are contained in a sample, as well as on the local environment of those atoms. The technique itself is based on the photoelectric effect.

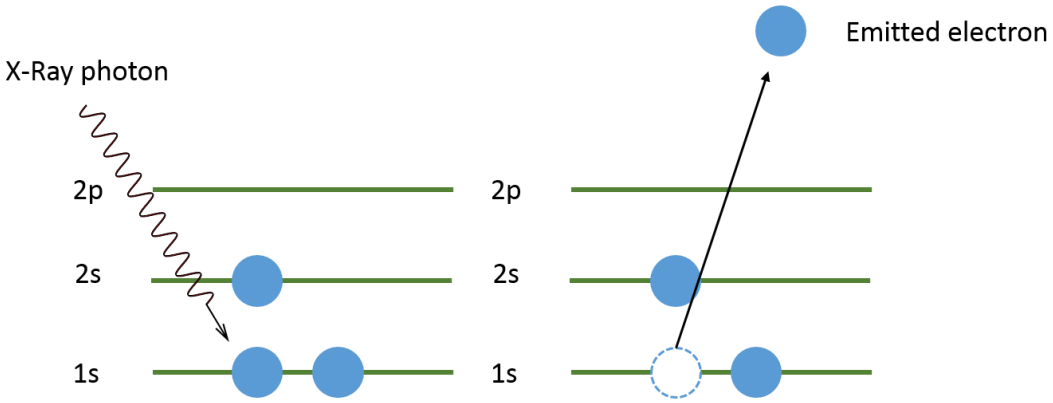

Figure 3.6.1. Scheme of electrons (blue circles) in the different energy levels of a lithium atom, and how the photoelectric effect works on it: the x-ray photon is absorbed by an electron (left), which gets ejected from the atom (right).

The photoelectric effect (Figure 3.6.1) is a phenomenon where photons of electromagnetic radiation eject electrons from a material if the energy of the photon is higher then the energy required to eject the electron. The emitted electron will have a kinetic energy equal to the energy of the incident photon minus the energy required to eject the electron. XPS uses X-Ray radiation to emit electrons, since x-rays have more energy than the binding energy of electrons in a variety of atoms.

Binding energy is a measure of how much energy is required to remove an electron from the orbit of an atom. It is affected not only by the nature of the atom itself, but also by the environment around it. The binding energy can be calculated as $BE = h\nu - KE - \phi$, where h is the Planck constant, 6.626 10^{-34} J s, and v is the frequency of the radiation, in Hz, i.e., KE the kinetic energy of the emitter electron, and ϕ the work function of the spectrometer, both in J.

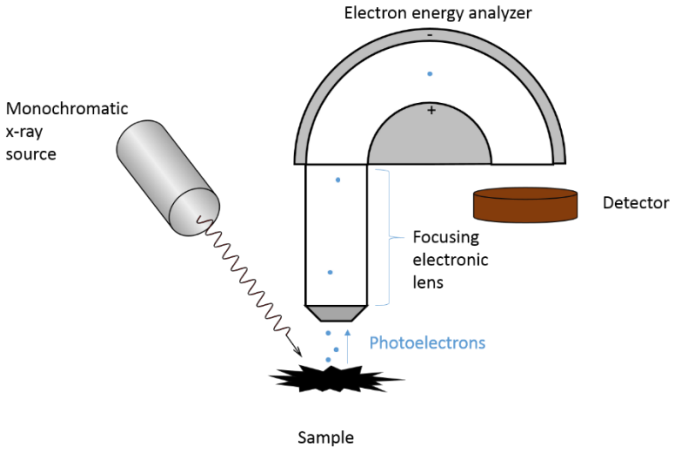

Figure 3.6.2. Scheme of an x-ray photoelectron spectrometer.

Figure 3.6.2 shows the basic setup of an XPS spectrometer. Ideally, the sample is illuminated with monochromatic x-ray only, to enable a precise calculation of the incident photon's energy. The x-rays absorbed by the sample trigger the emission of photoelectrons, which are then collected near the surface of the sample, and focused into the energy analyzer. The energy analyzer is used to select the velocity (i.e., kinetic energy) of the electrons before they can reach the detector. This is accomplished by two curved plates inside the analyzer, one positively and one negatively charged. By controlling the voltage difference, the centripetal force the electrons feel can also be controlled such that only electrons with the desired speed will be able to reach the detector. Electrons going too fast are not able to make the curve and reach the outer plate, while electrons going too slow will curve too much and collide with the inner plate. To ensure that the electrons do not collide with anything on their way to the detector, the whole assembly is held at ultra high vacuum, minimizing the chance of electron loss. Finally, as mentioned before, this technique is suitable for analysis of the surface of a sample only, usually with a depth from 1 to 10 nm. This is because any electron generated too deep into the sample will interact with the rest of the sample above it before it can successfully escape into the vacuum. Analysis at different depths are still possible, though they have to be done by removing the topmost layer. This is commonly performed

in situ by bombarding the sample with highly energetic ionized argon atoms. This can be done in a controlled manner to etch the top of the sample, exposing the inner parts, which can be then analyzed by XPS.

Adapted from reference [134].

3.7 Scanning electron microscopy

Scanning electron microscopy (SEM) is a type of microscopy that uses electrons instead of light to image a sample. The use of electrons allows for resolutions better of a few nanometers, making this technique a very powerful tool for the analysis of micro- and nano-sized materials.

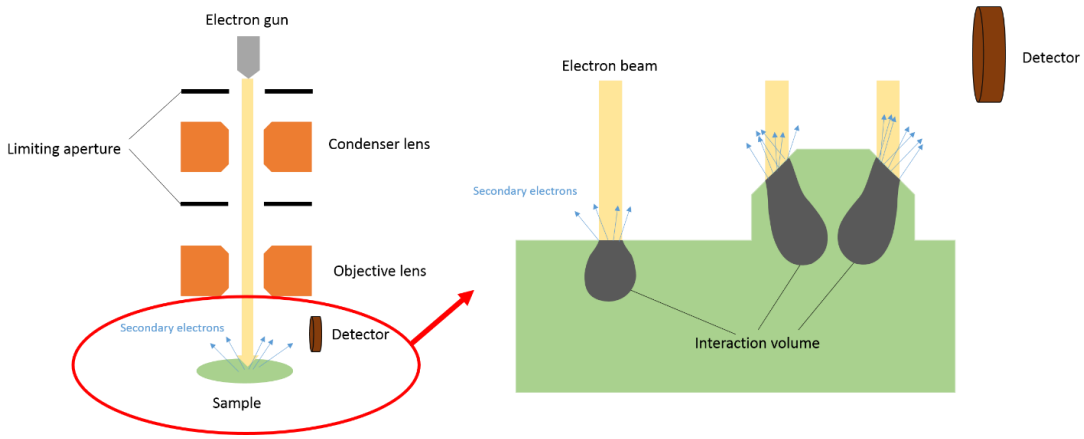

Figure 3.7.1. Left: simple schematics of a SEM showing the main components. Right: magnification of the sample, showing the interaction of the electron beam with different topologies within the sample.

Figure 3.7.1 shows the working principles of an SEM. Electrons are emitted from an electron gun (a filament, usually made of tungsten) which is heated up by passing a current through it, leading to the thermoionic emission of electrons. The beam of electrons is focused using electromagnetic condenser lenses and apertures, and is finally focused on the sample using the objective lens. Unlike light microscopy, the objective lens in SEM is used to focus the incoming beam, instead of gathering the light that was transmitted through the sample to the detector. The objective also allows for the exciting beam to be scanned over the sample, focusing it on different parts to form a complete

image. When the electrons hit the sample, they interact with its atoms in different ways, which can be used to analyze the sample.

The most common mode used for SEM imaging is to detect secondary electrons. These are electrons directly ejected when the atom is hit by an incoming electron from the beam, and often possesses a relatively low energy. These interactions occur mostly at just a few nanometers below the surface, in the so called interaction volume, the volume of the sample that is affected by the beam. Those electrons are then directed towards a detector which is kept at positive voltage in comparison to the sample, attracting some of the emitted electrons. Areas which emit more electrons are shown brighter than areas which emit less, such that the different topographies can be distinguished in the final image. This is because these different topographies interact differently with the beam and detector. Angled surfaces allow for the beam to penetrate the sample further, generating a larger interaction volume than on a flat surface. Surfaces angled towards the detector emit more electrons that are detected, since those electrons come out of the sample going in the detector's direction. On the other hand, surfaces angled away from the detector emit less electrons which are detected. This means that surfaces angled in the detector's direction appear brighter than flat surfaces, which in turn are brighter than surfaces facing the other direction. This allows for the differences in topology to be measured as differences in brightness. Finally, the size of the interaction volume, and hence the amount of ejected electrons, depends also on the energy of the incident beam, and with the composition of the sample. If a higher accelerating voltage is used to direct the electrons to the sample, the higher energy they acquire also means they can penetrate deeper in the sample, generating brighter images. On the other hand, samples with higher mean atomic numbers interact more strongly with the incoming electrons, decreasing the interaction volume, leading to a lower

brightness. Also, this means that differences in composition can be qualitatively determined by SEM.

Adapted from reference 135.

3.8 Powder x-ray diffraction

Powder x-ray diffraction (XRD) is a technique useful for determining the crystal structure of solids. This analysis can yield useful information to identify a compound, by comparing an unknown sample to known standards, or to measure changes in the structure of a known sample due to new synthetic methods, a certain chemical treatment, or even due to electrochemical processes.

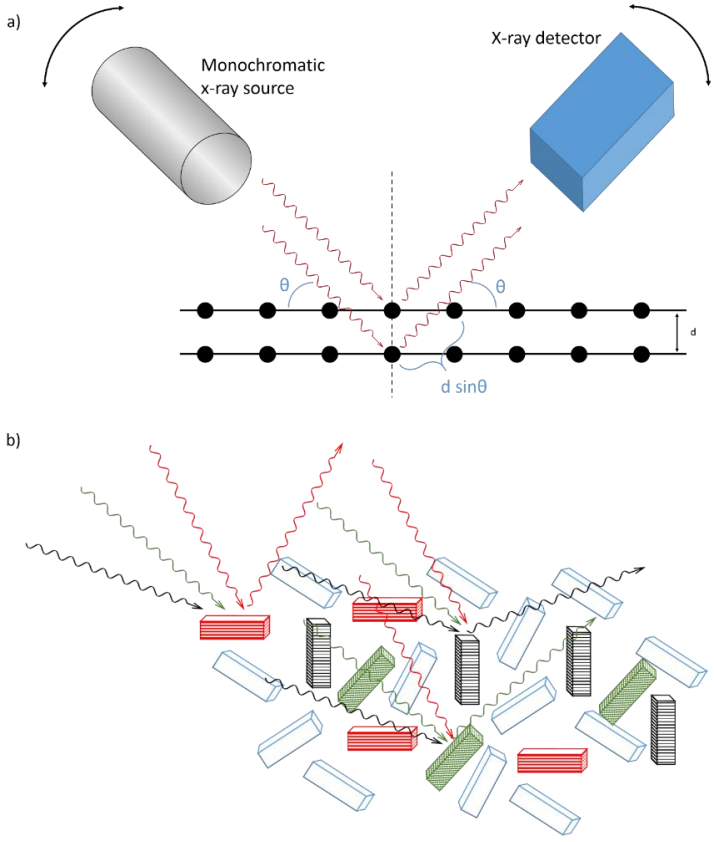

Figure 3.8.1. Left: simple schematics of an XRD device and Bragg's Law. The x-ray source and the detector are symmetrically rotated to change the degree θ. The black dots represent atoms in a crystalline plane, with two planes at a distance d apart. Right: representation of a sample with isotropically distributed grains having three different crystalline planes. Depending on the orientation of the grain, it diffracts radiation of a specific angle (black, green, or red). The blue crystals do not diffract the incident radiation at any angle.

Figure 3.8.1 shows the fundamentals of diffraction. It uses electromagnetic radiation of wavelength in the same order of magnitude as the interatomic distances in the crystal lattice, such as x-rays. The X-rays are absorbed by the atoms in the sample and re-emitted through Rayleigh scattering (Figure 3.5.2). The scattered radiation travels in all directions. Since there are multiple crystalline planes, the radiation scattered by each plane will interact with that of the other planes. At some particular angles, however, the scattering is said to be under Bragg's condition, i.e., they follow Bragg's law:

$$n\,\lambda = 2\,d\,\sin\theta \qquad \textbf{[3.8.1]}$$

Where n is an integer, λ is the wavelength of the incident radiation and d is the interatomic distance, both in nm, and θ is the incident angle. At a given angle θ, the scattered radiation has to travel an increased distance 2 d sinθ in comparison to radiation scattered at a plane above it. If this distance happens to contain an integer number of wavelengths, the two waves interact constructively once they meet again, and the signal is strengthened, making it possible to detect the diffracted radiation. For all other angles, however, this extra distance will not be an integer multiple of the wavelength. In those cases the interaction is destructive, i.e., the electromagnetic waves cancel each other out, and no radiation can be detected.

In normal crystallography, a single large crystal would be used, which can be rotated to expose different planes to the X-rays. Powder XRD assumes that the sample contains multiple micro- or nano-sized crystals. The samples are big enough that crystals in all possible orientations are assumed to be present. Since the x-ray source produces only x-rays with a single specific wavelength, the source and the detector are instead rotated. This rotation makes it so that the incident angle changes at each step. If a crystal in the sample has the right orientation such that one of its crystalline planes will be under the Bragg's condition at the incidence angle, it will diffract the X-ray (Figure 3.8.1,

right), and a peak in the diffractogram will be observed for that θ (or, most commonly, 2θ) value. As the incidence angle is changed, other crystals in the sample will diffract, corresponding to different crystalline planes, such that all planes for that solid can be identified.

Adapted from reference 136.

3.9 Elemental determination – combustion analysis and atomic emission.

In order to determine the elemental composition, both qualitatively and quantitatively, the most useful techniques are combustion analysis and atomic emission spectroscopy.

Combustion analysis is a straightforward process, in which the sample is heated to elevated temperatures under a stream of oxygen, i.e., oxygen in great excess. The high temperatures and oxygen content lead to oxidation of the sample, generating gaseous products such as CO_2, H_2O, N_2, and SO_2, according to:

$$C_xH_yN_wS_z + O_2 \rightarrow x\,CO_2 + y\,H_2O + w\,N_2 + z\,SO_2 \qquad \textbf{[3.9.1]}$$

The generated gases are then analyzed, for example, by gas chromatography, and the amount of each element quantified.

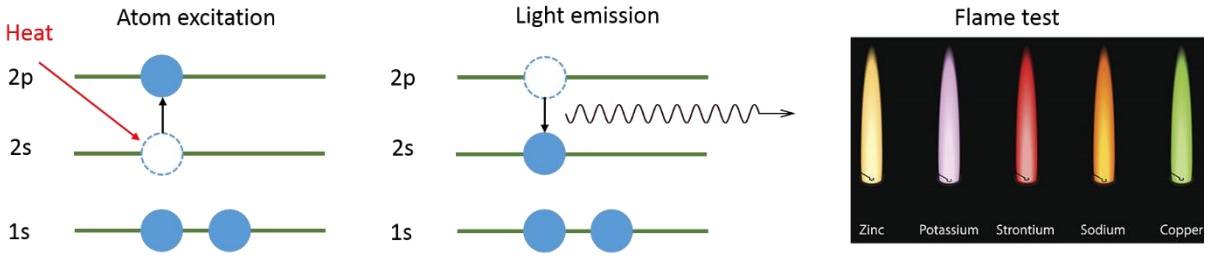

Figure 3.9.1. Scheme of thermic excitation of a lithium atom (left), light emission (center), and a flame test of different elements (right). Blue circles represent electrons in different electronic levels.

For other elements, atomic emission spectroscopy is more suitable. Here the sample is heated to high temperatures using, for example, a gas burner's flame, similar to the so called flame test. The atoms in the sample get excited by the high temperatures, and eventually emit the extra energy in the form of a light wave in order to return to the

ground state (Figure 3.9.1). Since the emissions are quantized, each element can be individually recognized by its individual emission spectrum, which can be analyzed, for example, using a coupled optical spectroscope.

Adapted from references 137 and 138.

4 Results and discussion

Herein, the experimental work carried out for this thesis is explained and discussed in depth. In each subsection, the procedures used to obtain the data are detailed first, followed by an analysis of said data by a combination of the methods described in section 3.

4.1 Effect of dissolved air in the electrolyte

State-of-the-art LSBs' electrolytes are constituted by ether solvents, or a mixture thereof[87], a lithium salt, and, optionally, an additive[101–103]. The choice of ethers as solvent comes from their stability towards polysulfides. The superior chemical stability of ethers was also shown to be relevant for Li-O_2 batteries, for instance[139]. Taking this in consideration, the electrochemistry of Li-S cells in a dry air environment is herein assessed.

4.1.1 Experimental procedures

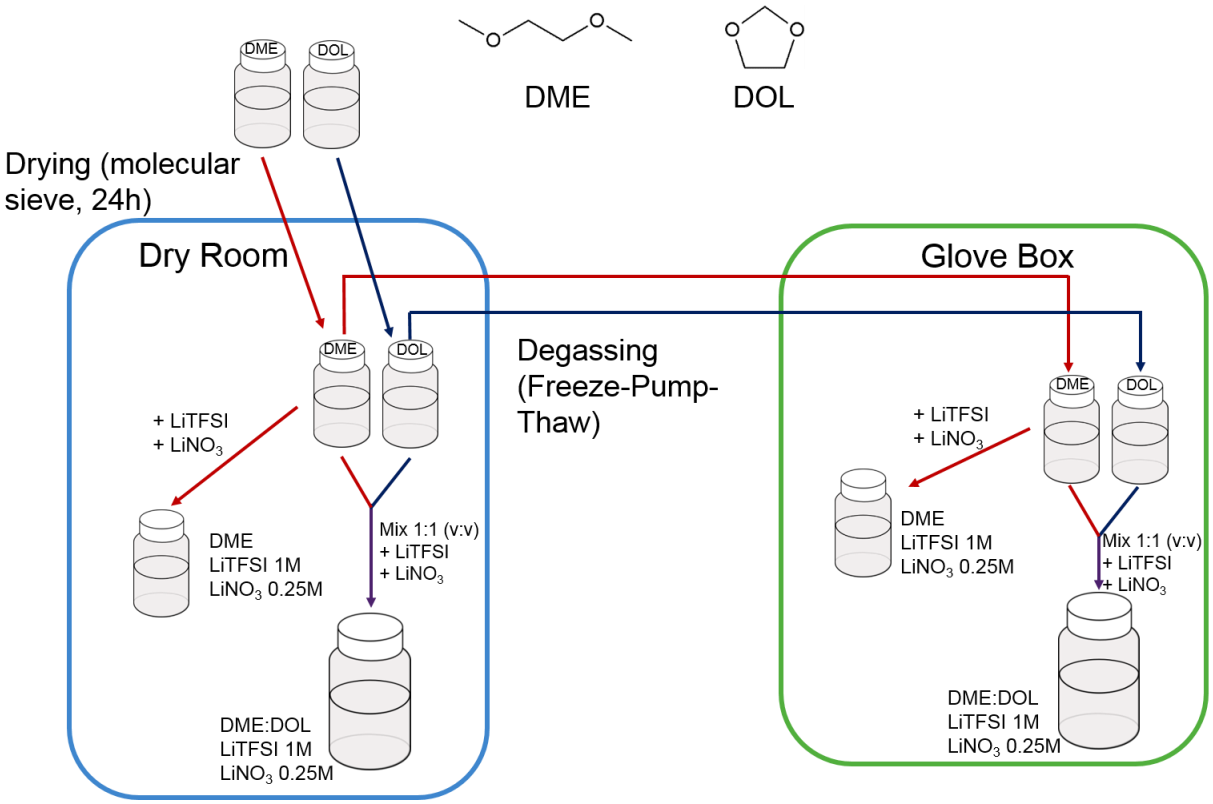

Figure 4.1.1. Scheme of electrolyte preparation, as well as structural formula of DME and DOL. For explanation of the each step, refer to the text.

Two sets of electrolytes were prepared and tested, one under dry air and one under argon (Figure 4.1.1). Electrolytes were prepared using dimethoxyethane (DME, Solvionic) and 1,3-dioxolane (DOL, Solvionic) as solvents. Each solvent was dried with 20 wt.% molecular sieve (3Å, Alfa-Aesar) for 24h, after which the water content was below 20 ppm, as determined by coulometric Karl Fischer titration (Mettler-Toledo Titrator Compact C30). For the DME:DOL-based electrolyte stored in dry air, the dried solvents were mixed in a 1:1 volumetric ratio, and the appropriate amount of lithium bis(trifluoromethane)sulfonimide (LiTFSI, Solvionic) and lithium nitrate ($LiNO_3$, Alfa Aesar) were added, in order to achieve a concentration of 1 mol L^{-1} and 0.25 mol L^{-1}, respectively. Dry DME was also used as the only solvent for another electrolyte, with the same concentrations of LiTFSI and $LiNO_3$. The electrolytes prepared and stored under

dry air are hereinafter labeled as DME:DOL air and DME air for DME:DOL (1:1 v/v) and DME as solvents, respectively.

For electrolytes without air, the dried solvents were further degassed, each individually, via the Freeze-Pump-Thaw method. Briefly, each solvent was frozen in liquid nitrogen, followed by vacuum until a final pressure of less than 10^{-3} mbar was achieved. The flask containing the solvent was then disconnected from the vacuum pump and allowed to melt under static vacuum. This step was repeated three times for each solvent. Afterwards, the solvents were transferred and stored in an Ar-filled Glove Box (MBraun) with O_2 and H_2O content lower than 0.1 ppm. These degassed solvents were then stored under argon atmosphere. Dried and degassed DME and DOL were mixed in a 1:1 volumetric ratio, and then used to prepare a 1 mol L^{-1} LiTFSI and 0.25 mol L^{-1} $LiNO_3$ in DME:DOL (1:1 v/v) electrolyte under Ar. Dried and degassed DME was also used to prepare a 1 mol L^{-1} LiTFSI and 0.25 mol L^{-1} $LiNO_3$ in DME electrolyte under Ar. Electrolytes prepared and stored under Ar were labeled DME:DOL Ar and DME Ar for DME:DOL (1:1 v/v) and DME as solvents, respectively.

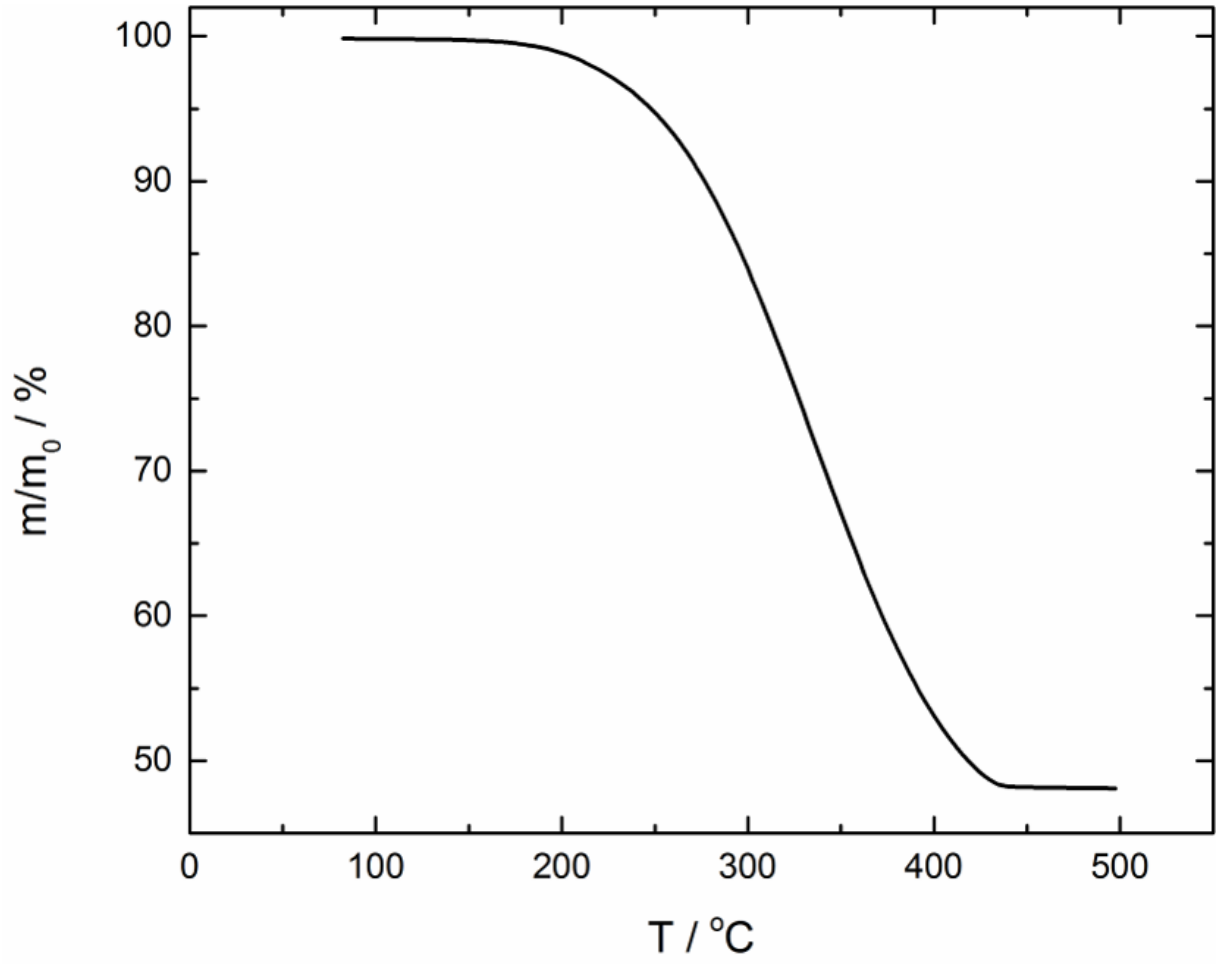

Figure 4.1.2. TGA of AC/S sulfur-based material (N_2 atmosphere, 10 °C min^{-1} heating rate). Sulfur content was determined to be 52% (m/m).

Sulfur composite cathodes (AC/S) were prepared by impregnation of sulfur in an activated carbon matrix. Specifically, 1 g of sulfur (Sigma-Aldrich) was dissolved in 65 mL of cyclohexane (Sigma Aldrich) at 70 °C. 0.2 g of activated carbon (DLC Super30, Norit) were then added, and the mixture was sonicated for 40 minutes and further stirred for one hour at 60 °C, and for 24h at 30°C. The solid material was then filtered and dried at 50°C under vacuum to remove the solvent. The sulfur content was determined to be 52 % wt. (Figure 4.1.2) by thermogravimetric analysis (TGA, Netsch), at a heating rate of 10 °C min^{-1} in N_2 atmosphere, from 80 to 500 °C. The weight percent of sulfur was calculated as the difference between the initial and the final mass for the composite, i.e., assuming that only but all sulfur is sublimated by heating.

The AC/S composite was then mixed with polyvinylidene fluoride (PVdF 6020, Solvay) and SuperC65 (Imerys Graphite & Carbon), as binder and conductive carbon respectively, in the ratio of 85:5:10. N-Methyl-2-pyrrolidone (NMP, Sigma Aldrich) was used as solvent to prepare the slurry. Electrode were cast, using the Doctor blade method, onto aluminum foil. The electrode layer was firstly dried at 60°C under normal atmosphere to remove the solvent and then punched into 12 mm diameter discs. Finally, the electrode disks were further dried overnight at 50°C in vacuum to remove solvent and water traces before each electrochemical characterization. The final active mass loading of the electrodes was ~1 $mg_s\ cm^{-2}$.

Three electrodes *Swagelok-type* T-cells were assembled inside an Ar-filled glove box (O_2 and H_2O <0.1 ppm), using AC/S cathodes and lithium metal (Rockwood Lithium) as counter and reference electrodes. Glass fiber (Whatman GF/A) was used as separator, soaked with ~100 μL of electrolyte. To prevent short-circuits, four layers of separator were used between counter and working electrode. The reference electrode consisted of a thin strip of lithium attached to a Ni grid, with 2 mm length, inserted between the separator layers.

Cells with electrolytes under Ar were assembled inside the Glove Box. The air containing electrolytes were sealed inside a bubble-free blister, and brought inside the glove box. Once inside, the blister was punctured using a syringe needle, and quickly added to the separator, and the cell sealed, to avoid gas exchange with the argon environment.

All galvanostatic measurements were performed at a constant rate of C/10 (1C = 1675 mA g_s^{-1}) between 3.0 and 1.5 V vs. Li/Li^+ using a Modulab XM ECS (Solartron Analytical). After each cycle, the cells were held at 3.0 V for 20 minutes (after which the current typically dropped below C/30) and analyzed by electrochemical impedance spectroscopy (EIS), from 250 kHz to 10 mHz, with a signal amplitude of 5 mV. All tests

were performed in a climatic chamber at 20 °C (Binder). Each cell was run for a total of 10 discharge/charge cycles and, finally stopped in the charged state (3.0 V *vs.* Li/Li^+) for the *post mortem* analysis.

After cycling, all cells were disassembled in inert atmosphere. The sulfur cathodes were carefully washed with DME to remove any salt residue, and stored under Ar. To recover the electrolyte, the separators were placed inside a sealed vial and centrifuged at 6000 rpm for 60 min.

The cathodes were subjected to scanning electron microscopy (SEM, Zeiss LEO 1550VP), with an acceleration voltage of 3 kV. To avoid any contamination by air, all samples were transferred inside the SEM chamber using a homemade sealed sample carrier filled with Ar.

The cathodes were also analyzed by X-ray photoelectron spectroscopy (XPS, PHI 5800 MultiTechnique ESCA System, Physical Electronics), using a monochromatic Al-Kα (1486.6 eV) radiation. The measurements were performed with a detection angle of 45°, using pass energies at the analyzer of 93.9 and 29.35 eV for survey and detail spectra, respectively. The samples were transferred to the device using a sealed sample holder to avoid air contamination. All XPS spectra were calibrated to the signal of the C(1s) peak at 284.6 eV and processed using CasaXPS software. When analyzing sulfur spectra, the $S(2p_{1/2})$ peaks were constrained to be shifted +1.16 eV to the corresponding $S(2p_{3/2})$ peaks, while having 0.511 times their area, and the same full width at half maximum (FWHM).

Both the fresh electrolytes and the ones recovered from cycled cells were analyzed by infrared spectroscopy (IR, PerkinElmer) in the attenuated total reflectance (ATR) mode. All ATR-FTIR measurements were performed in dry argon atmosphere.

4.1.2 Electrochemistry of sulfur in different electrolytes

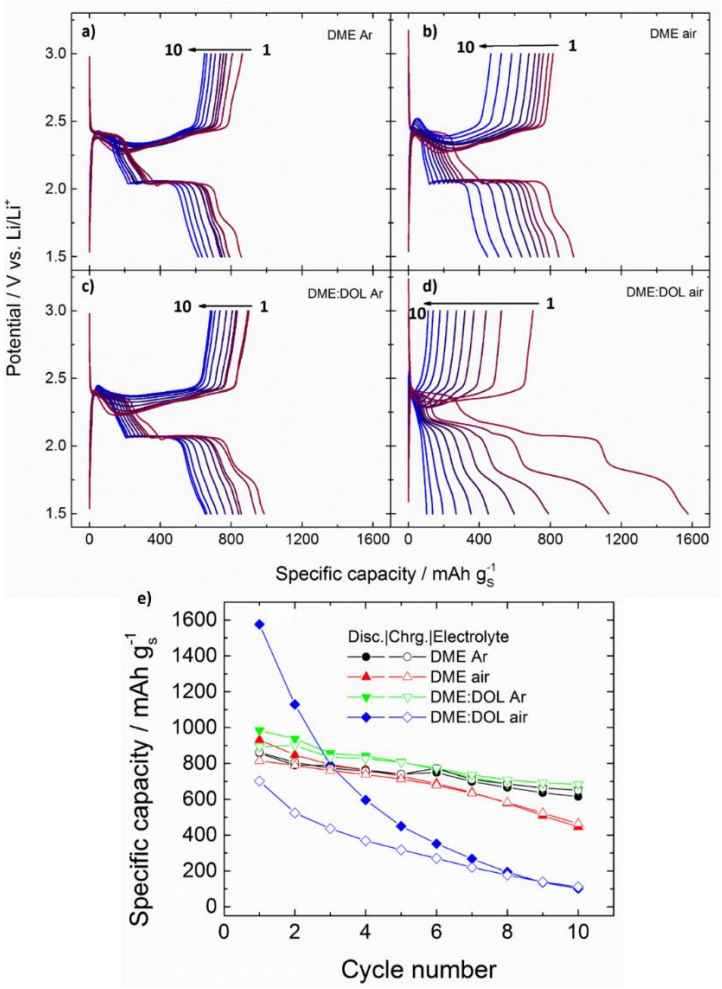

Figure 4.1.3. Voltage profiles of Li-S cells with different electrolytes: (a) DME Ar, (b) DME air, (c) DME:DOL Ar, and (d) DME:DOL air. (e) Capacity retention upon 10 cycles of the Li-S cells employing different electrolytes.

Figure 4.1.3a-d show the voltage profiles upon discharge and charge of Li-S cells with different electrolytes while Figure 4.1.3e shows the total capacity retention over 10 cycles. It is clearly noticeable that the cells employing DME Ar and DME:DOL Ar (Figure 4.1.3a and c) have very similar voltage profiles, in agreement with the typical cycling behavior of sulfur cathodes[49]. The discharge profile consists of a plateau at ~2.4 V, a sloping region from ~2.3 to 2.1 V, and another, longer, plateau at ~2.1 V. The high voltage plateau at 2.4 V is due to the reduction of S_8 to high order polysulfides ($Li_2S_{6\text{-}8}$). In the sloping region, these are reduced to form shorter polysulfides (Li_2S_4), which are further

reduced at ~2.1 V to solid Li_2S_2 and Li_2S, the final discharge products. It is important to note, however, that many disproportionation reactions take place in such a system, and the exact nature of the formed species upon reduction is still not fully known[47,49]. The abovementioned species represent what the average chain length is expected to be in each case. Finally, the last plateau at ~1.7 V is associated to the irreversible reduction of $LiNO_3$ on the positive electrode[107], which eventually vanishes due its complete consumption upon cycling.

Interestingly, the presence of air in the electrolyte appears not to be relevant for electrolytes based on DME as single solvent, as testified by the similar voltage profiles of the cells employing DME Ar and DME air (figure 1a and 1b, respectively). A first feature to be noticed is the lack of any sign of oxygen reduction in the DME air electrolyte. Oxygen reduction should be expected at about 2.6-2.7 V vs. Li/Li^+ [140,141], while in Figure 4.1.3b, no plateau at this potential can be detected. This is, however, not surprising, since most of the O_2 is likely reacting with the lithium anode, as soon as the cell is assembled. The only indication of O_2 presence is the slightly higher open circuit potential (OCP) before the experiment started (~3.3 vs. 2.8 V in the presence and absence of air, respectively), possibly due to the reaction of sulfur with oxygen, forming lower sulfur oxides. Such oxides might explain the higher OCP observed in this case.

A further substantial difference between DME Ar and DME air is the more pronounced capacity fading of the latter (see Figure 4.1.3e). A possible explanation would be the oxidative decomposition of DME, which can form, among other, inorganic carbonates and esters[142]. Sulfides and polysulfides are known for their high nucleophilicity, in part due to the large atomic volume of sulfur, making them readily polarizable. Organic thiolates, which have a negatively charged sulfur atom analogous to sulfides and polysulfides, have been shown to be highly reactive towards organic esters[143], resulting in their cleavage. Therefore it is not unlikely that polysulfides formed

during discharge of sulfur cathodes can also react with organic carbonates *via* nucleophilic attack[92], forming poly-thiocarboxylates. Hence, the carbonates and esters formed by oxidation of DME in presence of air are expected to react with dissolved polysulfides formed during discharge, decreasing the available amount of active material, and leading, in turn, to a more pronounced capacity fade in each cycle, when compared to the air-free DME electrolyte.

Similarly, DME:DOL air also has a different behavior compared to the electrolyte under Ar. The first cycle capacity is much larger (ca. 1600 mAh g_s^{-1}) than for those electrolytes. This is mainly due to the increased discharge capacity in the sloping region, but can also be partially attributed to the increased capacity coming from nitrate reduction, accounting for about 300 mAh g_s^{-1} more than in the other electrolytes. This higher discharge capacity is likely associated to larger availability of nitrate in the electrolyte. As it will be shown later, indeed, the passivation of the lithium anode by the decomposition products of DOL results in a lower consumption of nitrate at the anode, making it available to react on the positive electrode. Once again, no features attributable to oxygen reduction could be observed besides the higher initial OCP value. The efficiency of the cell also decreases substantially, with approximately half the capacity being lost in the first charge. After 10 cycles, the capacity of the cell employing DME:DOL air is only 110 mAh g_s^{-1} while the typical plateaus of sulfur practically vanished.

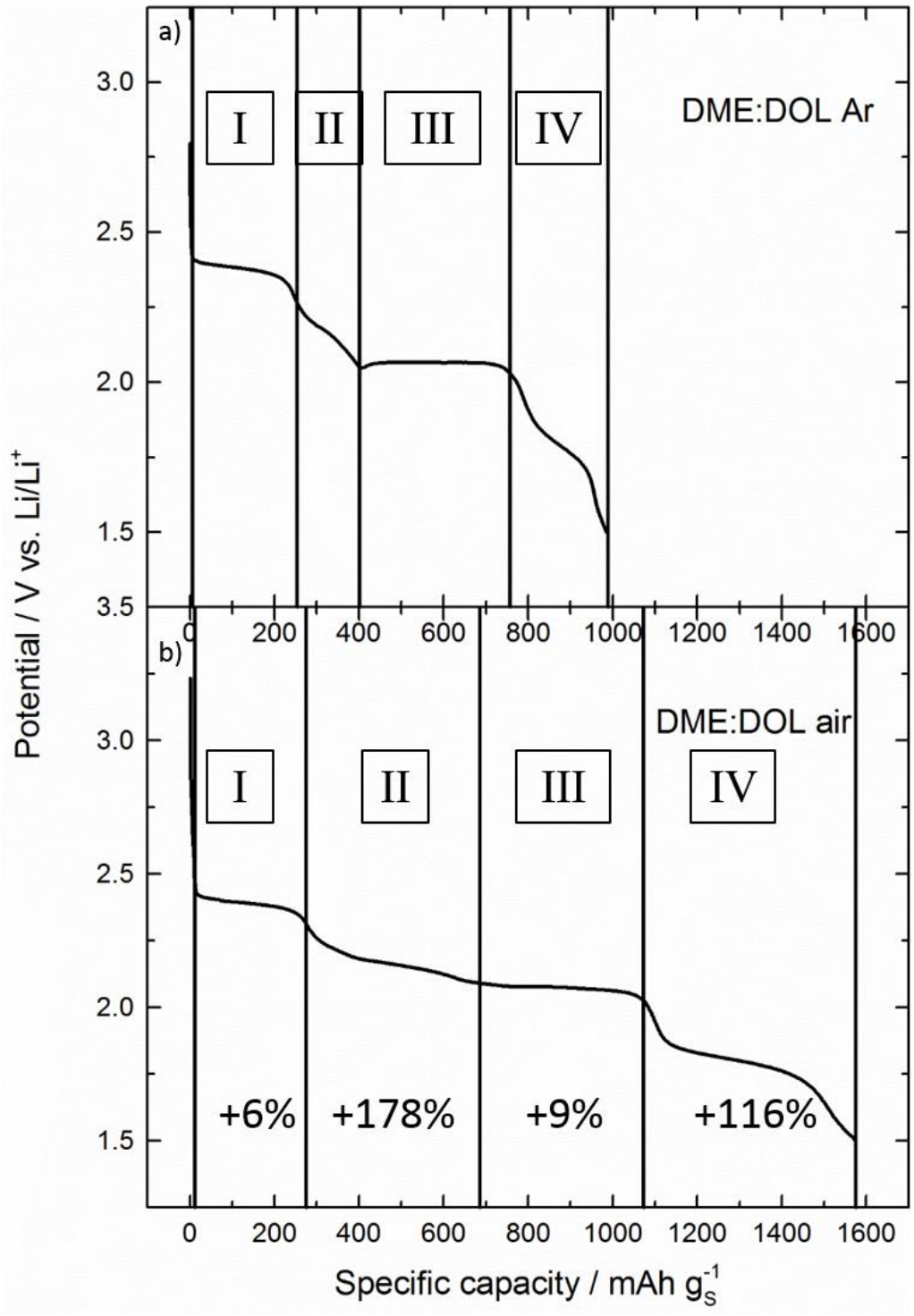

Figure 4.1.4. First discharge profile of Li-S cells in a) DME:DOL Ar electrolyte, and b) DME:DOL air electrolyte. The cycles are divided in four regions, corresponding to (I) high voltage plateau, (II) sloping region, (III) low voltage plateau, and (IV) nitrate reduction over the cathode. The percentage values in figure b) shows the increase in capacity of a given region when compared to the same region in figure a).

Figure 4.1.4 summarizes the differences, in the first discharge of DME:DOL Ar and DME:DOL air. As it can be seen, there is only a small change in regions I and III, where S_8 is reduced to long-chain polysulfides, and the solid discharge products are formed, respectively. There is, however, a substantial difference in region II, when long-chain polysulfides are reduced to shorter polysulfides, and in region IV, where nitrate is irreversibly reduced on the cathode. As mentioned previously, this is a clear indication that there is more nitrate available in the electrolyte of DME:DOL air in comparison to DME:DOL Ar, and is attributed to the formation of a different passivation layer over the lithium anode. The change in region II, however, is still the most interesting feature, since it shows a change in reduction mechanism for sulfur.

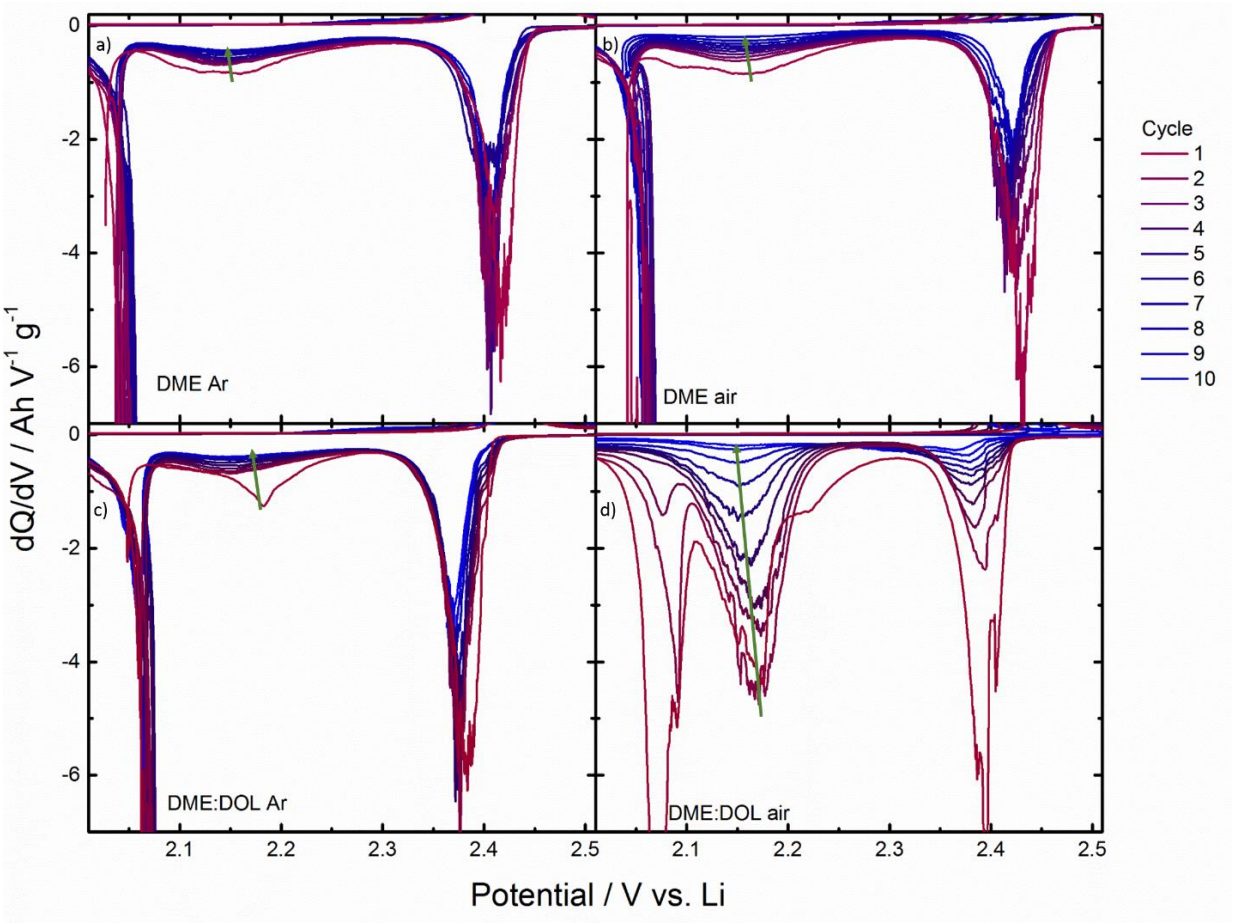

Figure 4.1.5. Differential capacity plots of the discharge curves (reported in Figure 1a-d) of cells with a) DME Ar, b) DME air, c) DME:DOL Ar, and d) DME:DOL air electrolytes. The plots are focused in the region of major interest, i.e. between 2.0 and 2.5 V.

The differences in region II of Figure 4.1.4 can be observed more in depth by looking at the differential capacity plots of the discharge curves (Figure 4.1.5). Once again, the difference between DME Ar and DME air (Figure 4.1.5a and b, respectively) is virtually none, indicating that this electrolyte is much more resistant to decomposition of air, and there is no change in the mechanism of sulfur reduction. For DME:DOL Ar and DME:DOL air (Figure 4.1.5c and d, respectively), there are noticeable changes. For DME:DOL Ar, in fact, only the first cycle shows an increase of the peak around 2.15 V vs. Li/Li^+ in Figure 4.1.5c, while DME:DOL air shows higher intensities for this peak, which is equivalent to region II in Figure 4.1.4, in all cycles. There is a pronounced change in shape of the peak around 2.07 V vs. Li/Li^+, corresponding to the formation of

the solid discharge products. Similar results to Figure 4.1.4 and Figure 4.1.5c and d for an increased capacity in region II were shown in literature for solvents with a large concentration of the trisulfur radical anion[48], indicating that DME:DOL air might have a higher formation of the trisulfur radical.

4.1.3 Reactions of the electrolyte – EIS studies

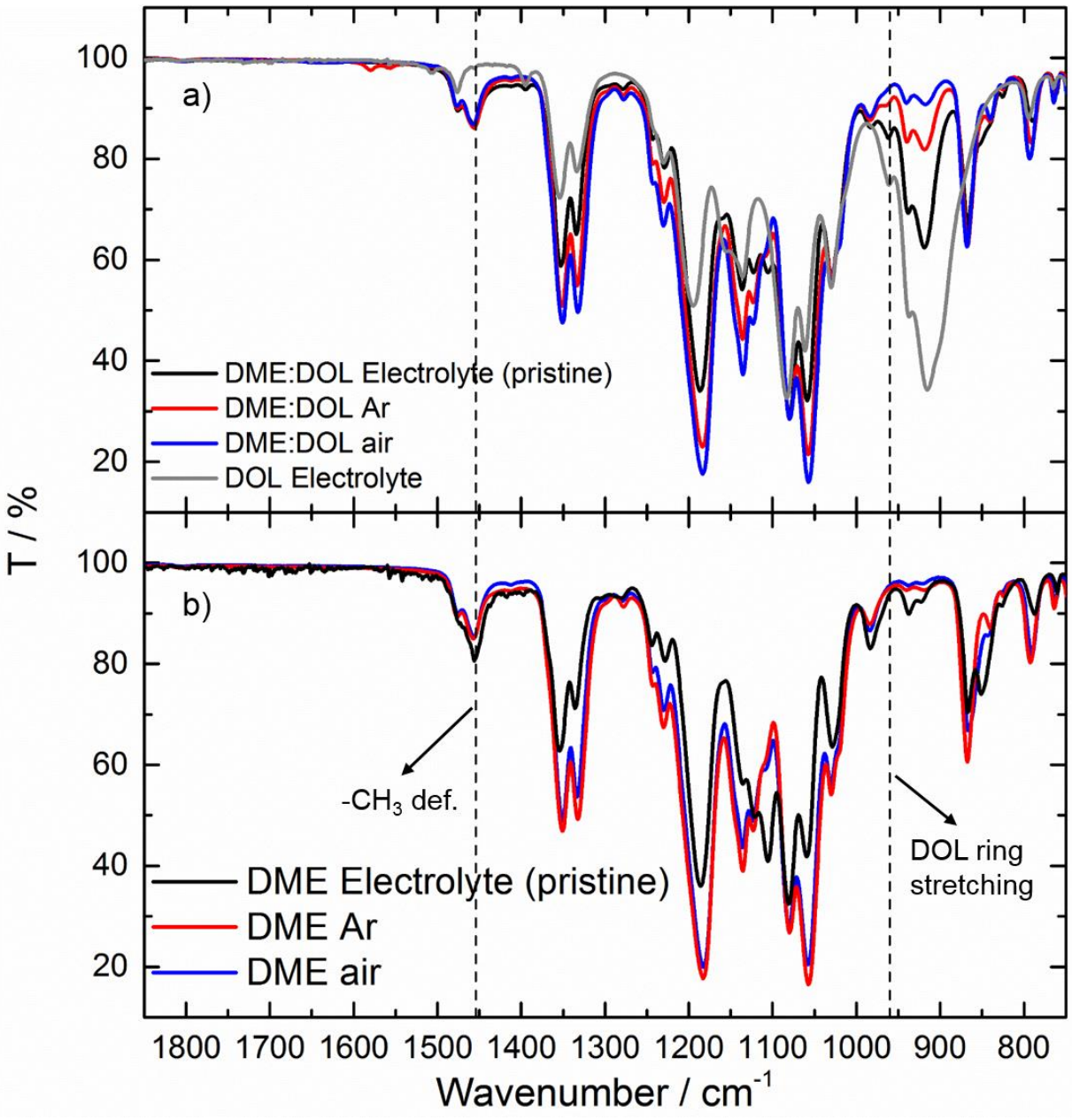

Figure 4.1.6. ATR-FTIR spectra of the different electrolytes: a) DME:DOL Ar (pristine electrolyte, black), compared to DME:DOL Ar after 10 cycles (red), DME:DOL air after 10 cycles (blue), and a solution of 1 mol L^{-1} LiTFSI and 0.25 mol L^{-1} $LiNO_3$ in DOL (DOL Electrolyte, grey); b) DME Ar (pristine electrolyte, black), compared to DME Ar after 10 cycles (red), and DME air after 10 cycles (blue).

As displayed in Figure 4.1.6, the pristine and cycled electrolytes were analyzed by ATR-FTIR. The dashed vertical lines mark two regions of interest for these electrolytes being solely associated to either DME or DOL. The bands around 1454 cm^{-1}

are due to the asymmetric methyl group (-CH_3) deformation in DME[144], as confirmed by their absence in the spectrum of pure DOL (labeled as 'DOL electrolyte' in Figure 4.1.6a). The band around 960 cm^{-1} is instead due to the ring stretching of DOL[145], and is absent in the DME-based electrolyte.

From Figure 4.1.6, it is clear that DOL is consumed during cycling. The decrease of the DOL band is stronger when oxygen is present, but it is also appreciated in the DME:DOL Ar cycled electrolyte, too. Differently, the DME band is not strongly affected in any case. These findings are in agreement with what was previously observed in Figure 4.1.3. Namely, oxygen has a stronger impact on DOL. The oxygen solubility in DME:DOL is similar to that in DME[146], thus, a higher dissolved O_2 amount is not the reason for the increased decomposition. Thus, the decomposition mechanisms of DME and DOL must be different. As a matter of fact, it has been shown that DME reacts with oxygen superoxide to form esters, by bonding oxygen atoms to the carbon backbone of DME[142]. By this mechanism, oxygen is consumed upon oxidation of DME, i.e., the decomposition will stop after all O_2 has reacted. Differently, being a cyclic compound, DOL is unsaturated and subject to ring opening reactions (ROR). In literature, two kinds of RORs for DOL are reported: polymerization[147,148] and isomerization[149].

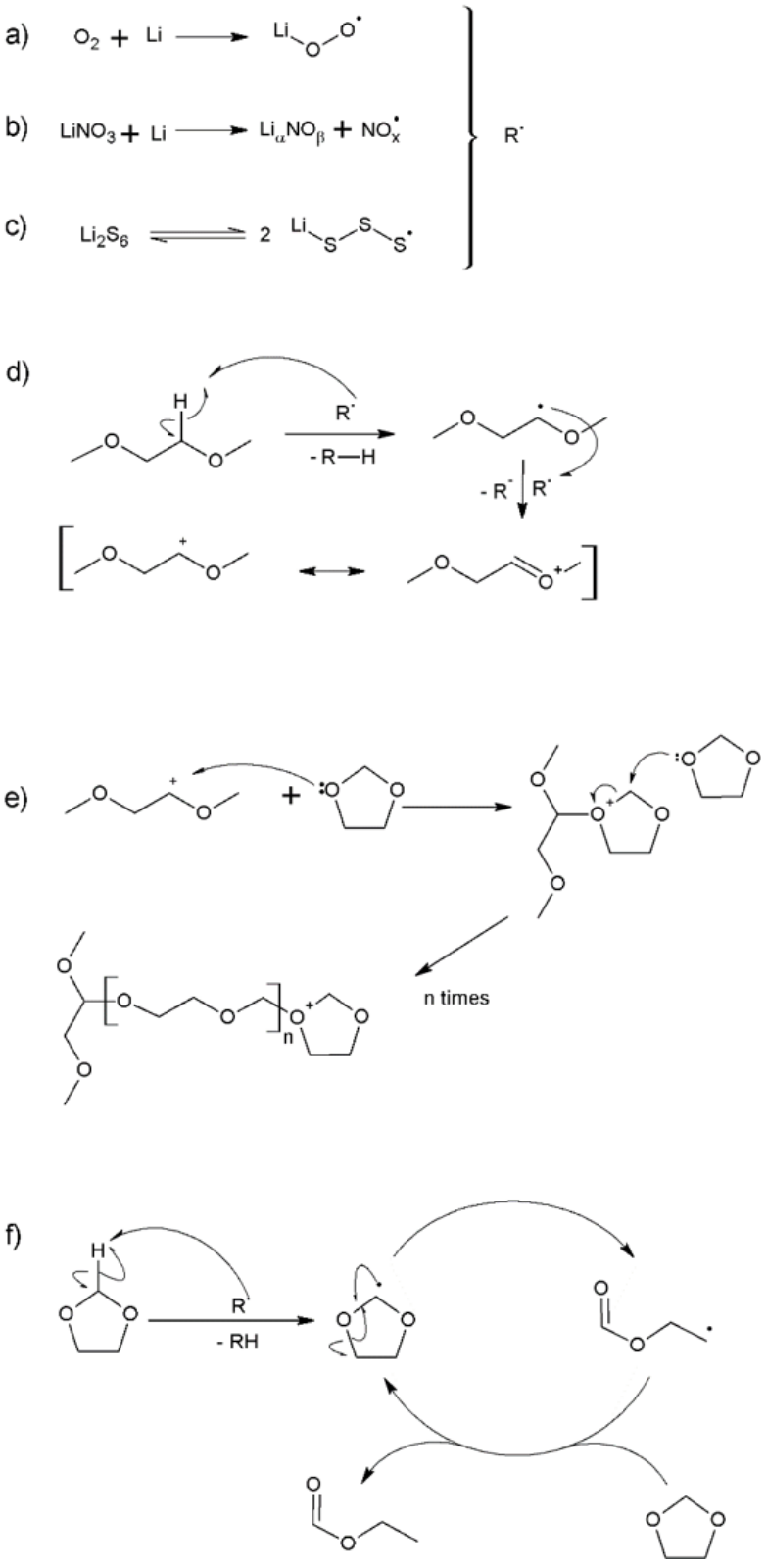

Figure 4.1.7. Proposed mechanisms of (a-c) radical formation in Li-S cells, (d-e) DOL polymerization, and (f) DOL isomerization.

Figure 4.1.7 depicts the proposed mechanisms for the DOL decomposition in Li-S cells. This mechanism, based upon reactions already known for DOL, goes through the formation of highly reactive radicals that can be expected in the cell during normal operation (Figure 4.1.7a-c). Of particular importance is the reduction of O_2, when present, in contact with metallic lithium, leading to the formation of lithium superoxide (Figure 4.1.7a). This species is known to be highly reactive, and, in fact, causes the increased DOL consumption when O_2 is present. From Figure 4.1.6, it is obvious that some DOL is consumed even in the absence of O_2, meaning that some other radical source must be inherently present in the cell, forming less reactive radicals, and/or radicals in a smaller amount. The electrolyte also contains $LiNO_3$ to aid the SEI formation on the lithium anode[101,105]. The mechanism of nitrate reduction in these electrolytes has not been fully elucidated yet, as studies on the subject often show only the decomposition products of $LiNO_3$ over the lithium surface[101]. However, there has been some studies on nitrate reduction in molten-salt electrolytes[150], where the reduction occurs through the formation of lower nitrogen oxides and alkali metal oxides. Since ether-based electrolytes are aprotic, it is expected that the reduction of $LiNO_3$ follows a mechanism close to that occurring in molten salts (Figure 4.1.7b). Lastly, the presence of $LiS_3^{\cdot}$ is inherent of Li-S cells[48,49] (Figure 4.1.7c). However, they are only present upon S_8 reduction, so they cannot account for all the results seen here.

The first mechanism for DOL decomposition is its polymerization, as shown in Figure 4.1.7d and e. It has been shown that DOL polymerization occurs neither through anionic[148] nor radical initiators[149], but only *via* cationic polymerization. Thus, we propose a mechanism where the radicals in solution react with DME to form a carbocation (Figure 4.1.7d), which then reacts with DOL to start the polymerization (Figure 4.1.7e)[151]. Additionally, there might be other Lewis acids in solution, which could help initiate the polymerization as well. Polymerization of DOL has been already shown in other

electrolytes, both those relevant to Li-O_2 batteries, i.e., where molecular oxygen is present and dissolved in the electrolyte,[142,152], as well as for LSB[105]. Aurbach and coworkers[152] showed, for instance, that a silver electrode swept from 3.0 to 1.7 V vs. Li/Li^+ in a 0.5 mol L^{-1} solution of $LiClO_4$ in DOL won't show any polymerization product over its surface. For the same system with added O_2, some polyether species are detected on the silver surface by FTIR, showing that the products of O_2 reduction can indeed promote DOL polymerization. However, the specific mechanism of polymerization in this setup was not determined. A similar phenomenon was reported by Bruce and coworkers[142] in 1 mol L^{-1} $LiPF_6$ in DOL under 1 atm O_2, although the excess of oxygen lead to further oxidation of polyether to form polyesters. In another work by Aurbach and coworkers[153], lithium metal was exposed to pure DOL and DOL-based electrolytes (without oxygen). FTIR and XPS measurements of the surface of lithium showed hints for DOL decomposition, among which some peaks related to C-O bonds that the authors attributed to both polyether and alkoxide species. This is agreement with our findings reported in Figure 4.1.6a, in which DOL is consumed even when the electrolyte has no oxygen dissolved. Overall, all these previous reports are also in accordance with Figure 4.1.7a and b, were we show that DOL decomposition starts on the anode side. Interestingly, this last work by Aurbach also showed the presence of formate on the surface of lithium, which confirms the reaction in Figure 4.1.7f, where we propose that the direct reaction of DOL with radical species is not the polymerization, but rather its isomerization to form ethyl formate[149]. This reaction is explained by the formation of a (strong) C=O bond, and takes place in parallel to the first one. The formation of a polymeric film over the anode has a potentially good impact on the cell cycle life, since it avoids the reaction of polysulfides with metallic lithium. In fact, this might be one of the reasons for the early reports on DOL-containing electrolytes offering better performance[87,97,154], as those did not use SEI forming additives (e.g., $LiNO_3$)[104].

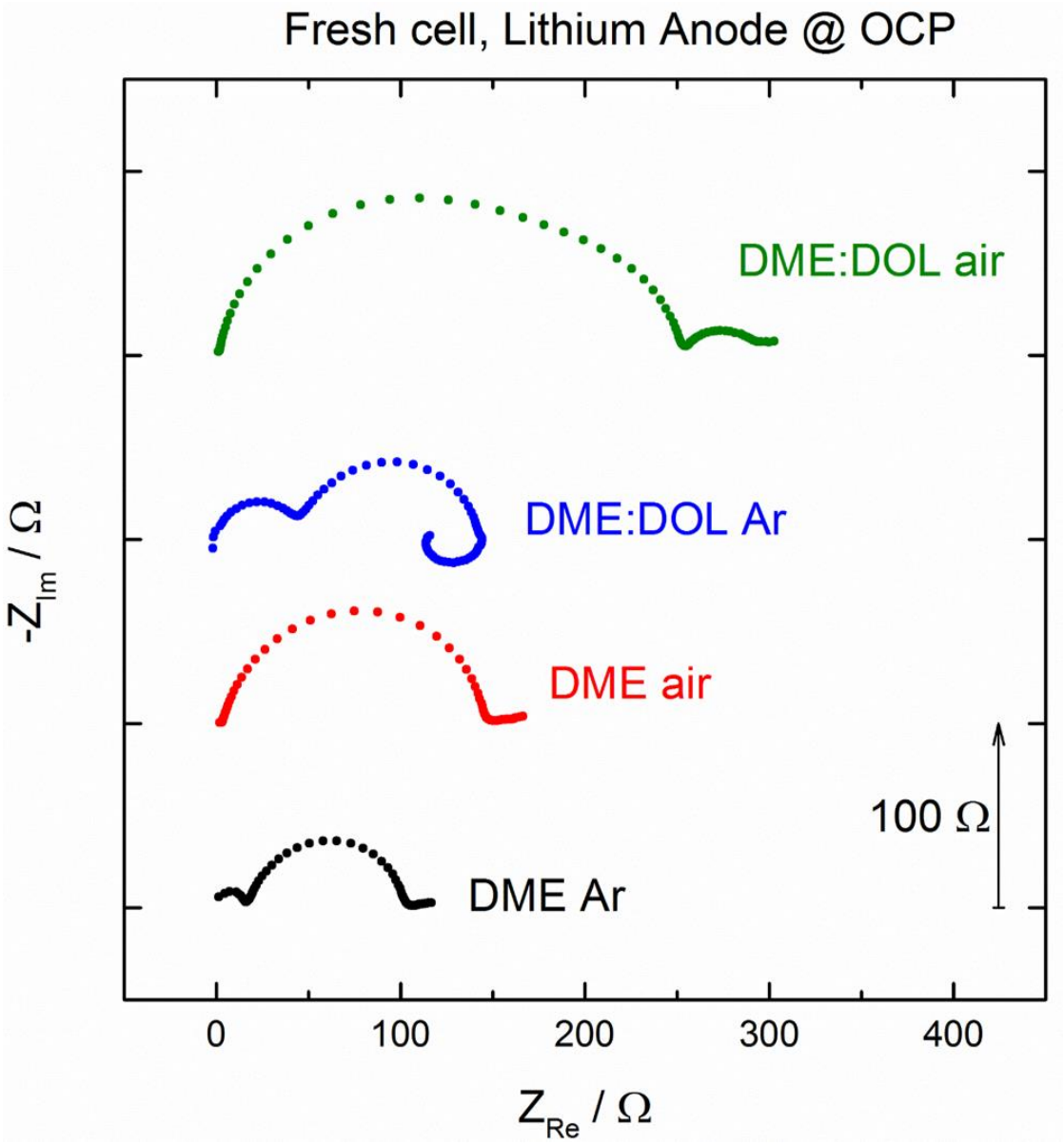

Figure 4.1.8. Impedance spectra of the lithium anode of cells with different electrolyte at OCP (before cycling started).

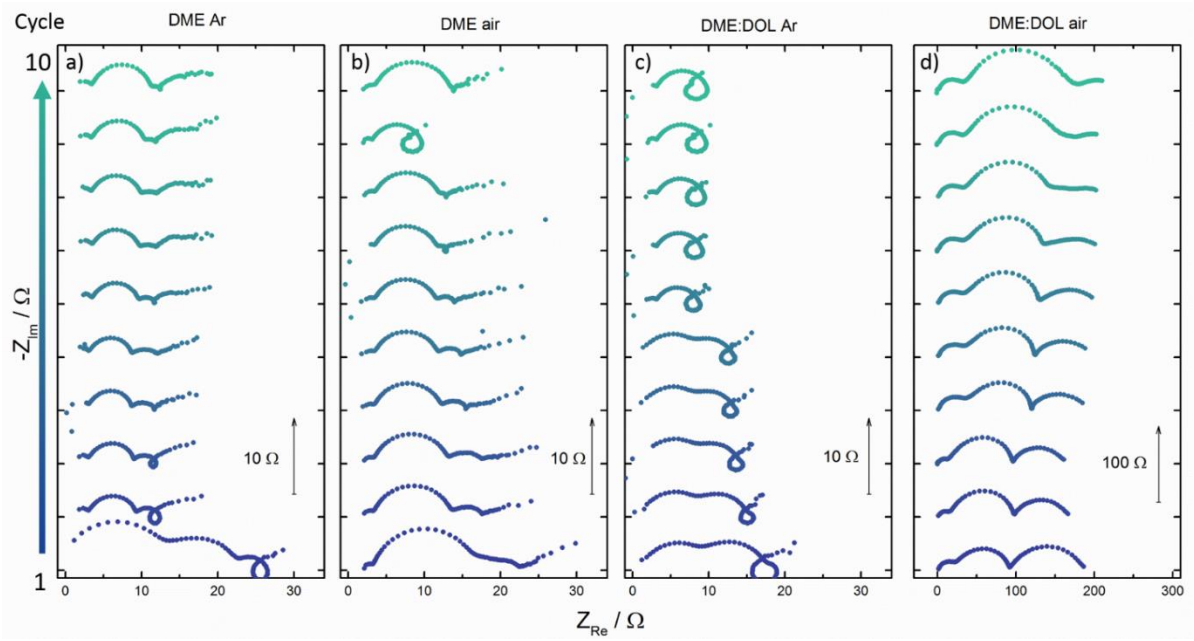

Figure 4.1.9. Impedance spectra of the lithium anode for cells with a) DME Ar, b) DME air, c) DME:DOL Ar, and d) DME:DOL air for the first 10 cycles.

Figure 4.1.8 and Figure 4.1.9 show the impedance of the lithium anode of the cells with different electrolytes. It is clear in Figure 4.1.8Figure 4.1.9. Impedance spectra of the lithium anode for cells with a) DME Ar, b) DME air, c) DME:DOL Ar, and d) DME:DOL air for the first 10 cycles. that, even before the cell starts to be cycled, the impedance of the anode for the cell with DME:DOL air is much bigger than that for the other cells. This is a clear evidence that the polymerization of DOL starts at the anode side, as proposed in Figure 4.1.7, and begins as soon as the electrolyte is brought in contact with the anode. This holds true as well for each of the subsequent 10 cycles (Figure 4.1.9). The much bigger impedance values for DME:DOL air are indicative of a much thicker SEI, caused by the extensive polymerization of DOL over the anode. This extensive polymerization also explains the decrease in DOL content, as observed in Figure 4.1.6. Also, the contribution of DOL to form the SEI means that less nitrate is consumed during SEI formation, explaining the higher nitrate reduction observed in Figure 4.1.4.

This increase in the anode impedance cannot, however, explain neither the strong decrease in capacity of DME:DOL air cell (Figure 4.1.3), nor the change in mechanism of this cell. As shown, the increase in impedance happens before the cell starts to be cycled, and the impedance remains relatively constant for the next 10 cycles. If the anode was the cause of the change in behavior, then a constantly lower capacity would be expected from the first cycle onwards. Instead, the change in behavior is due to the formate ester (Figure 4.1.7f) in the cell. As in the case of the polymerization, the radicals that initiate the formate formation are initially produced over the anode, but remain dissolved in the electrolyte after formation. The presence of ethyl formate can be, however, very detrimental to the cell cycling life, since polysulfides can react with esters[92,143], forming electrochemically inert products.

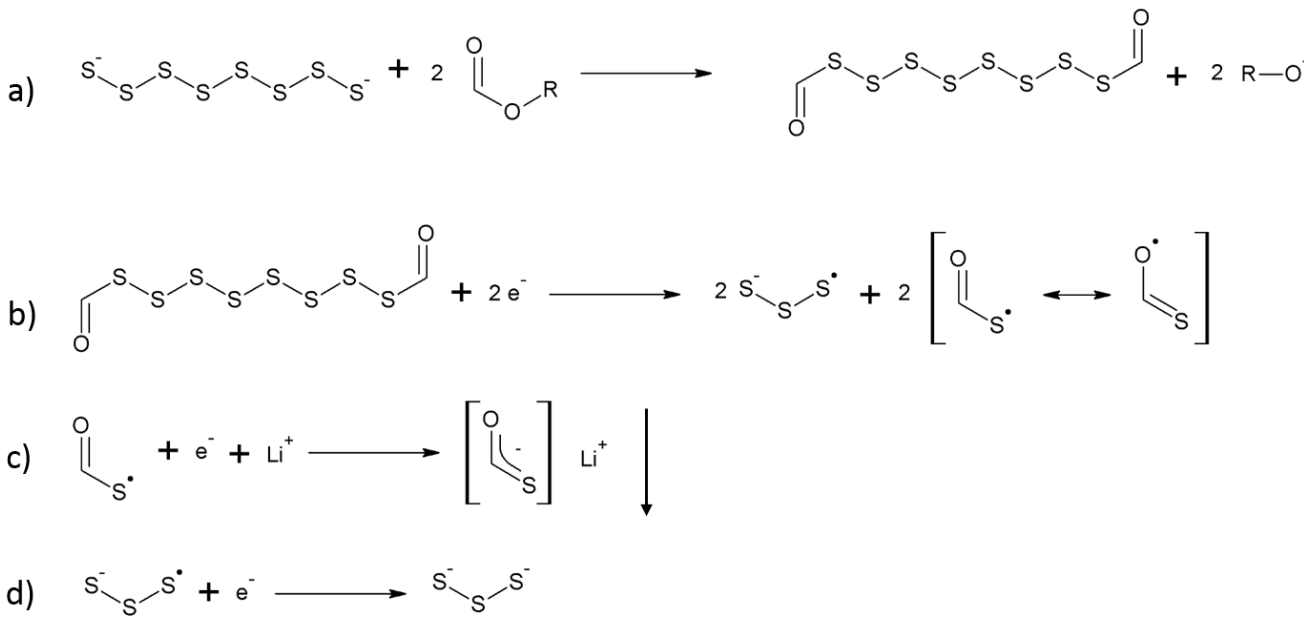

Figure 4.1.10. Proposed mechanism for the interaction of polysulfides with esters. a) Nucleophilic attack of polysulfide, forming poly- thiocarboxylates, b) reduction of poly-thiocarbonate to form thiocarboxylates radical and trisulfur radical, c) reduction of thiocarboxylates radical, and d) reduction of trisulfur radical.

Figure 4.1.10 shows the proposed mechanism for the reactions between polysulfides and esters. Initially, the nucleophilic attack of S_8^{2-} on the esters leads to the formation of poly-thiocarboxylates (Figure 4.1.10a). The reduction of these poly-

thiocarboxylates is facilitated in comparison to the reduction of pure S_8^{2-} due to the two stable products formed, the trisulfur radical, and a thiocarboxylate radical, which can be partially stabilized through resonance (Figure 4.1.10b). Both these radicals can then be further reduced, forming S_3^{2-} and a solid lithium thiocarboxylate (Figure 4.1.10c and d). The formation of a solid thiocarboxylate is first evidenced by the lack of bands related to it in the infrared spectrum of DME:DOL air (Figure 4.1.6a), in particular the absence of bands around 1700 cm^{-1} related to the carbonyl moiety. Interestingly, there is a weak signal in this region for DME:DOL Ar, indicating that there is indeed some formate formation in even when oxygen is not present, though the formation is probably slower. The extra reduction steps of Figure 4.1.10c and d would explain the increased intensity of the peak around 2.15 V vs. Li/Li^+ in Figure 4.1.5d. The formation of the solid lithium thiocarboxylate, however, seems to be irreversible, which would explain the loss in capacity during cycle. To further test this hypothesis, the impedance spectra of the cells was analyzed.

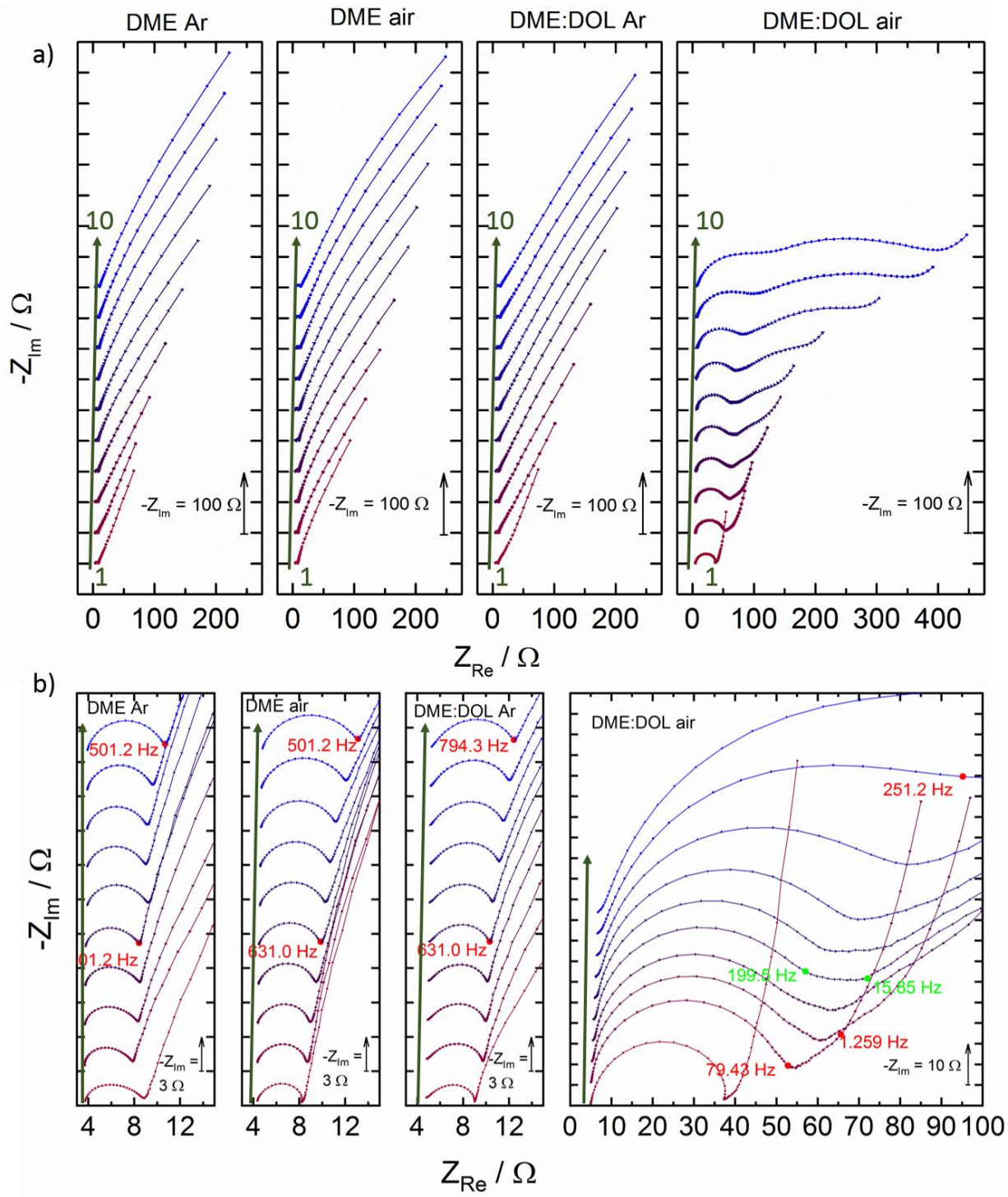

Figure 4.1.11. a) EIS spectra of AC/S cathodes at 3.0 V vs. Li/Li⁺ for the four different kinds of electrolytes, and b) magnification of the high frequency region of said spectra, with frequencies of interest highlighted. The vertical arrow on the left of each panel indicates the spectrum series, from the 1st to the 10th cycle. The vertical arrow on the right of the panels indicate the scale of the imaginary part (y-axis).

Figure 4.1.11 shows the Nyquist plots of AC/S cathodes after the initial 10 cycles (charged state) in the various electrolytes. It can be seen that for cells cycling in DME

Ar, DME air, and DME:DOL Ar, the spectra are similar, both between the different cells and the different cycles, showing a depressed semi-circle in the high frequency region, and a diffusion-related straight line at mid- and low-frequency region. This corroborates the results seen in Figure 4.1.3, in that the electrochemical behavior of sulfur in these electrolytes is similar. The spectra recorded for the cell in DME:DOL air, however, is remarkably different. Specifically, another depressed semi-circle appears in the mid-frequency range, which evolves upon further cycling. This feature is related to the formation of an additional passivation film over the electrode As proposed in Figure 4.1.10, the reduction of sulfur in DME:DOL air leads to the formation of solid thiocarboxylates, which are insoluble and precipitate over the electrode. The film grows over cycle, both consuming the active material, and blocking the electrode from reacting further. This, in turn, leads to the fast capacity decrease seen in Figure 4.1.3e. Figure 4.1.11b shows the magnification on the high-frequency region of the spectra. This semi-circle could be associated to the contact and pore impedances of the electrode material[155]. Again, the behavior for DME Ar, DME air, and DME:DOL Ar is quite similar. For DME:DOL air, the semi-circle appearing in this region is much larger and increases over cycling. This is again due to the precipitation of solid thio-carboxylates inside the cathode, resulting in pore-clogging, which leads to the increase of impedance. All this information corroborates the results presented so far and corroborate the proposed mechanism of DOL decomposition (Figure 4.1.7) and sulfur consumption (Figure 4.1.10).

4.1.4 *Post mortem* analysis of the cathode

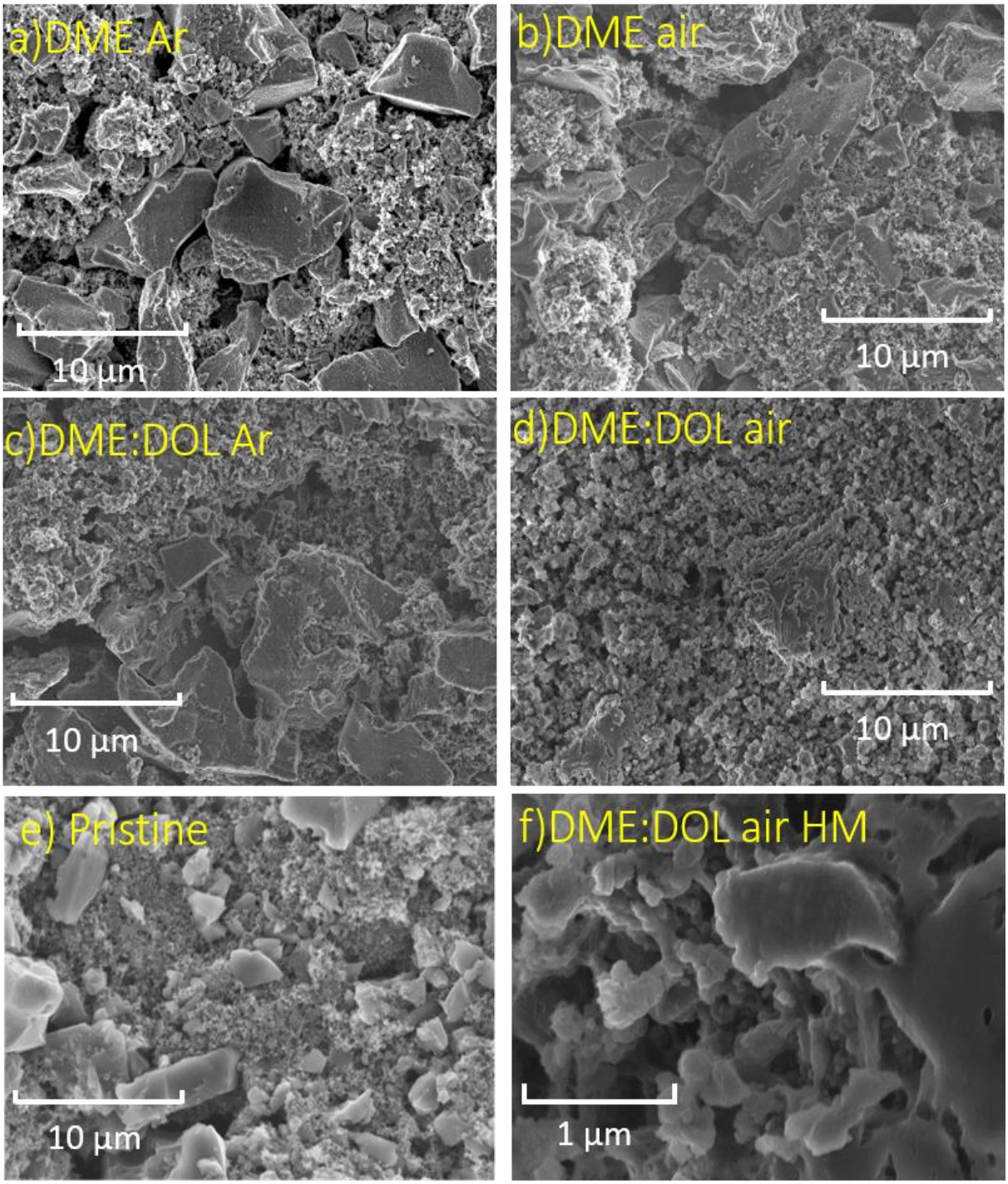

Figure 4.1.12. SEM images of the AC/S cathodes after 10 cycles in the electrolytes a) DME Ar, b) DME air, c) DME:DOL Ar, and d) DME:DOL air, compared to e) the pristine electrode. f) Shows a high magnification image of the electrode cycled in DME:DOL air.

The AC/S cathodes were analyzed by SEM to check for morphological differences after 10 cycles. As shown in Figure 4.1.12, the morphology of the electrodes where no

DOL decomposition happens (Figure 4.1.12a, b and c) are very similar to the pristine electrode (Figure 4.1.12e). Specifically, the large activated carbon particles are still clearly visible. The electrode cycled in DME:DOL air (Figure 4.1.12d and f) does not, however, show the AC particles. Instead, a deposit of undefined morphology is present over the entire electrode, which could be seen even with the naked eye, as a white precipitate over the electrode. This deposit is in agreement with the results of the impedance spectrum in Figure 4.1.11 for DME:DOL air. As a final confirmation of the reactions proposed so far, the XPS spectra of the cycled cathodes was analyzed.

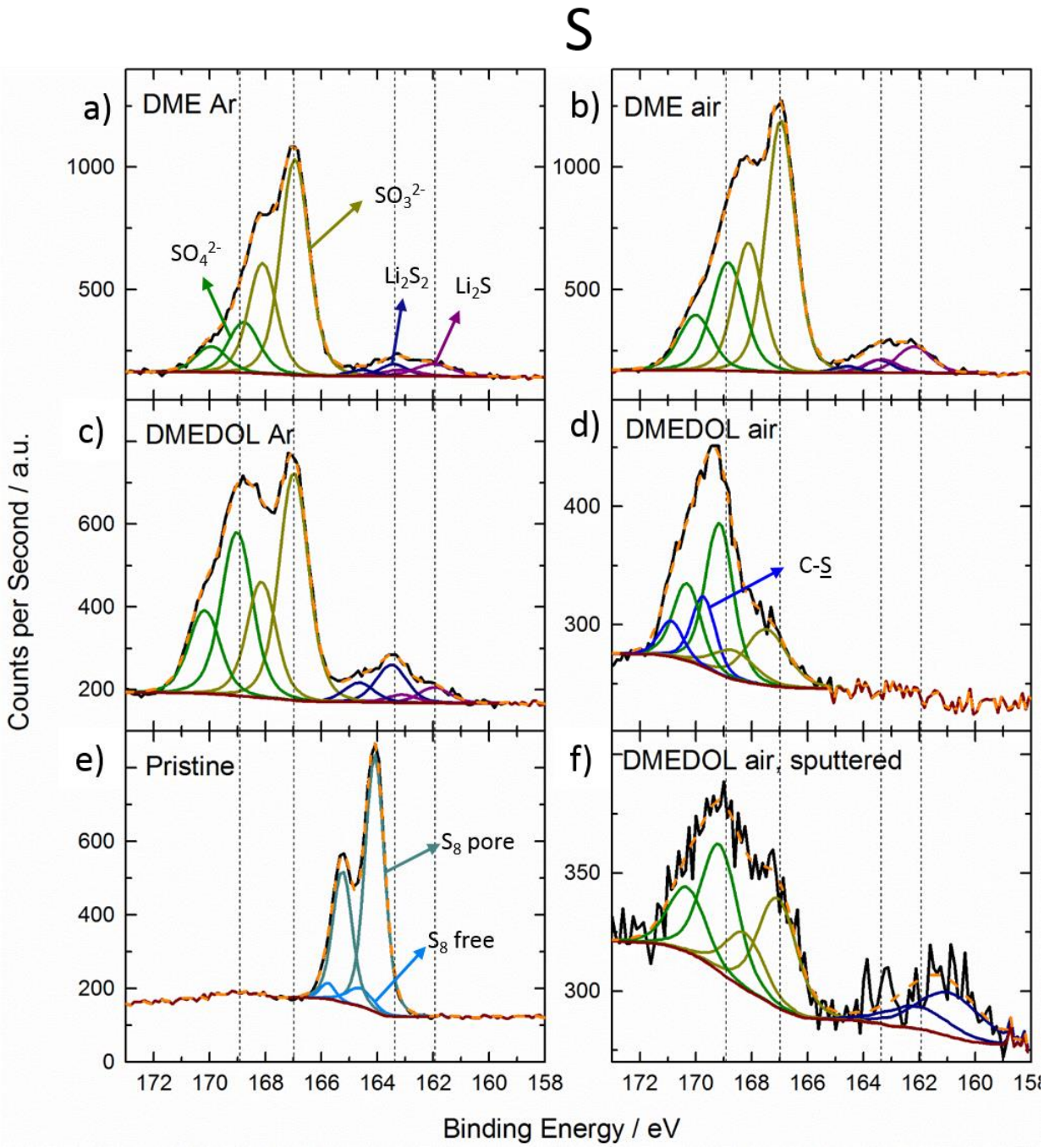

Figure 4.1.13. XPS spectra of sulfur binding energy region, for AC/S charged (3.0 V vs. Li/Li^+) cathodes cycled in a) DME Ar, b) DME air, c) DME:DOL Ar, and d) DME:DOL air. e) The spectrum of the pristine cathode for comparison. f) The cathode cycled in DME:DOL air was also sputtered for 2 minutes to remove the top layer off of the cathode. Black lines show the raw data, brown line the background, and the orange dashed lines are the spectral envelope.

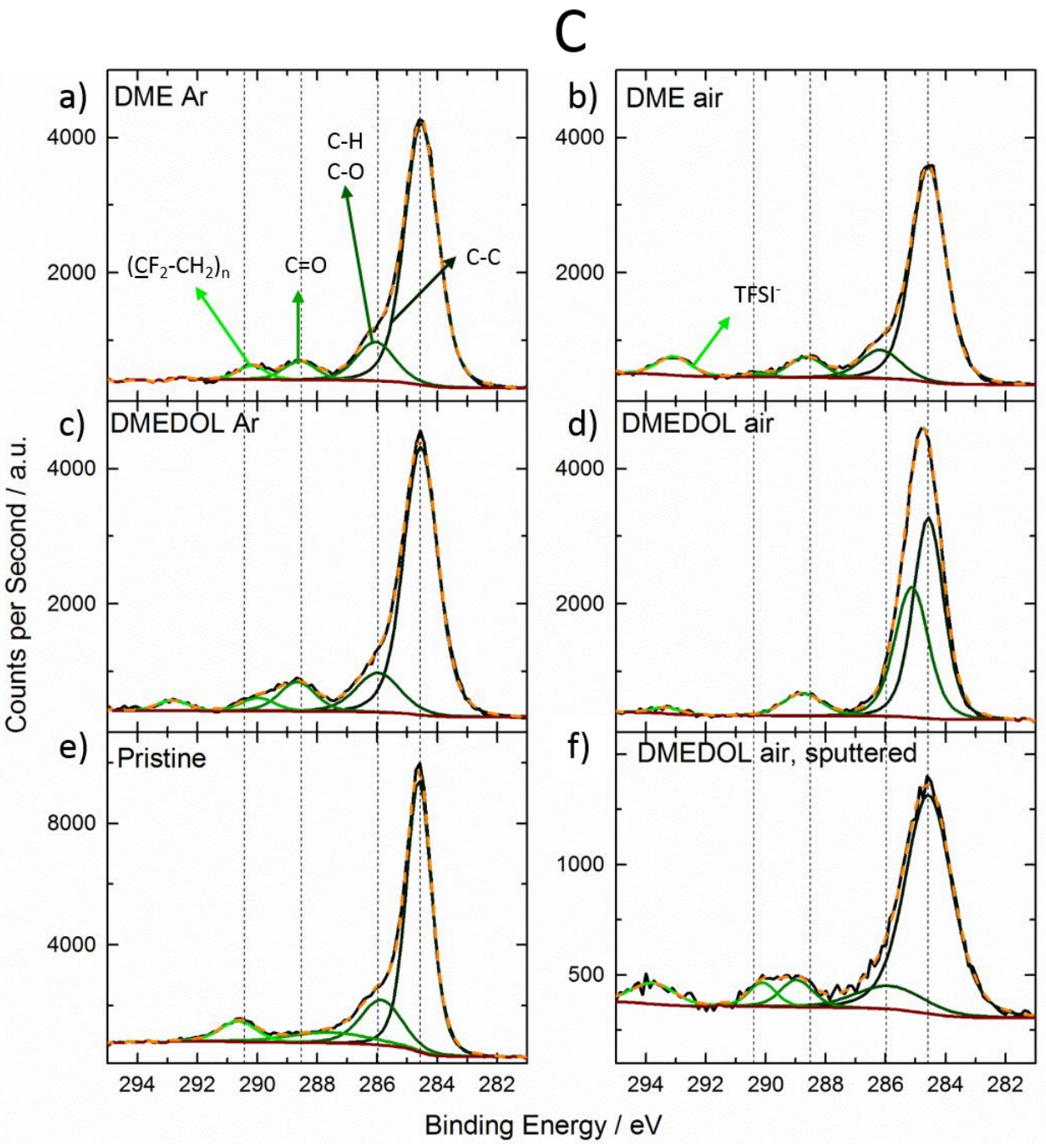

Figure 4.1.14. XPS spectra of carbon binding energy region, for AC/S charged (3.0 V vs. Li/Li⁺) cathodes cycled in a) DME Ar, b) DME air, c) DME:DOL Ar, and d) DME:DOL air. e) The spectrum of the pristine cathode for comparison. f) The cathode cycled in DME:DOL air was also sputtered for 2 minutes to remove the top layer off of the cathode. Black lines show the raw data, brown line the background, and the orange dashed lines are the spectral envelope.

Figure 4.1.13 and Figure 4.1.14 show the XPS spectra of the pristine and cycled AC/S cathodes in the sulfur and carbon regions, respectively.

The sulfur spectra for the cathodes cycled in DME Ar, DME air, and DME:DOL Ar (Figure 4.1.13a, b, and c, respectively) present small peaks coming from irreversibly reduced Li_2S (S $2p_{3/2}$ 161.9 eV) and Li_2S_2 (S $2p_{3/2}$ 163.4 eV)[66], and more intense peaks from SO_3^{2-} (S $2p_{3/2}$ 166.9 eV) and SO_4^{2-} (S $2p_{3/2}$ 168.9 eV)[156], the latter due to reactions with nitrate in the electrolyte[153,157]. Interestingly, there is no visible peak related to S_8 molecules. The binding energy related to S_8 molecules can be seen in the sulfur spectrum of the pristine cathode (Figure 4.1.13e), consisting mostly of sulfur trapped inside AC pores (S $2p_{3/2}$ 164.1 eV)[66] and some small amount of free sulfur (S $2p_{3/2}$ 164.6 eV)[158]. However, most importantly, the spectrum of the electrode cycled in DME:DOL air shows some striking differences. Firstly, in the sulfur spectrum, no peaks associated to Li_2S or Li_2S_2 are observable, but only those related to SO_3^{2-} and SO_4^{2-}. Another peak is also present, which is attributed to C-S bonds (S $2p_{3/2}$ 169.7 eV)[159]. This C-S bond is a good indication that there is, indeed, some thiocarboxylate on the surface of the electrode. The peaks related to Li_2S and Li_2S_2 have both disappeared, indicating that the passivation layer has possibly been covered by the passivation layer. To test this, the upper layer was removed by sputtering it with an ion beam. The spectrum after sputtering (Figure 4.1.13f) shows that, when the top layer is removed, the underlying electrode resembles much more the other systems (Figure 4.1.13a, b, and c), with the disappearance of the C-S peak, and reappearance of the Li_2S peak. The intensities, however, are much smaller, indicating that the majority of sulfur is found in this passivation layer.

The carbon spectra for the electrodes tested with DME Ar, DME air, and DME:DOL Ar electrolytes (Figure 4.1.14a, b, and c) display peaks for C-C bonds (C 1s 284.6 eV), C-H and C-O (C 1s 285.9 eV), C=O (C 1s 288.7 eV) coming from AC, and C-F (C 1s 290.5 eV) from the PVdF binder[66,160,161]. In some of the spectra, a small amount of $TFSI^-$ is detected as well (C 1s 293.1 eV)[160], probably from leftover salt on the electrode. Other than the peak of $TFSI^-$, all are also present in the pristine electrode (Figure

4.1.14e), though with different intensities. The spectrum for DME:DOL air (Figure 4.1.14d) presents some differences, similar to the case of Figure 4.1.13. The most notable ones are the complete disappearance of the PVdF peak, and a much more pronounced C-H and C-O peak in comparison to the C-C peak. The disappearance of PVdF peak can be ascribed, once again, to the formation of a passivation layer, which covers the underlying electrode. The increase of C-H and C-O peak, in turn, is due to the formation of lithium alkoxides over the electrode, in accordance with the mechanism in Figure 4.1.10a. As expected, the carbonyl peak is still present, showing that there is plenty of thiocarboxylate forming the passivation layer. After the electrode is sputtered (Figure 4.1.14f), the spectrum once again resembles much more that of the other electrodes, with a decrease in the peak related to C-H/C-O (alkoxides), and the resurgence of the PVdF peak.

The XPS data presented herein gives further proof of the presence and nature of the passivation layer over the electrode when the electrolyte containing both DOL and O_2 is used in lithium-sulfur cells, specially the difference between sputtered and unsputtered electrodes.

To summarize this chapter, the effect of dissolved oxygen in the state-of-the-art electrolyte for Li-S batteries was thoroughly investigated. It was found that dissolved oxygen promotes the decomposition of 1,3-dioxolane by initiating polymerization and isomerization, the latter forming organic esters that react with polysulfides formed during discharge and leading to early cell death. Though the initial motivation was to assess the feasibility of assembling sulfur cells in normal atmosphere, and not an inert one, the study allowed some more in-depth understanding of the sulfur electrochemistry.

Firstly, the results are directly translatable to cells using radical-forming additives, or additives derived from carboxylic acid[162]. Additives coming from carboxylic acids should be avoided in all cases, and additives which form radicals should be avoided

in electrolytes containing DOL, since these conditions lead to the formation of thiocarboxylates in the cell. Thiocarboxylates formed in this way can passivate and remove active material from the cathode, leading to strong capacity fading.

Secondly, the role of DOL in the passivation layer was better understood. Through the polymerization of DOL, a stable, albeit resistive, SEI could be formed over the lithium surface, to the point where a great amount of nitrate ions are left unreacted in comparison to standard electrolyte formulations. This is a valuable information in the search of stable SEIs to enable the usage of lithium metal anodes in lithium batteries.

Finally, the presence of organic esters in the electrolyte was shown to enhance the reduction of long-chain polysulfides in the liquid phase, which greatly increased the capacity that could be extracted from the cell. This, however, came at the expense of cell capacity retention, since the reaction of polysulfide with ester is irreversible, and quickly consumes the active material. If, however, a catalyst can be found, which enhances this reaction without irreversibly consuming the active material, a great improvement in capacity for sulfur cathodes can be expected.

4.2 Ethylenediamine-embedded lithium sulfide – characterization and carbonization

Recently, many researchers are considering lithium sulfide (Li_2S) as active material for LSBs[116,117]. The main motivation behind this choice is that Li_2S already contains lithium, in theory avoiding the need of using the lithium metal anode for the battery assembly, which is notoriously dangerous. However, Li_2S has disadvantages, too, requiring an energy-consuming and harsh activation step related to the first lithium extraction from the highly crystalline lithium sulfide particles[109]. In this chapter, a novel kind of lithium sulfide material is synthesized by co-precipitation of the constituents in ethylenediamine. Herein, the full characterization of the material is given. Electrochemical tests of the material are given in chapter 4.3.

4.2.1 Experimental procedures

All procedures described in this section were carried out under inert atmosphere. All the handling of chemicals, chemical and sample preparations, measurements, and cell assembly were conducted either in a GloveBox filled with argon (O_2 and H_2O contents below 0.1 ppm) or using standard Schlenk techniques.

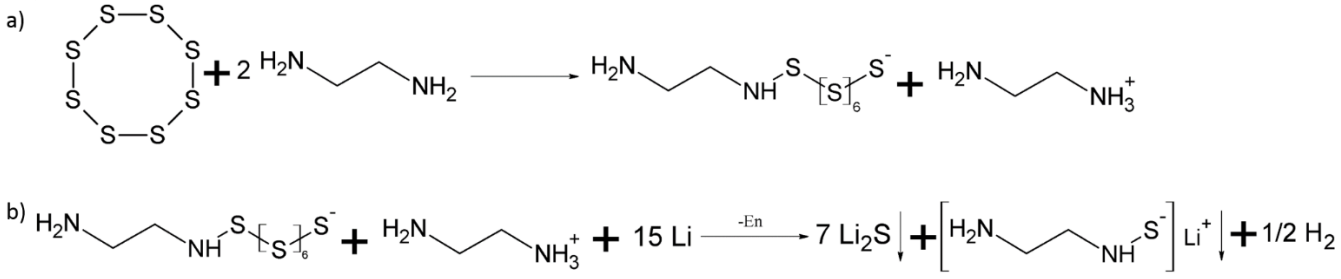

Figure 4.2.1. Scheme of Li_2S-En synthesis. a) Dissolution of S_8 molecules in ethylenediamine, forming an En-S_8 complex. b) Reduction of En-S_8 complex using metallic lithium.

Amorphous lithium sulfide was prepared in house by reacting metallic lithium (Abermarle Lithium) with elemental sulfur (Sigma-Aldrich) in ethylenediamine (EDA, Alfa-Aesar) (Figure 4.2.1). In a round bottom flask, 1.03 g (32.2 mmol) of sulfur were

dissolved in 50 mL of ethylenediamine. After all solid had been dissolved, the solution was slowly (dropwise) transferred to another flask containing 0.487 g (69.6 mmol) of metallic lithium. In a round bottom flask, 1.03 g (32.2 mmol) of sulfur were dissolved in 50 mL of ethylenediamine. After complete dissolution, the solution was slowly (dropwise) transferred to another flask containing 0.487 g (69.6 mmol) of metallic lithium. The reaction was extremely exothermic and heated up considerably, such that a reflux condenser was fitted over the flask to avoid solvent loss. The reaction was allowed to take place until all lithium was consumed, for around 2 hours. The reaction mixture turned black as the reaction progressed. After complete reaction, the solid precipitate was filtered off and collected. The precipitate was a dark-purple powder which turned slightly dark brown after drying at 50 °C and below 10^{-3} mbar for 24h. Elemental analysis (Elementar vario MICRO cube) and induced coupled plasma atomic emission spectroscopy (ICP-AES, Ultima 2: Horiba Jovin Yvon) revealed the compound to be composed of lithium sulfide and 12% (w/w) of ethylenediamine, even after drying. The compound, hereinafter labeled as Li2S-En, was analyzed by X-ray diffractometry (XRD, Bruker D8 Advance difractometer, Bruker) using a CuKα (λ = 0,154 nm) monochromatic X-ray source with Bragg-Brentano geometry, X-ray photoelectron spectroscopy (XPS, PHI 5800 MultiTechnique ESCA System, Physical Electronics), infrared spectroscopy (IR, PerkinElmer) in the attenuated total reflectance (ATR) mode, and scanning electron microscopy (SEM, Zeiss LEO 1550VP). Commercial Li2S (Abermarle Lithium) was used as reference material for the different characterizations. To test the reactivity of the material, it was mixed in a 1:1 (w/w) ratio with two different ionic liquids. 1-butyl-1-methylpyrrolidinium tricyanomethanide (Pyr1,4TCM, IoLiTec) and 1-butyl-3-methylimidazolium tricyanomethanide (EMImTCM, IoLiTec) were dried under vacuum for 48 hours and used without further purification.

Attempts to carbon-coat the material were also carried out. In a first attempt, it was mixed in a 1:1 (w/w) ratio with two different ionic liquids. 1-Butyl-1-methylpyrrolidinium tricyanomethanide ($Pyr_{1,4}TCM$, IoLiTec GmbH) and 1-butyl-3-methylimidazolium tricyanomethanide (EMImTCM, IoLiTec GmbH) were dried under vacuum for 48 hours and used without further purification. These ionic liquids are known to be good carbon sources for the carbon-coating process[163,164]. However, it was found that Li_2S-En is too reactive, as is shown in section 4.2, leading to decomposition of both the ionic liquid and of the active material. Thus, the material was carbon-coated by simply heating it to 400 °C under argon atmosphere. Li_2S-En was loaded into an alumina (Al_2O_3) boat and placed inside a quartz tube. The tube was placed inside a horizontal furnace (Nabertherm R 50/250/12 P330), under a constant stream of argon. The sample was heated at a rate of 5 °C min^{-1} up to 400 °C, and kept at 400 °C for 5 hours, and turned light grey afterwards. The obtained material, named Li_2S-CC, was characterized by XPS, XRD, Raman spectroscopy (Renishaw InVia confocal Raman microscope), and induced coupled plasma atomic emission spectroscopy (ICP-AES, Ultima 2: Horiba Jovin Yvon). It was shown to be composed of 94% Li_2S and 6% carbon-coating, with the carbon coating itself composed of 64% carbon and 36% nitrogen (all values given as weight percentages).

4.2.2 Infrared characterization of Li_2S-En

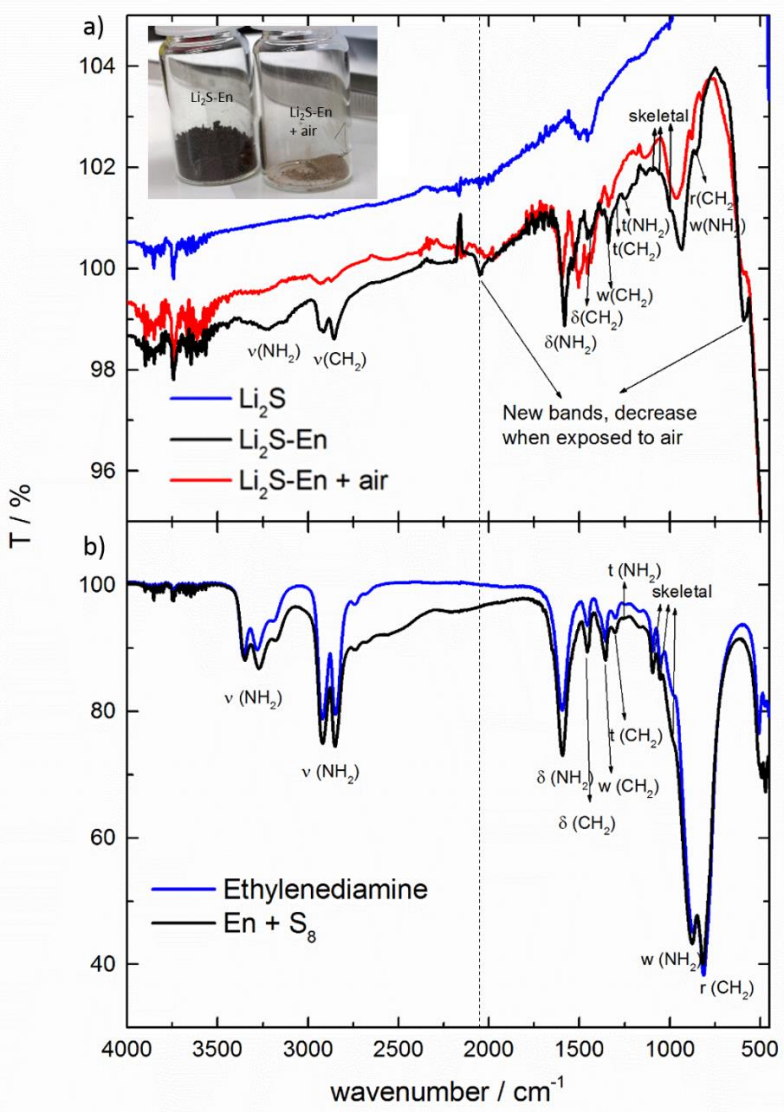

Figure 4.2.2. a) FTIR spectra of Li_2S-En, Li_2S-En exposed to ambient air, and commercial Li_2S. Inset: Photographic pictures of Li_2S-En and Li_2S-En exposed to air. b) FTIR spectra of pure ethylenediamine and a saturated solution of S_8 in ethylenediamine. Abbreviations for the different vibration modes: ν = stretching, δ = deformation, w = wag, t = twist, r = rock.

The synthesis of Li_2S-En was carried based on the known formation of a complex between molecular sulfur and ethylenediamine[165,166] (Figure 4.2.1a). The reaction is expected to form both Li_2S and a lithium sulfenamide (Figure 4.2.1b), which co-precipitate to form a solid compound. This co-precipitated compound was called Li_2S-En, and is formed by both normal lithium sulfide and lithium sulfenamide.

In Figure 4.2.2a the IR spectra of Li_2S-En, Li_2S-En exposed to ambient air, and commercial Li_2S are shown. The same is done in Figure 4.2.2b for pure ethylenediamine and a saturated solution of elemental sulfur in ethylenediamine. The bands of ethylenediamine are identified in Figure 4.2.2b, which attribution was done according to literature[167]. The same peaks are observed for Li_2S-En, whereas commercial Li_2S shows no peaks in the same regions. This is a clear evidence of the presence of ethylenediamine in the synthesized material even after drying, indicating that ethylenediamine is strongly bound into the obtained compound. This strong interaction is probably due to the covalent bonding of the amine's nitrogen with sulfur, established upon sulfur dissolution in ethylenediamine[165,166], but retained even after the sulfur is reduced to Li_2S. Unfortunately, the compound is very sensitive to oxidation, making difficult to work with[165], such that the IR characterization of this compound, i.e., appropriate references for this band, is not straightforward. Comparing the two IR spectra in Figure 4.2.2b, the only notable difference in the presence of sulfur is the increased intensity of the region between 2600 and 1800 cm^{-1} due to two very broad bands. When sulfur is dissolved in amine solvents, the S_8 molecules undergo a ring-opening reaction, and the sulfur chains produced this way become attached to the amines. These sulfur chains can rearrange themselves through the cleavage and recombination of the S-S bonds, which means they form compounds with different polysulfide chain lengths[166]. Thus, it is reasonable to expect that the S-N bond presents a broad absorption band, since its chemical environment is very diverse, similar to the hydrogen bonded hydroxyl groups versus free-standing hydroxyl groups[168]. In the spectrum of Li_2S-En, a new band is present in this region, namely at 2050 cm^{-1}, which cannot be attributed to ethylenediamine. However, it might be associated to the S-N bond of the fully reduced Li_2S-En compound. A further evidence of this hypothesis is that, when exposed to air, the compound drastically changes color from dark brown to light brown (see Figure 4.2.2a, inset), while the infrared

spectrum shows a decrease of the bands associated with ethylenediamine and the complete vanishing of the new bands. All these evidences are consistent with the oxidation of the S-N bond existing in the Li_2S-En compound.

4.2.3 Carbon coating of lithium sulfide

Initial attempts to carbon-coat lithium sulfide were carried out using TCM-based ionic liquids as carbon sources, as discussed in section 4.2.1.

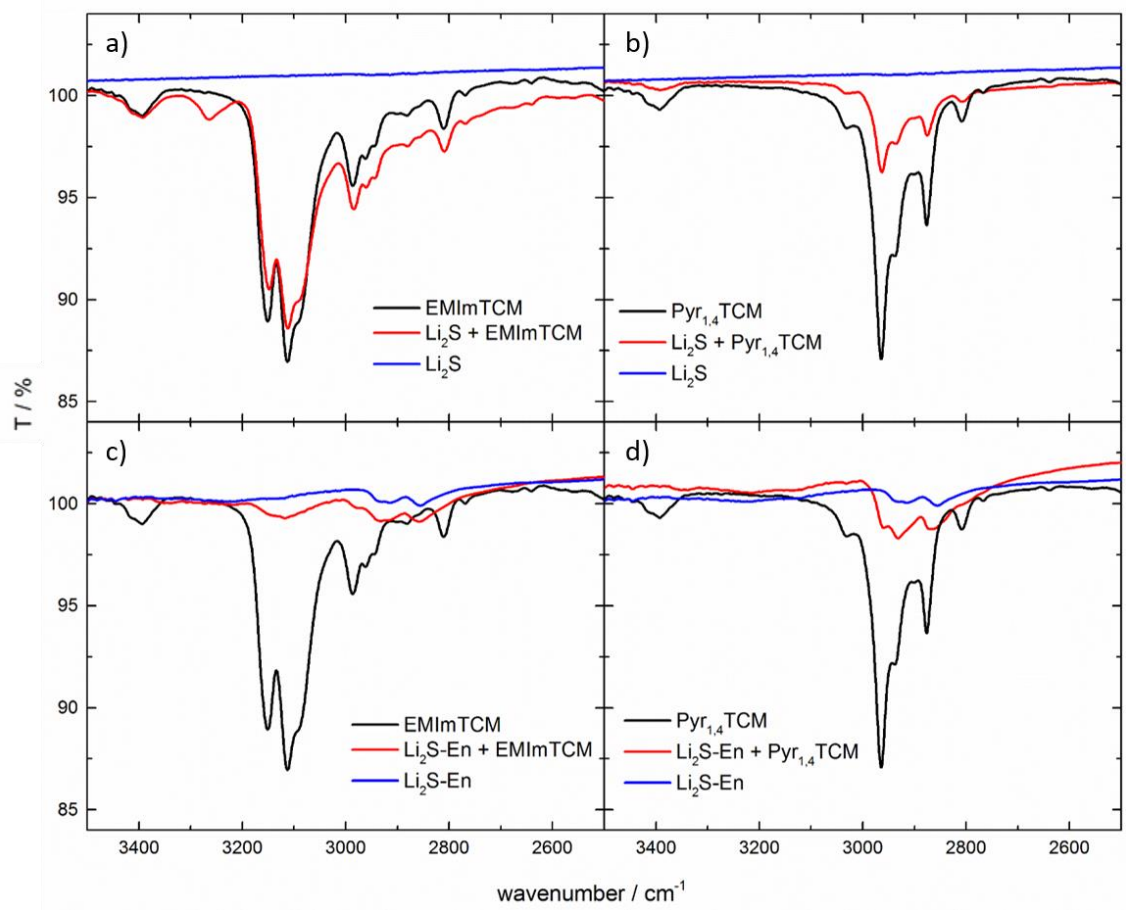

Figure 4.2.3. ATR-FTIR spectra of different 1:1 mixtures of ionic liquids and lithium sulfides. a) Commercial Li_2S and EMImTCM; b) commercial Li_2S and $Pyr_{1,4}TCM$; c) Li_2S-En and EMImTCM; d) Li_2S-En and $Pyr_{1,4}TCM$. The spectra of the pure components are also shown in each panel for comparison (cf. legend).

Li_2S-En was found to be extremely reactive. For example, the compatibility of the active material with some ionic liquids (ILs) was tested by IR. In Figure 4.2.3, the region related to the cation vibrations (high wavelength)[169,170] is shown. In the case of Li_2S with two different ILs, EMImTCM and $Pyr_{1,4}TCM$ (Figure 4.2.3a and b,

respectively), the bands remain mostly the same. In the case of EMImTCM, there is a new band at 3260 cm^{-1} due to the interaction of the acidic hydrogen of $EMIm^+$ with the sulfide ions. For $Pyr_{1,4}^+$, there is a decrease in the intensity of all bands, probably because the ionic liquid did not spread well over the Li_2S particles. In the case of the mixtures with Li_2S-En (Figure 4.2.3c and d), there is a complete vanishing of the cation bands, with new ones evolving. Sulfides are actually known to react with both these cations[171]. Ionic liquids containing both these cations with bisulfide anion (HS^-) have been shown to be prone to decomposition through attack of the highly nucleophilic anion. However, this kind of decomposition reactions normally happen at elevated temperatures and/or under vacuum. In the case of Li_2S-En, this happens at room temperature and atmospheric conditions. This is probably due to the higher nucleophilicity of the S^{2-} anion, which reacts more vigorously than HS^-. In the case of commercial Li_2S, however, the highly reactive sulfide ions are stabilized by the high lattice energy of the crystalline solid, of around 2470 kJ mol^{-1} [172]. In the case of Li_2S-En, its amorphous nature means that the lattice energy is much smaller, and the sulfide ions are not stabilized, making them much more reactive. This proved troublesome when preparing electrodes with Li_2S-En as active material, for example, as Li_2S-En would immediately react with NMP, the solvent used to prepare electrode slurries using PVdF as binder. The material was stable when in contact with toluene, such that a PIB dissolved in toluene was used to prepare slurries instead. The electrochemical performance of such electrodes will be discussed in section 4.3.

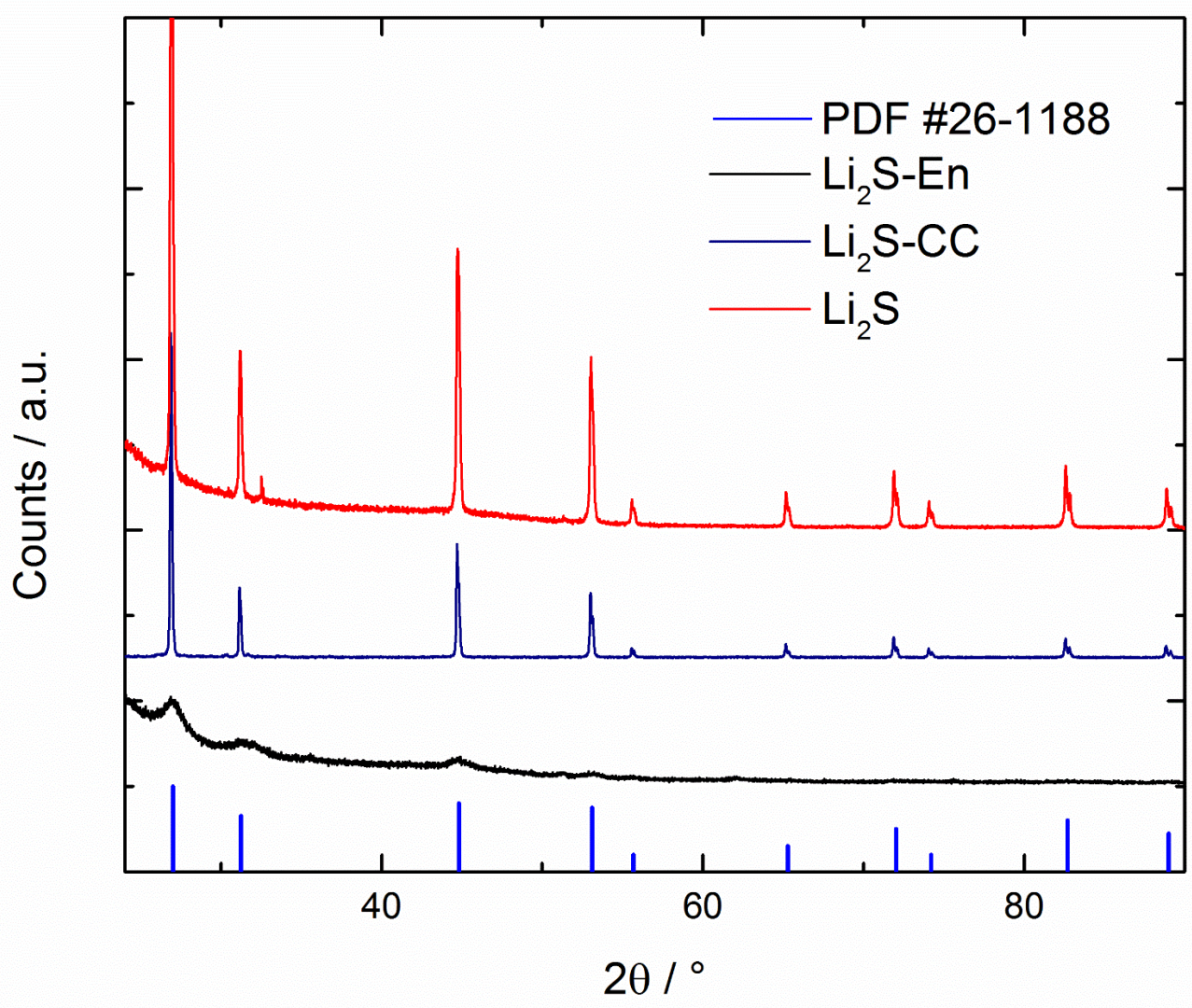

Figure 4.2.4. XRD diffractogram of commercial Li_2S, Li_2S-En, and the predicted diffraction peaks.

The XRD diffractogram of Li_2S-En, Li_2S-CC, and commercial Li_2S are shown in Figure 4.2.4. As evident from the diffractogram, Li_2S-En does not show any intense diffraction peaks, unlike the commercial Li_2S displaying sharp peaks at the expected angles (see powder diffraction file #26-1188). The lack of diffraction peaks indicates that Li_2S-En is mostly amorphous. This is probably due to the incorporation of the large ethylenediamine, in the form of NH_2-CH_2-CH_2-NH-S-Li, on the freshly formed Li_2S-En, hindering the growth of Li_2S crystals. This means that Li_2S-En cannot crystallize properly, and does not form the regular crystal planes required to give rise to the typical diffraction peaks. However, the XRD diffractogram of Li_2S-CC shows striking differences

compared Li_2S-En, with clear diffraction peaks corresponding to the presence of crystalline Li_2S. This is probably due to the release of the sulfenamide molecules during the carbonization and annealing of the sample allowing for the crystallization of the particles

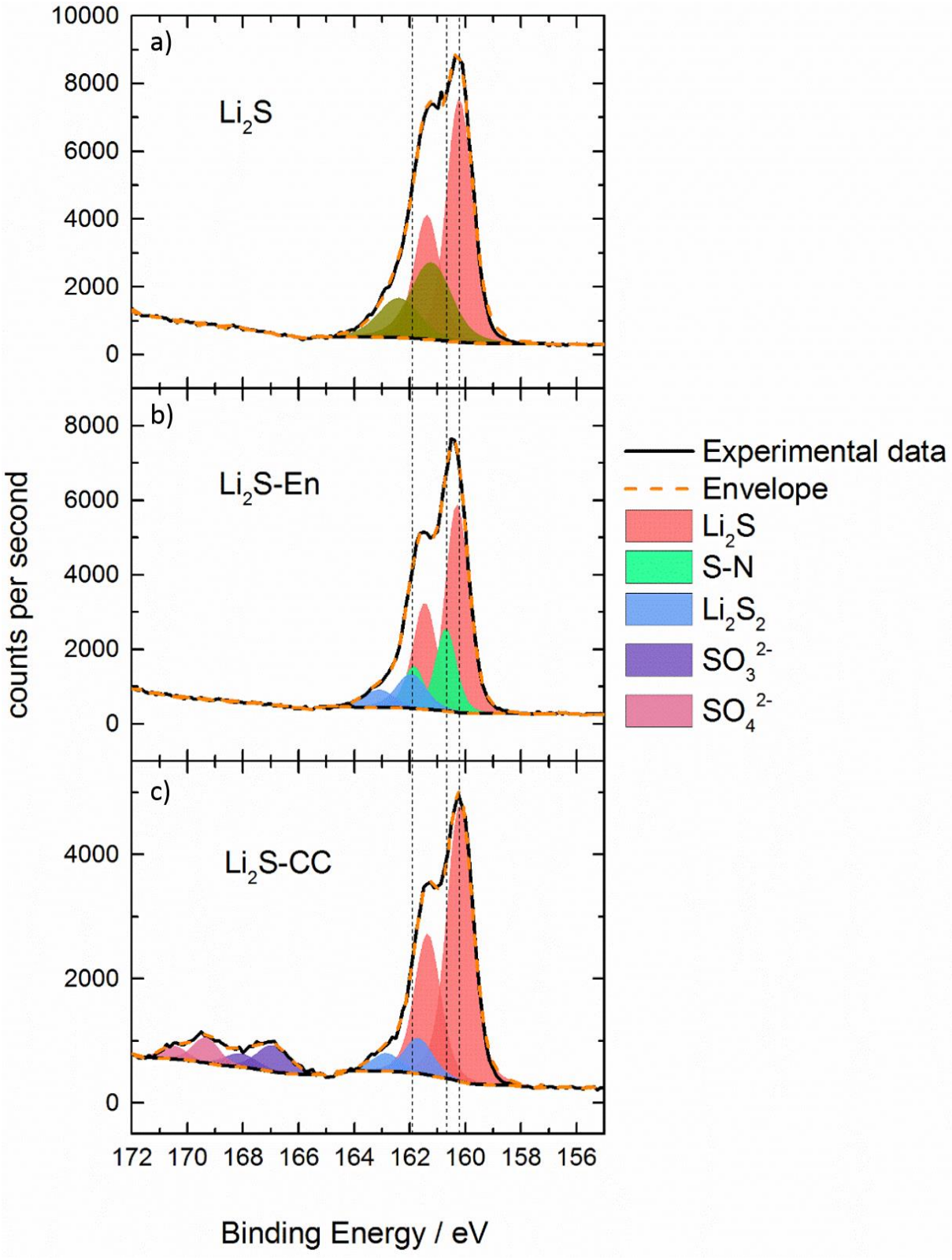

Figure 4.2.5. XPS spectra of a) Li_2S, b) Li_2S-En, and c) Li_2S-CC in the sulfur region

Figure 4.2.5 shows the XPS spectra of Li_2S-En and Li_2S-CC and compares them to commercially available Li_2S, as well as the deconvolution of those. The main peak,

which is due to S^{-2} ions, is centered at 160.3 eV ($S2p_{3/2}$) in all three samples[66]. Commercial Li_2S (Figure 4.2.5a) shows also a feature located at 161.3 eV ($S2p_{3/2}$) most likely due to the native layer covering the Li_2S particles (such as LiOH, LiSH, Li_2CO_3)[116]. Most interestingly, however, is the case of Li_2S-En showing two additional peaks ($S2p_{3/2}$) centered at 160.7 and 162.0 eV. The peak at higher binding energy is attributed to the disulfide ion (S_2^{2-}), suggesting the presence of a small amount of sulfur not completely reduced on the surface. The peak with binding energy 160.7 eV is attributed to the sulfur bonded to nitrogen instead, possibly in the sulfenamide NH_2-CH_2-CH_2-NH-S^-. The proximity of binding energy to that of S^{2-}/S_2^{2-} ions suggests that, indeed, the sulfur in this case is chemically similar to those ions, i.e., there is a negatively charged sulfur atom in the molecule. When the sample is carbonized (Figure 4.2.5c) the spectrum changes once again. The spectrum highly resembles that of Li_2S-En (Figure 4.2.5a). The most notable differences are the disappearance of the S-N peak and the presence of two small peaks at higher binding energies. These peaks are due to SO_3^{2-} (S $2p_{3/2}$ 166.9 eV) and SO_4^{2-} (S $2p_{3/2}$ 168.9 eV)[156], which formed due to traces of oxygen in the furnace during carbonization. The disappearance of the S-N peak, in turns, is due to the decomposition of the sulfenamide at high temperatures.

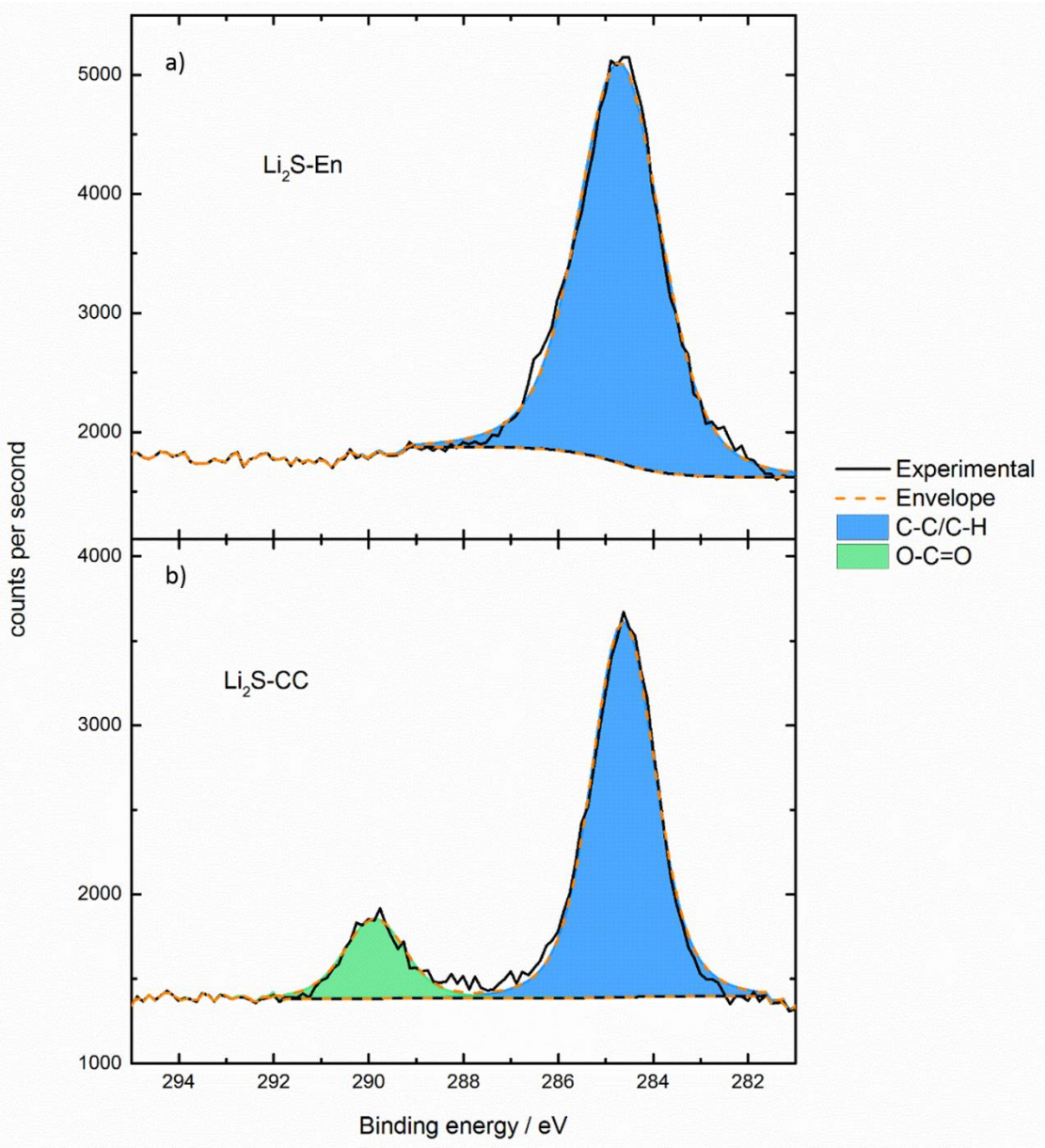

Figure 4.2.6. XPS spectra of a) Li_2S-En and b) Li_2S-CC in the carbon region

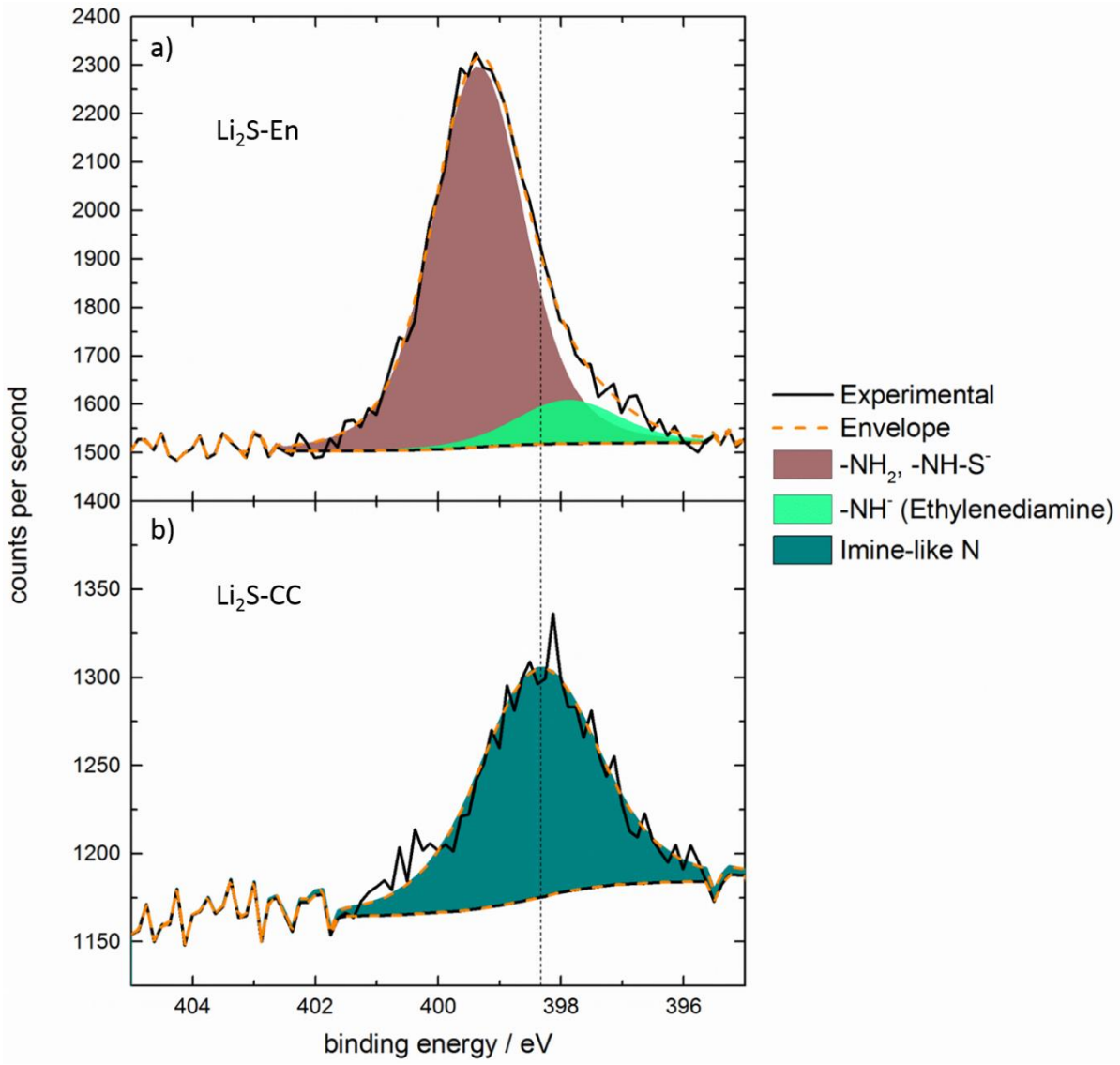

Figure 4.2.7. XPS spectra of a) Li_2S-En and b) Li_2S-CC in the nitrogen region

The XPS spectra of Li_2S-En and Li_2S-CC in the carbon (Figure 4.2.6) and nitrogen (Figure 4.2.7) regions show some small differences. The carbon spectra in both cases are similar, dominated by a peak at 284.6 eV corresponding to carbon-carbon bonds. After carbonization, there is a small peak at 289.9 eV due to carbon oxidation, again from small amount of oxygen contamination in the protecting gas. The nitrogen spectra, on the other hand, shows bigger differences. For Li_2S-En a main peak is located at 399.4 eV, and corresponds to the amine moiety. A small bond at 397.9 eV is also present, probably from a small amount of reduced ethylenediamine with the excess lithium. Interestingly,

the sample after carbonization is rich in nitrogen, showing an imine-like nitrogen peak[173,174], also a result of the sample carbonization..

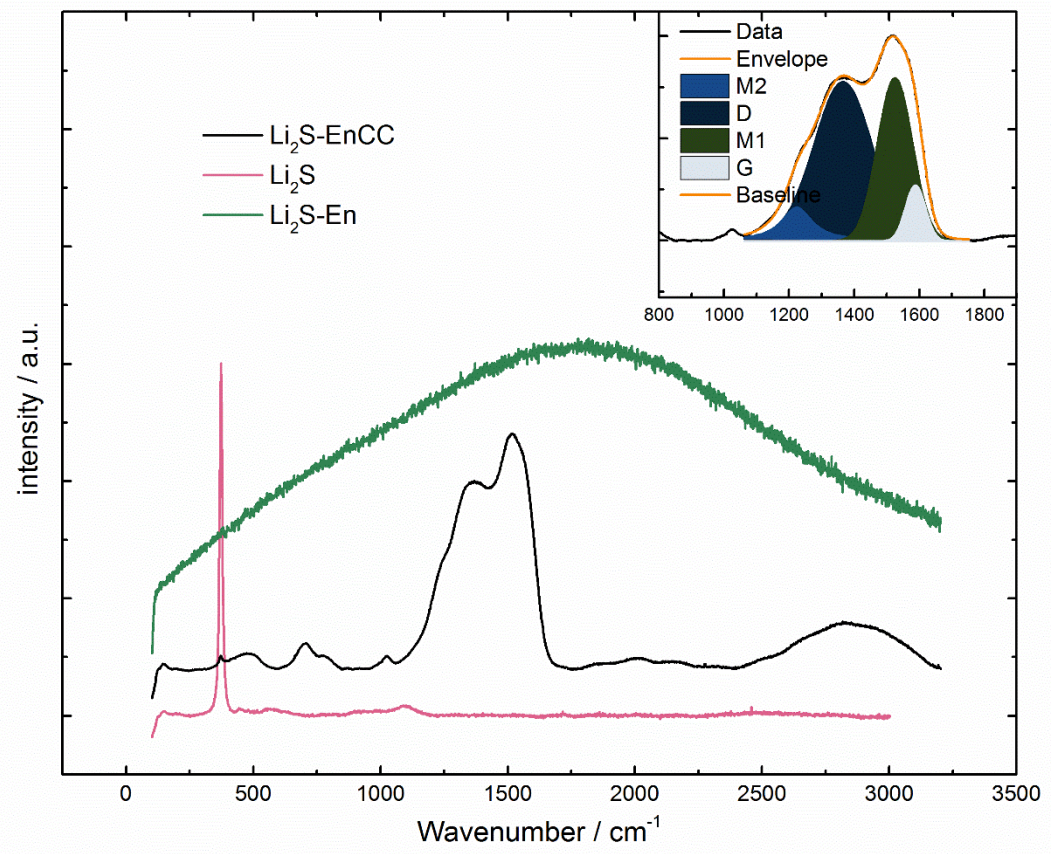

Figure 4.2.8. Raman spectra of commercial Li_2S and Li_2S-CC. Inset shows the deconvolution of peaks between 1100 and 1700 cm^{-1}.

Figure 4.2.8 shows the Raman spectra of Li_2S-CC, Li_2S, and Li_2S-En. The spectrum of Li_2S-En showed no scattering peaks, but only a very strong fluorescence signal. For Li_2S only one peak centered at 375 cm^{-1} is clearly noticeable. In the spectrum of Li_2S-CC this peak is also detected, but it appears very weak, indicating that the lithium sulfide particles are well covered by the carbon coating. Additional features are more predominant instead, mainly those between 1100 and 1800 cm^{-1} typical of carbonaceous material. These peaks can be separated into four distinct contributions by deconvolution (Figure 4.2.8, inset). The G band, centered at 1600 cm^{-1}, is attributed to the in-plane vibration of the condensed aromatic rings of the graphitic domains of the carbon coating, whereas the D band, centered at 1360 cm^{-1}, is related to edge defects in

the graphitic domains[175]. The two extra bands (M1 and M2) resulting from the fitting have been attributed to several decomposition compounds formed during pyrolization of the precursor[176]. The high ratio of the D to G band intensities (i.e., I(D)/I(G) = 2.37) support for an extremely low level of graphitization of the carbon coating.

In summary, the synthesis of a new lithium sulfide-based material has been carried out, and the material itself thoroughly characterized. The material was shown to be composed of a mixture of lithium sulfide, and a lithium sulfenamide. The presence of lithium sulfonamide was confirmed by both the presence of ethylenediamine-like bands in the infrared spectrum of the material, as well as some new bands, which could be attributed to the sulfur-nitrogen bond. The presence of this bond was also indicated by the XPS analysis of the compound. These two components were shown to co-precipitate out of solution during synthesis, to form an amorphous solid, in comparison to the highly crystalline lithium sulfide. This lower crystallinity rendered the material extremely reactive, which showed troublesome when handling it.

The sulfenamide also showed to be a reasonable carbon source for carbon coating, where simply heating the material under inter atmosphere is enough to render it carbon coated. The material did not show, however, the same S-N bond that Li_2S-En possess, showing that the sulfenamide was decomposed by the high temperatures.

The electrochemical behavior of both these materials is shown in the next chapter.

4.3 Effect of aged electrolyte in lithium sulfide-based cells

The effect of decomposition of the electrolyte shown in section 4.1 is a good evidence that this aspect has to be taken into account when designing lithium sulfur cells. This is particularly important when using lithium sulfide as cathode material. As previously mentioned, lithium sulfide must be activated up to high potentials (>4 V vs. Li/Li^+) before becoming electrochemically active, which raises concerns regarding side-effects from the decomposition of the ether-based electrolytes commonly used in Lithium-Sulfur batteries. In this chapter, the effect of such high activation potential is studied.

4.3.1 Experimental procedures

Cells using commercial Li_2S, Li_2S-En, and Li_2S-CC as active material were prepared to study the effect of aged and fresh electrolyte on the performance of cells (cf. section 4.2.1 for the different materials preparation).

In this part of the work, two different electrolytes were tested, which were prepared as follows. DME and DOL were mixed in a 1:1 volumetric ratio, and the mixture used as solvent for the electrolyte. Previously, the solvents were separately dried with 3Å molecular sieves, until the water content was below 20 ppm, similar to what is described in section 4.1.1. The solvent mixture was used to dissolve LiTFSI and $LiNO_3$ to a respective concentration of 1 and 0.25 mol L^{-1}. The electrolytes were stored in aluminum bottles. The two different electrolytes studied were labeled as "fresh" and "aged". The fresh electrolyte was prepared up to two weeks prior to the experiments. The aged electrolyte had been prepared more than a year prior to starting the experiments. Both were stored in the same conditions (sealed aluminum bottle inside the above mentioned glove box).

Electrodes using Li_2S-En as active material were prepared using polyisobutylene (PIB, BASF) as binder. Li_2S-En was manually ground with Super C65, and after the components were thoroughly mixed, a solution of 10 mg ml^{-1} of PIB in toluene (Sigma-

Aldrich) was added, and the components mixed further until a homogeneous slurry was formed. The final mass ratio of the components was 57:33:10 for Li_2S-En:Super C65:PIB, respectively. The slurry was then also cast over an aluminium current collector, and the electrodes dried at 60 °C under normal pressure. The electrodes were used in *Swagelok*-type three-electrodes T cells, with lithium metal as both counter and reference electrode, to test the impact of activation potential on the electrochemistry of Li_2S-based cathodes. The electrodes were kept apart by a glass fiber separator, soaked with 100 µL of electrolyte.

Electrodes using commercial Li_2S and Li_2S-CC as active material were prepared by manually grinding active material, Super C65 and PVdF. For Li_2S, the respective weight ratios were 50:40:10, while for Li_2S-CC, the weight ratio was 53:37:10, to keep the amount of active Li_2S similar across electrodes. NMP, and the resulting slurry cast over an aluminum current collector using the doctor blade method, and dried at 60 °C under normal pressure. Three-electrodes *Swagelok*-type T cells, with lithium metal as both counter and reference electrode, with a glass fiber separator soaked in 100 µL of either the "fresh" or "aged" electrolyte.

For capacity retention experiments of Li_2S-En based cathodes, cells were galvanostatically cycled in a Maccor S4000 battery tester at 20 °C. The cells were activated at a C/20 rate (1C = 1165 mAh g^{-1}) up to either 3 or 4V vs. Li/Li^+, followed by cycling at C/10 between 1.9 and 3.0 V vs. Li/Li^+. Electrochemical impedance spectroscopy was measured using a BioLogic VMP3 multi-channel potentiostat. For that, cells were cycled using the same procedures as mentioned above. However, after each discharge, the cell was allowed to rest at open-circuit for two hours prior to measuring impedance. Spectra were recorded between frequencies of 200 kHz and 100 mHz, using a 5 mV signal amplitude.

For Li_2S and Li_2S-CC, similar electrochemical tests were performed, where capacity retention was evaluated by galvanostatically cycling cells in a Maccor S4000 battery tester at 20 °C. Cells were also activated at a C/20 rate (1C = 1165 mAh g^{-1}), but always up to 4V vs. Li/Li^+, followed by cycling at C/10 between 1.9 and 3.0 V vs. Li/Li^+. EIS was measured using a BioLogic VMP3 multi-channel potentiostat, with cells cycled using the same procedures as mentioned above. However, after each discharge, the cell was allowed to rest at open-circuit for two hours prior to measuring impedance. Spectra were recorded between frequencies of 200 kHz and 100 mHz, using a 5 mV signal amplitude.

For the electrochemical stability window, electrodes composed of Super C65 and PVdF were prepared, where Super C65 and PVdF were ground in an 85:15 ratio, respectively, NMP added to prepare a slurry, and the resulting slurry cast over aluminum foil. Electrodes were also prepared using a nitrogen-rich carbon derived from EMImTCM, IoLiTec. In short, EMImTCM was placed in an alumina boat inside a horizontal tube furnace under argon flow, and the temperature was raised to 500 °C at a rate of 5 °C min^{-1}, and kept at that temperature for 5 hours. The resulting carbonized sample (N-Rich carbon) was composed of 62% carbon, 33% nitrogen, 2% hydrogen, and 3% oxygen (all values given as weight percentages), similar to the composition of the carbon coating in Li_2S-CC. The N-rich carbon was used to prepare electrodes as well, in which Super C-65, N-rich carbon, and PVdF were mixed in a 70:15:15 ratio, respectively, dispersed in NMP, and the resulting slurry cast over aluminium foil.

Anodic electrochemical stability was studied by cyclic voltammetry, where the potential was spanned from 3 to 4V vs. Li/Li^+. After cycling, the cell was disassembled inside a glove box, and the electrolyte recovered by centrifuging the glass fiber separators at 6000 rpm for 10 minutes. The recovered electrolytes were also analyzed via ATR-IR.

The following tables summarize the different systems tested and the abbreviation given to them:

Table 4.3.1. Naming convention for the set of experiments using crystalline lithium sulfide as active material

		Electrolyte	
		Fresh	Aged
Material	Li_2S	Li_2S_F	Li_2S_A
	Li_2S-CC	Li_2S-CC_F	Li_2S-CC_A

Table 4.3.2. Naming convention for the set of experiments using amorphous lithium sulfide as active material

		Activation cut-off	
		3V	4V
Electrolyt	Aged	Li_2S-En_3VA	Li_2S-En_4VA
	Fresh	Li_2S-En_3VF	Li_2S-En_4VF

4.3.2 Ageing of the electrolyte – impact on lithium sulfide electrochemistry

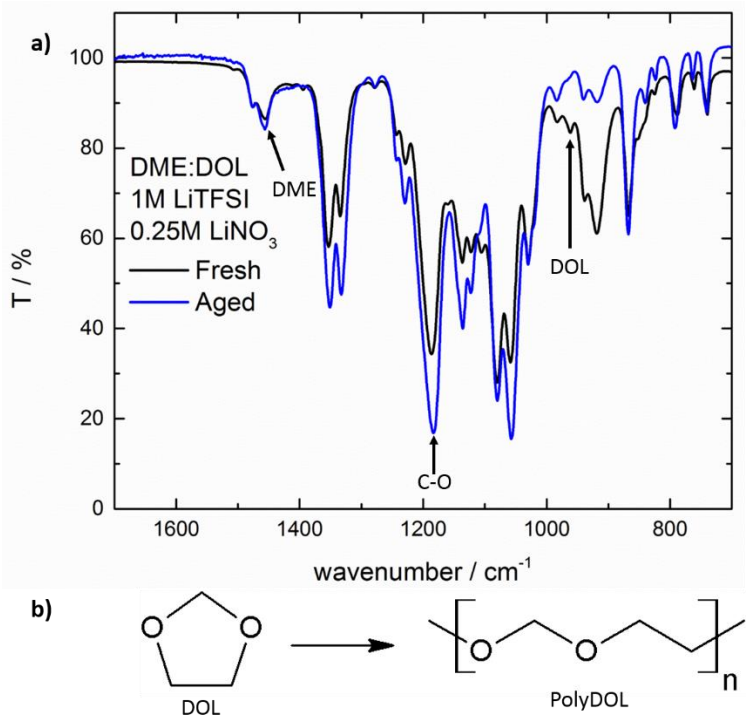

Figure 4.3.1. a) ATR-FTIR spectra of freshly prepared (black line) and aged (blue line) DME:DOL-based electrolyte. b) Scheme of the polymerization reaction of DOL (cf. also Figure 4.1.7).

Figure 4.3.1a shows the infrared spectrum of a freshly prepared electrolyte (fresh), as well as the infrared spectrum of the same electrolyte after storage for at least 12 months (aged). The assignments is done similarly to the spectra in Figure 4.1.6. Clearly, there are significant changes occurring during storage. The band at around 1450 cm^{-1} due to the $–CH_3$ deformation in DME[144] has a constant intensity before and after ageing, showing that DME is stable. The band at 960 cm^{-1} due to the ring-breathing mode of DOL[145] shows an appreciable decrease upon storage. DOL is known to be relatively unstable, being prone to ring-opening reactions (Figure 4.1.7). As shown in section 4.1, the two main ones are its polymerization and isomerization[147–149]. Isomerization of DOL leads to the formation of ethyl formate. However, no band corresponding to the vibration of the carbonyl group can be detected in the aged electrolyte, thus ruling out this option. On the other hand, polymerization of DOL has been extensively studied and known to happen when a cationic initiator is present[147,148,151], leading to the formation of

polydioxolane (polyDOL, Figure 4.3.1b), a poly-ether. The formation of polyDOL in the aged electrolyte is proven by the increase in the band at around 1190 cm^{-1}, which is caused by the vibrations of the C-O bonds in linear molecules[144]. Being a cyclic compound, C-O-C vibrations in DOL involve the whole ring and are thus heavily shifted[145]. The exact cause of this polymerization, in this case, is still unknown. Although DOL is known to be reactive, polymerization only happens in the presence of an appropriate initiator, usually one that can promote chain growth through a cationic mechanism. Analysis of the pure solvent mixture (1:1 DME:DOL) without addition of salt and stored under the same conditions for the same period of time shows no change in its spectrum, such that the culprit is likely the salts added to form the electrolyte ($LiNO_3$ and LiTFSI). Li^+ is known to coordinate the oxygen atoms in ether molecules[177], placing a partial positive charge on it. This weak initiating ability could explain the long storage times necessary to observe the polymerization appreciably.

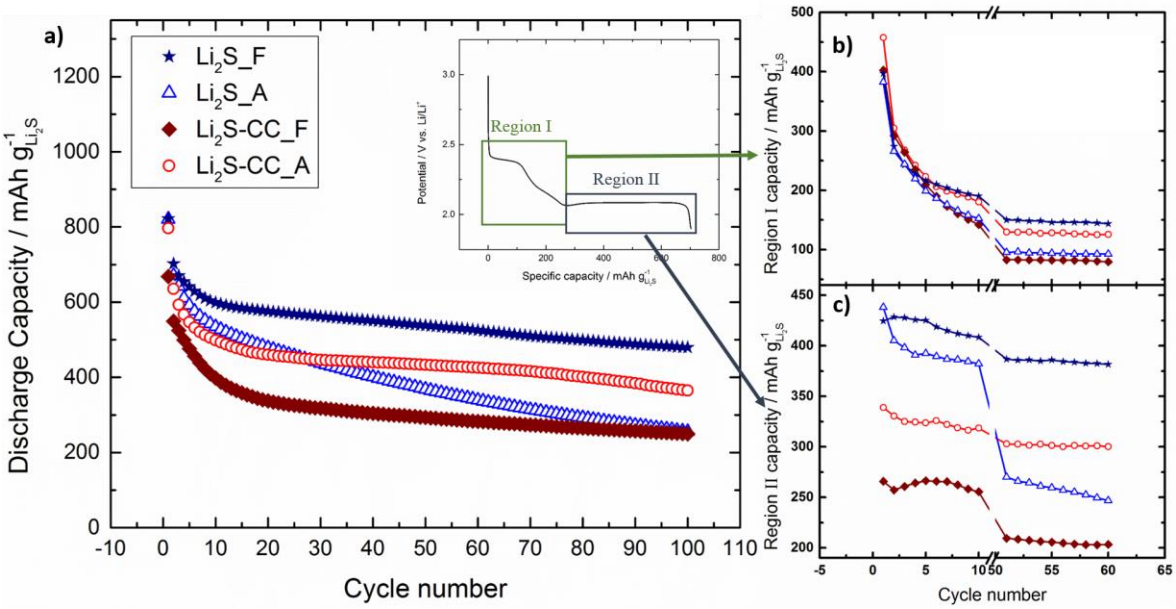

Figure 4.3.2. a) Capacity retention for cells using commercial Li_2S and carbon-coated Li_2S (Li_2S-CC). Inset: Typical discharge profile showing the two main discharge plateaus. Evolution of the capacity of b) region I and c) region II for selected cycles.

Figure 4.3.2a shows the capacity retention of the two active materials when using either the fresh (Li_2S_F and Li_2S-CC_F) or the aged (Li_2S_F and Li_2S-CC_F) electrolytes, from which it is evident that the electrolyte ageing had a big impact on the cell performance. One interesting and puzzling feature, though, is that the effect is not the same for the two active materials tested. In fact, the aged electrolyte worsened the performance of the commercial Li_2S compared to the fresh electrolyte, but enhanced that of the carbon-coated lithium sulfide, which showed a substantially improved capacity. This increased performance is certainly a noteworthy feature to be understood, as it could help in properly designing optimized active material/electrolyte combinations. The inset of Figure 4.3.2a shows the typical discharge curve of a Li_2S-based electrode after the initial activation leading to fully oxidized S. The first region (I) shows a voltage plateau (around 2.4 V vs. Li/Li^+) followed by a slopy region both associated with the reduction of molecular sulfur (S_8) to medium chain polysulfides (Li_2S_x, x = 4-6). After, a second region (II) characterized by a plateau at lower voltage (around 2.1 V vs. Li/Li^+) occurs, resulting

from the reduction of lithium polysulfides to form the final solid discharge products (Li_2S_x, $1 \leq x \leq 2$)[178].

Figure 4.3.2b and c show the evolution of the capacity arising in regions I and II, respectively, for a few selected cycles (1 to 10 and 50 to 60 cycles). The individual capacity of each region was calculated as shown in the inset of Figure 4.3.2a. As shown in Figure 4.3.2b, the capacity in the first region decrease sharply during the first 10 cycles to stabilize, however, after the 50th cycle. This indicates that, in all cells, less and less elemental sulfur (S_8) is formed in each charge, until a minimum is reached. In Figure 4.3.2c, the evolution of the capacity associated with the second region shows a considerably more peculiar behavior. In the Li_2S_F cell, the capacity is high and remains reasonably stable upon cycling. The Li_2S_A cell showed also high initial capacity, which rapidly faded within the first 50 cycles. Once more, the cells employing the carbon-coated lithium sulfide (Li_2S-CC) electrodes showed a different behavior. Firstly, it is clearly observed that the initial lower capacity of these cells with respect those employing commercial Li_2S mostly arised from region II where the solid discharge products are formed. However, while the Li_2S-CC_A cell delivered a stable capacity upon cycling, the Li_2S-CC_F cell showed a lower and faster decreasing capacity. It is now clear then that understanding the effect of the aged electrolyte on this voltage region is vital to a deeper comprehension of the sulfur electrochemistry.

As shown in Figure 4.3.1, the polymerization of DOL occurred upon prolonged storage of the electrolyte. The formation of polymeric chains led to the consumption of the low viscosity DOL resulting on increasing electrolyte's viscosity and, according to the available literature[27], lower sulfur utilization. In fact, decreasing the tetraethylene-glycol-dimethyl-ether (TEGDME) content in TEGDME:DOL-based electrolytes, resulted in a linear decrease of the sulfur utilization. Specifically, the electrolyte containing only TEGDME as solvent (high viscosity) showed a lower capacity in the second plateau

compared to electrolytes with high percentage of DOL (low viscosity)[154] due to the accumulation of solid products on the electrode's surface. High electrolyte viscosities reduce the diffusion of the polysulfides formed in the first discharge plateau away from the electrode, leading to their locally high concentration at the electrode surface. Upon disproportionation, the spontaneous precipitation of a rather thick layer of Li_2S onto the electrode occurs, which is not in electronic contact due to its poor electronic conductivity. Low electrolyte viscosities, on the other hand, allow low polysulfide concentrations such that the solid products are formed preferentially upon reduction (rather than disproportionation) over the conducting surface, leading to overall higher capacities.

However, the effect of the viscosity is not ubiquitous, or not the only reason for the observed differences. The Li_2S-CC_A cell, in fact, shows a higher capacity than the Li_2S-CC_F cell (Figure 4.3.2a), mainly due to the higher and more stable capacity delivered in region II (Figure 4.3.2c). Similar results have been already reported in literature[88]. The comparison of electrolytes based on DME:DOL, TEGDME:DOL, and poly(ethylene glycol) dimethyl ether (PEGDME):DOL, which viscosity increases in the aforementioned order, showed an increase in capacity of up to 2.5 times for the PEGDME:DOL based electrolyte compared to the DME:DOL based one. In order to better clarify the reason for this unconventional behavior of Li_2S-CC, the EIS response of all cells in the discharged states upon cycling was measured (see Figure 4.3.3).

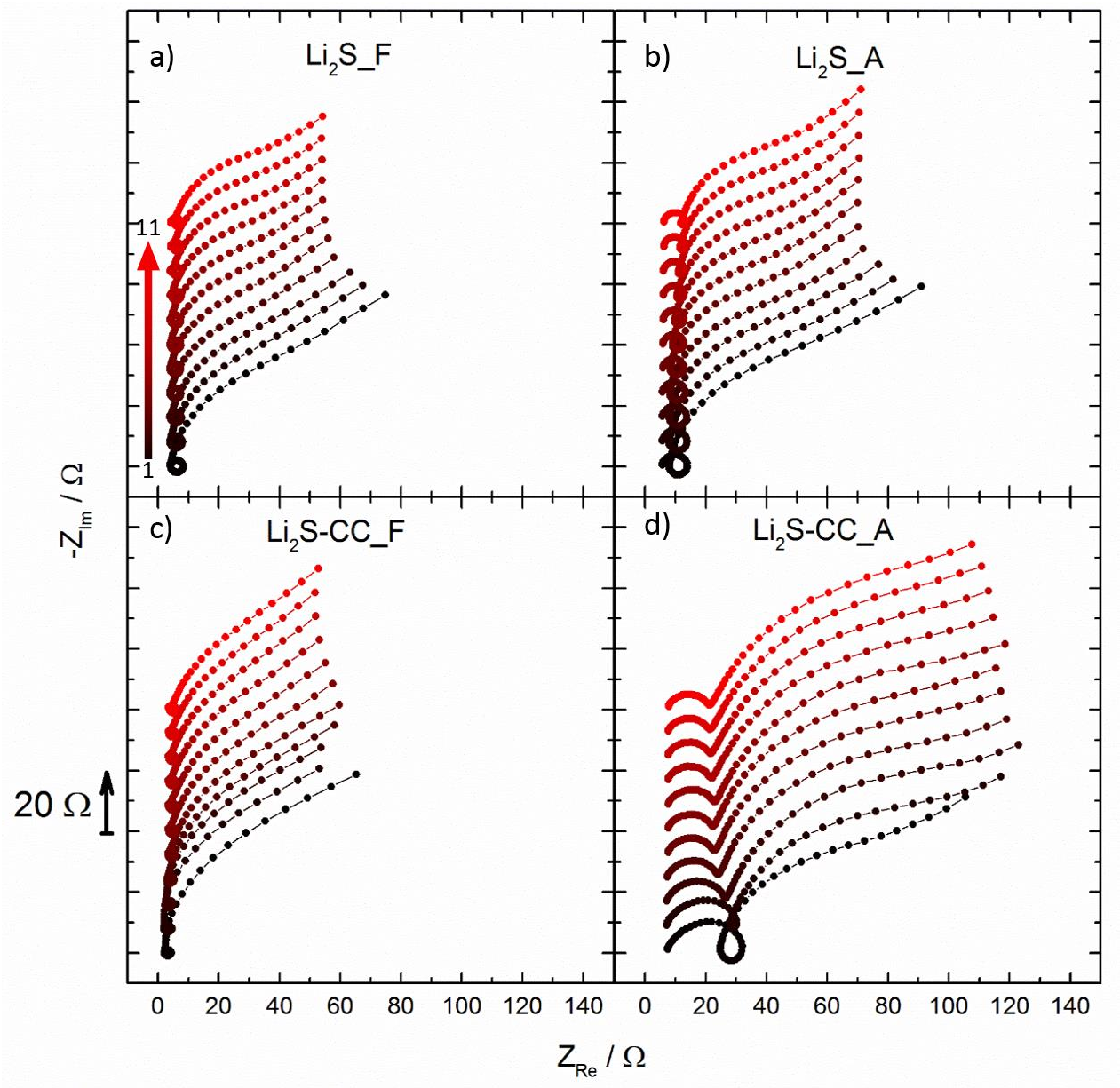

Figure 4.3.3. Evolution of the electrochemical impedance spectra from the first to the eleventh cycle of a) Li_2S-F, b) Li_2S_A, c) Li_2S-CC_F, and d) Li_2S-CC_A. The baseline of the spectra are shifted upward for clarity. All spectra were taken on 3-electrode cells in the discharged state.

The spectra of Li_2S_F and Li_2S-CC_F (Figure 4.3.3a and c, respectively) show a small high frequency (HF) semicircle evolving into a pseudo-inductive loop, followed by the beginning of a large, partially depressed, semicircle at low frequencies (LF). The pseudo-inductive loop has been shown to be related to intermediate species, i.e., polysulfides, adsorbed on the electrode's surface[129,130,179,180]. The depressed LF semicircle is typical of charge-transfer reactions, and corresponds to the reversible conversion of

polysulfides to solid products. For Li_2S_A and Li_2S-CC_A (Figure 4.3.3b and d, respectively) some differences are observed, the most relevant being the large HF semicircle before the pseudo-inductive loop. This is more evident for Li_2S-CC_A (Figure 4.3.3d) than Li_2S_A (Figure 4.3.3b). Even more interesting is the disappearance of the loop in the spectra of the former cell after a couple of cycles. The exact nature of this disappearance is unclear. In fact, in many of the reported impedance spectra of Li-S systems no inductive loop can be observed[84,181–184]. In a previous report of our group, the inductive loops during the cycling of sulfur-based cathodes were also observed[155].

As previously mentioned, the main difference between the impedance spectra of the cells with fresh and aged electrolyte in Figure 4.3.3, beside the disappearance of the inductive loop in Figure 4.3.3d, is the size of the HF semicircle, which may be associated to presence of a surface layer on the electrode. The formation of a passivation layer is not unexpected. In fact, during the activation step the cathode is charged up to 4 V vs. Li/Li^+, while the electrolyte is only stable up to 3.6 V vs. Li/Li^+ [118]. To test the effect of activation potential on the impedance spectra of lithium sulfide-based cathodes, electrodes using Li_2S-En as active material were studied.

4.3.3 Impact of activation potential on the electrochemistry of lithium sulfide

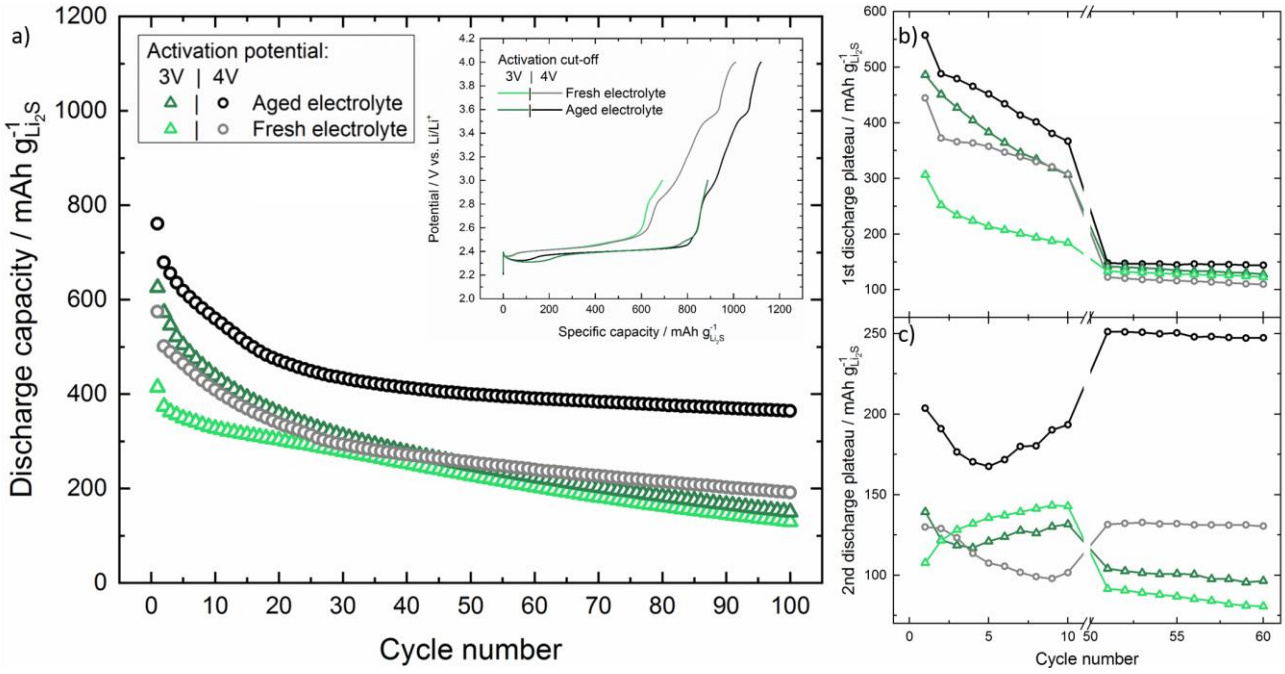

Figure 4.3.4. a) Capacity retention for cells using amorphous Li_2S-En cathodes with different activation potential cut-offs. Inset: activation step for the four systems investigated. Evolution of the capacity of the b) region I and c) region II for selected cycles.

To test the effects of the passivation layer on the cycling of the electrode, the electrolytes were tested with another active material, namely Li_2S-En. This material, which is not carbon coated and is the precursor of the Li_2S-CC, is different from the commercial one as is composed of mostly amorphous particles. As it can be seen in the inset of Figure 4.3.4a, this leads to a decrease in the average activation potential of lithium sulfide. This allows us, by varying the potential cut-off during activation, to study the effect of the passivation layer more in-depth.

Figure 4.3.4a shows the effect of different activation potential cut-offs and electrolyte ageing on the capacity retention of the cells using Li_2S-En as cathode material. The cells show an interesting response, with Li_2S-En_4VA delivering substantially higher capacity in comparison to any of the other systems (fresh electrolyte and/or activated only up to 3 V vs. Li/Li^+). The capacities are, however, much smaller than those in Figure 4.3.2a. As previously done for Li_2S and Li_2S-CC, the capacity arising

from different potential regions of the discharge curve is analyzed for selected cycles (see Figure 4.3.4b and c for region I and II capacities, respectively). The same trends as in Figure 4.3.2 can be observed, with the capacity of the first plateau rapidly decreasing in the first few cycles and, afterwards, reaching a stable value, which is similar for all studied electrolytes. Again, the differences can be mostly attributed to the capacity of the second plateau, similar to the case of crystalline lithium sulfide. Of note, the capacity of the second plateau increases for the cells activated up to 4V vs. Li/Li^+, showing much higher capacity in the 50th to 60th cycle region than cells activated only up to 3V.

It should be noted that one important difference between the systems in Figure 4.3.2 and Figure 4.3.4 is the binder used. For the crystalline lithium sulfide, the binder is PVdF, a polar polymer. Differently, the electrode based on amorphous lithium sulfide, given its incompatibility with NMP, are bound using polyisobutylene, a non-polar polyolefin which can be used in toluene-based slurries. As previously mentioned, the polarity of the electrode have a huge impact on the formation of the solid products during discharge[73]. The lower capacities of Figure 4.3.4a, with respect to Figure 4.3.2a, can likely be attributed to the lower polarity of the electrode caused by the different binder. In fact, while the capacities of the first plateau are comparable, for the second plateau, they are much lower in case of the non-polar binder. Interestingly, this decrease is more pronounced for Li_2S-En_3VA and Li_2S-En_3VF, since they do not undergo the passivation layer formation. Li_2S-En_4VF shows an increase in the capacity after 50 cycles, showing that the formation of the passivation layer leads to a slight improvement of the lithium sulfide formation. The passivation layer formed by decomposing the electrolyte is known to be composed of several polar components[142,152], which help to increase the capacity of the second plateau. This improvement, however, is much bigger for Li_2S-En_4VA, as seen by the larger capacity (and capacity increase) of the second

plateau. This is a strong hint that the passivation layer formed in the aged electrolyte is more effective for reversibly forming lithium sulfide during discharge.

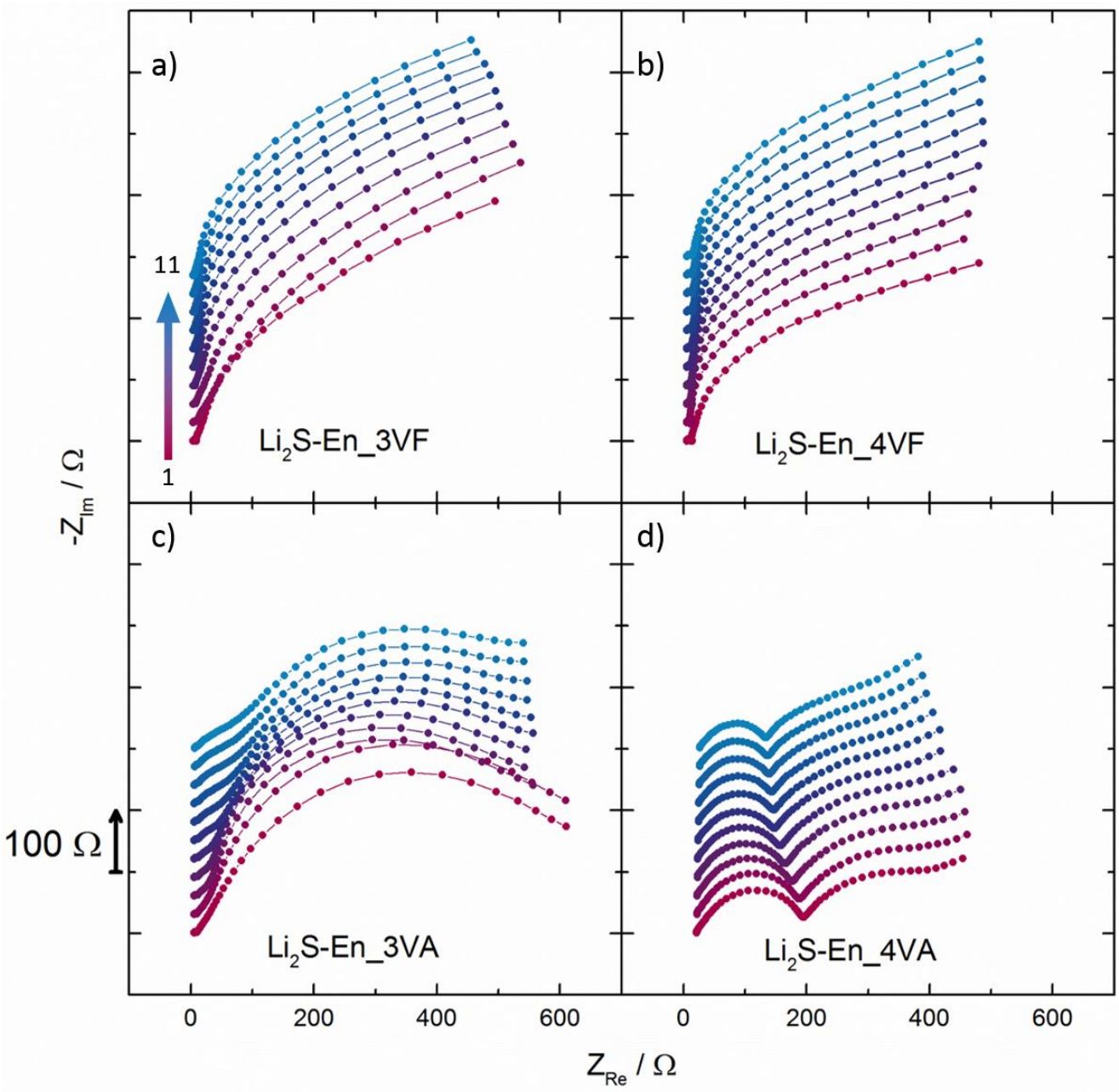

Figure 4.3.5. Electrochemical impedance spectroscopy from first to eleventh cycle of amorphous Li_2S (Li_2S-En) cells. A) Li_2S-En_3VF, b) Li_2S-En_4VF, c) Li_2S-En_3VA, d) Li_2S-En_4VA.

Figure 4.3.5 shows the EIS spectra of cathodes with Li_2S-En in the discharge state. The spectra of Li_2S-En_3VF and Li_2S-En_4VF (Figure 4.3.5a and b) as well as of Li_2S-En_3VA (Figure 4.3.5c) are very similar, being dominated by a large semicircle. The spectra of Li_2S-En_4VA (Figure 4.3.5d) shows a different shape instead, with two well separated semicircles at high and medium to low frequencies. As mentioned in the discussion of Figure 4.3.3, the HF semicircle can be associated with a passivation layer

formed on the electrode. Interestingly though, the LF semicircle, related to the charge-transfer, is noticeably smaller for Li_2S-En_4VA, both compared Li_2S-En_3VF and Li_2S-En_3VA, which presumably have no passivation layer formed, and to that of Li_2S-En_4VF, where the passivation layer is assumed to be very thin, as observed by the small HF semicircle. This confirms, once more, the previous results reported in Figure 4.3.4, and suggest the beneficial nature of said layer.

Figure 4.3.4 and Figure 4.3.5 partially explain the results observed in Figure 4.3.2c, as far as the increase in capacity for Li_2S-CC with aged electrolyte is concerned. As previously explained, the carbon coating of the particles is non-polar, hindering the efficient formation of lithium sulfide. However, during the first activation, a passivation layer is formed upon decomposition of the electrolyte. The passivation layer formed in the aged electrolyte seems to be highly polar and it promotes the lithium sulfide formation during discharge, which greatly improves the capacity of the second plateau. On the contrary, the passivation layer formed in the fresh electrolyte, seems to be less effective in promoting the lithium sulfide formation. One question that remains, though, is why does this process only happens on the carbon-coated material, and not on the commercial Li_2S.

4.3.4 Passivation layer formation on the different electrolytes

It is clear from the results in section 4.3.3 that activating the cell containing the aged electrolyte up to 4V vs. Li/Li$^+$ leads to a thicker passivation layer in comparison to other cells. This is clear evidence that, indeed, the bigger HF semicircles in Figure 4.3.3b and d are caused by the aged electrolyte. Such change in the surface properties of the electrodes could reasonably affect the adsorption of the polysulfides, as evidenced, indeed, by the disappearance of the pseudo-inductive loop, and also the lithium sulfide precipitation. Since, once again, the main difference between Li_2S-CC_A and Li_2S_A is the presence of carbon-coating in the former, it is reasonable to assume that the passivation layer is able to grow thicker over the carbon-coating.

To test the effect of the carbon coating on the electrode passivation, the anodic stability window of both electrolytes were tested with two different electrodes, one which is similar to the electrode of Li_2S, and one which is similar to the electrode of Li_2S-CC, but both without any Li_2S.

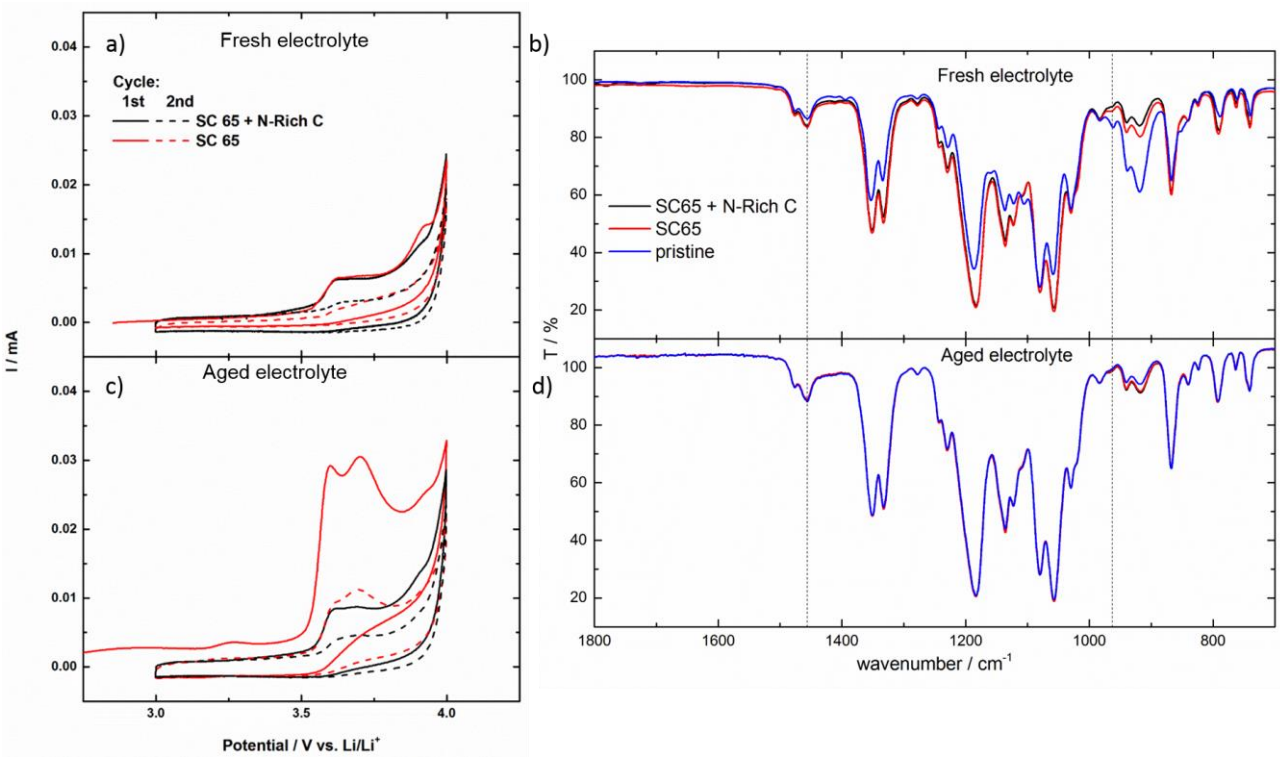

Figure 4.3.6. Electrochemical stability window determined by cyclic voltammograms of a) fresh electrolyte and b) the IR of the electrolyte extracted from the cells using two different electrode materials. c) Cyclic voltammograms

under similar conditions using aged electrolyte and d) IR of the electrolytes extracted from the different cells. The spectra of the uncycled electrolyte is also shown for comparison

Figure 4.3.6 shows the anodic stability limit measurements of the electrolytes performed using the two types of carbon electrodes, containing either the conducting carbon only (labeled as **SC 65**) or the mixture of conductive carbon and nitrogen-rich carbon (labelled as **SC 65 + N-rich C**), the latter mimicking the carbon-coating of the Li_2S-CC particles. As seen in Figure 4.3.6, the two electrolytes showed oxidation peaks above 3.5-3.6 V vs. Li/Li^+. For the fresh electrolyte, comparable peaks were observed with both carbon electrodes in the first cycle. The same occurred in the second cycle, where almost no oxidation current was seen indicating that the carbon electrodes underwent a passivation process. However, the recorded peak current was substantially larger with the aged electrolyte, especially for the electrode solely composed by SuperC 65 and binder.

The infrared spectra of the electrolytes after cycling (Figure 4.3.6b) show the disappearance of the DOL band, indicating its consumption to form the passivation layer on the carbon electrodes. The aged electrolyte (Figure 4.3.6d) contains less DOL than the fresh one even before cycling, due to the age-induced polymerization. However, there is only a little, if any, change in the spectra of the recovered electrolyte in comparison to the pristine aged electrolyte. Still, the cyclic voltammograms show pretty clearly that the oxidation current for the electrode using only Super C65 is much larger than for that containing also the N-rich carbon. This is a strong indication that the formation of a passivation layer still occurred, but at a much reduced extent on the electrode containing the N-rich carbon. Though the exact mechanism is not clear yet, it can be proposed that the N-rich carbon layer facilitates the anchoring of the PolyDOL from the aged electrolyte, resulting in the formation of a protective layer only on the carbon-coated Li_2S, which leads to the improved performance of such electrodes in the aged electrolyte.

In summary, the effect of electrolyte ageing on the electrochemistry of Li_2S-based cathode was studied. It was determined that DOL tends to spontaneously polymerize upon aging in the presence of Li^+ ions. The presence of polyDOL in the electrolyte has an appreciable and unexpected impact on the performance of Li_2S electrodes. For pure Li_2S electrodes, the overall impact was found to be negative, mostly due to the increased viscosity of the electrolyte causing the formation of a thick sulfide layer by polysulfide disproportionation, which is not in good electronic contact with the electrode. Differently, the aged electrolyte showed improved performance with the carbon-coated Li_2S electrodes when compared with the fresh electrolyte. The obtained results suggest the anchoring of the polymer chains over the carbon-coating, leading to a more hydrophilic electrode which favors the lithium sulfide formation during discharge.

Additionally, analyzing how the aged electrolyte impacts the different cells, allowed for a deeper understanding of the sulfur electrochemistry. Specifically, it was shown that the carbon coating used is largely hydrophobic and hampers lithium sulfide formation, as evidenced by the smaller capacity in Region II of the discharge profile. PolyDOL can form a stable, hydrophilic passivation layer over the carbon coating, improving the lithium sulfide formation during discharge, and leading to bigger capacities in the same region. This passivation layer, however, seems to also affect the polysulfide absorption, seen as the decrease of the inductance loop over cycle in the cells where this layer is thicker.

5 Conclusions

In this work, several degradation reactions involving the electrolyte are investigated, and their influence on the electrochemistry of lithium-sulfur batteries carefully addressed.

Overall, the dioxolane solvent was found to be the electrolyte component most susceptible to degradation, as it is prone to different types of ring-opening reactions. These reactions are not always detrimental. Dioxolane was found to form stable passivation layers both on the lithium anode and on the lithium sulfide cathode, preventing the further degradation of the electrolyte. Specifically, the polymerization here was promoted by dissolved oxygen, which also promotes isomerization, a reaction much more detrimental to the sulfur cathode. To exploit this polymerization, an additive needs to be found which can selectively trigger polymerization but not isomerization. The effect of high activation potentials on lithium sulfide anodes was also tested, and from the electrochemical stability window tests, it seems that dioxolane is successful in forming a passivation layer with minimal to no isomerization under the conditions needed for lithium sulfide activation. Much more interesting, however, were the results regarding the self-polymerization of dioxolane in the electrolyte stored over prolonged periods of time. The poly-dioxolane chains can apparently be anchored over the electrode, leading to improved interactions with the lithium sulfides/polysulfides as well. All these potential improvements were hampered, however, by the depletion of the dioxolane. In fact, dioxolane also plays the role of low-viscosity solvent, and its consumption means that the properties of the electrolyte change in the real cell. This effect has to be accounted for when designing new electrolytes, either by replacing dioxolane by a more stable solvent, or by using dioxolane in conjunction with another low-viscosity electrolyte.

Finally, an arguably more interesting aspect in the present work is the rationalizations of the changes in cycling behavior of the sulfur electrodes. The

isomerization products of dioxolane lead to an improved liquid-phase reaction, which seems to improve the cell capacity, albeit irreversibly. Finding an additive which could increase the liquid-liquid polysulfide reduction without irreversibly reacting with it could open new pathways to improve sulfur capacity. The effect of poly-dioxolane on the cathode also shows some interesting results. Firstly, the electrochemical impedance spectra show that polysulfide adsorption over the surface precedes the reduction to form lithium sulfide, which is an aspect of the sulfur reduction mechanism that is rarely, if ever, discussed. It was also observed that the capacity of the two plateau regions in the voltage profile of sulfur reduction are independent from one another. If the decrease in capacity was caused by the loss of active material, it would be reasonable to expect that both plateaus would lose capacity at the same time, and at similar rates. In the case of commercial lithium sulfide with freshly prepared electrolyte, for example, the first plateau capacity decreases while the second remains constant. Even more striking, the first plateau capacity decreases similarly in all systems, a strong evidence that the same amount of sulfur is present at the electrode in all of them, at any given cycle. The reason for this puzzling behavior is not known. It can be speculated that promoting good electrode kinetics is more important than polysulfide retention, as previously thought. This is even harder to analyze seeing how literature data rarely report the evolution of each plateau independently, such that understanding the effect of different electrode/electrolyte modifications on each part of the sulfur reduction becomes harder.

6 Bibliographical references

(1) Xu, B.; Qian, D.; Wang, Z.; Meng, Y. S. Recent Progress in Cathode Materials Research for Advanced Lithium Ion Batteries. *Mater. Sci. Eng. R Reports* **2012**, *73* (5–6), 51–65.

(2) Scrosati, B.; Garche, J. Lithium Batteries: Status, Prospects and Future. *J. Power Sources* **2010**, *195* (9), 2419–2430.

(3) Etacheri, V.; Marom, R.; Elazari, R.; Salitra, G.; Aurbach, D. Challenges in the Development of Advanced Li-Ion Batteries: A Review. *Energy Environ. Sci.* **2011**, *4* (9), 3243.

(4) Amatucci, G. G. CoO[Sub 2], The End Member of the Li[Sub x]CoO[Sub 2] Solid Solution. *J. Electrochem. Soc.* **1996**, *143* (3), 1114.

(5) Ozawa, K. Lithium-Ion Rechargeable Batteries with LiCoO2 and Carbon Electrodes: The LiCoO2/C System. *Solid State Ionics* **1994**, *69* (3–4), 212–221.

(6) Vaalma, C.; Buchholz, D.; Weil, M.; Passerini, S. A Cost and Resource Analysis of Sodium-Ion Batteries. *Nat. Rev. Mater.* **2018**, *3*, 18013.

(7) Guyomard, D.; Tarascon, J. M. Li Metal-Free Rechargeable LiMn[Sub 2]O[Sub 4]/Carbon Cells: Their Understanding and Optimization. *J. Electrochem. Soc.* **1992**, *139* (4), 937.

(8) Tarascon, J. M.; McKinnon, W. R.; Coowar, F.; Bowmer, T. N.; Amatucci, G.; Guyomard, D. Synthesis Conditions and Oxygen Stoichiometry Effects on Li Insertion into the Spinel LiMn[Sub 2]O[Sub 4]. *J. Electrochem. Soc.* **1994**, *141* (6), 1421.

(9) Verma, P.; Maire, P.; Novák, P. A Review of the Features and Analyses of the Solid Electrolyte Interphase in Li-Ion Batteries. *Electrochim. Acta* **2010**, *55* (22), 6332–6341.

(10) Edström, K.; Herstedt, M.; Abraham, D. P. A New Look at the Solid Electrolyte Interphase on Graphite Anodes in Li-Ion Batteries. *J. Power Sources* **2006**, *153* (2), 380–384.

(11) Nie, M.; Chalasani, D.; Abraham, D. P.; Chen, Y.; Bose, A.; Lucht, B. L. Lithium Ion Battery Graphite Solid Electrolyte Interphase Revealed by Microscopy and Spectroscopy. *J. Phys. Chem. C* **2013**, *117* (3), 1257–1267.

(12) Lu, M.; Cheng, H.; Yang, Y. A Comparison of Solid Electrolyte Interphase (SEI) on the Artificial Graphite Anode of the Aged and Cycled Commercial Lithium Ion Cells. *Electrochim. Acta* **2008**, *53* (9), 3539–3546.

(13) Vetter, J.; Novák, P.; Wagner, M. R.; Veit, C.; Möller, K. C.; Besenhard, J. O.; Winter, M.; Wohlfahrt-Mehrens, M.; Vogler, C.; Hammouche, A. Ageing Mechanisms in Lithium-Ion Batteries. *J. Power Sources* **2005**, *147* (1–2), 269–281.

(14) Möller, K. C.; Hodal, T.; Appel, W. K.; Winter, M.; Besenhard, J. O. Fluorinated Organic Solvents in Electrolytes for Lithium Ion Cells. *J. Power Sources* **2001**, *97–98*, 595–597.

(15) Smart, M. C.; Ratnakumar, B. V.; Ryan-Mowrey, V. S.; Surampudi, S.; Prakash, G. K. S.; Hu, J.; Cheung, I. Improved Performance of Lithium-Ion Cells with the Use of Fluorinated Carbonate-Based Electrolytes. *J. Power Sources* **2003**, *119–121*, 359–367.

(16) Ohzuku, T.; Makimura, Y. Layered Lithium Insertion Material of LiNi1/2Mn1/2O2: A Possible Alternative to LiCoO2 for Advanced

Lithium-Ion Batteries. *Chem. Lett.* **2001**, *2*, 744–745.

(17) Yabuuchi, N.; Kumar, S.; Li, H. H.; Kim, Y.-T.; Shao-Horn, Y. Changes in the Crystal Structure and Electrochemical Properties of Li[Sub x]Ni[Sub 0.5]Mn[Sub 0.5]O[Sub 2] during Electrochemical Cycling to High Voltages. *J. Electrochem. Soc.* **2007**, *154* (6), A566.

(18) Yoon, W.-S.; Paik, Y.; Yang, X.-Q.; Balasubramanian, M.; McBreen, J.; Grey, C. P. Investigation of the Local Structure of the LiNi[Sub 0.5]Mn[Sub 0.5]O[Sub 2] Cathode Material during Electrochemical Cycling by X-Ray Absorption and NMR Spectroscopy. *Electrochem. Solid-State Lett.* **2002**, *5* (11), A263.

(19) Abdel-Ghany, A.; Zaghib, K.; Gendron, F.; Mauger, A.; Julien, C. M. Structural, Magnetic and Electrochemical Properties of LiNi0.5Mn0.5O2as Positive Electrode for Li-Ion Batteries. *Electrochim. Acta* **2007**, *52* (12), 4092–4100.

(20) Yoon, W. S.; Grey, C. P.; Balasubramanian, M.; Yang, X. Q.; McBreen, J. In Situ X-Ray Absorption Spectroscopic Study on LiNi0.5Mn 0.5O2 Cathode Material during Electrochemical Cycling. *Chem. Mater.* **2003**, *15* (16), 3161–3169.

(21) Kang, K. Electrodes with High Power and High Capacity for Rechargeable Lithium Batteries. *Science (80-.).* **2006**, *311* (5763), 977–980.

(22) Ohzuku, T.; Makimura, Y. Layered Lithium Insertion Material of LiCo 1/3 Ni 1/3 Mn 1/3 O 2 for Lithium-Ion Batteries. *Chem. Lett.* **2001**, *30* (7), 642–643.

(23) Li, Z.; Chernova, N. A.; Roppolo, M.; Upreti, S.; Petersburg, C.; Alamgir, F. M.; Whittingham, M. S. Comparative Study of the Capacity and Rate Capability of LiNiyMnyCo1–2yO2 (y = 0.5, 0.45, 0.4, 0.33). *J. Electrochem. Soc.* **2011**, *158* (5), A516.

(24) Kim, J.-M.; Chung, H.-T. The First Cycle Characteristics of Li[Ni1/3Co1/3Mn1/3]O2 Charged up to 4.7 V. *Electrochim. Acta* **2004**, *49* (6), 937–944.

(25) Manthiram, A.; Choi, J. Chemical and Structural Instabilities of Lithium Ion Battery Cathodes. *J. Power Sources* **2006**, *159* (1), 249–253.

(26) Choi, J.; Manthiram, A. Role of Chemical and Structural Stabilities on the Electrochemical Properties of Layered LiNi[Sub 1⁄3]Mn[Sub 1⁄3]Co[Sub 1⁄3]O[Sub 2] Cathodes. *J. Electrochem. Soc.* **2005**, *152* (9), A1714.

(27) Rozier, P.; Tarascon, J. M. Review—Li-Rich Layered Oxide Cathodes for Next-Generation Li-Ion Batteries: Chances and Challenges. *J. Electrochem. Soc.* **2015**, *162* (14), A2490–A2499.

(28) Kalyani, P.; Chitra, S.; Mohan, T.; Gopukumar, S. Lithium Metal Rechargeable Cells Using Li2MnO3 as the Positive Electrode. *J. Power Sources* **1999**, *80* (1–2), 103–106.

(29) David, W. I. F.; Thackeray, M. M.; Bruce, P. G.; Goodenough, J. B. Lithium Insertion into ß-MnO2 and the Rutile-Spinel Transformation. *Mater. Res. Bull.* **1984**, *19* (1), 99–106.

(30) Thackeray, M. M.; David, W. I. F.; Bruce, P. G.; Goodenough, J. B. Lithium Insertion into Manganese Spinels. *Mater. Res. Bull.* **1983**, *18* (4), 461–472.

(31) Xia, Y. Capacity Fading on Cycling of 4 V Li⁄LiMn[Sub 2]O[Sub 4] Cells. *J. Electrochem. Soc.* **1997**, *144* (8), 2593.

(32) Xiao, J.; Chen, X.; Sushko, P. V.; Sushko, M. L.;

Kovarik, L.; Feng, J.; Deng, Z.; Zheng, J.; Graff, G. L.; Nie, Z.; et al. High-Performance LiNi0.5Mn1.5O4Spinel Controlled by Mn3+concentration and Site Disorder. *Adv. Mater.* **2012**, *24* (16), 2109–2116.

(33) Oh, S. H.; Jeon, S. H.; Cho, W. Il; Kim, C. S.; Cho, B. W. Synthesis and Characterization of the Metal-Doped High-Voltage Spinel LiNi0.5Mn1.5O4by Mechanochemical Process. *J. Alloys Compd.* **2008**, *452* (2), 389–396.

(34) Zhang, N.; Yang, T.; Lang, Y.; Sun, K. A Facile Method to Prepare Hybrid LiNi0.5Mn1.5O4/C with Enhanced Rate Performance. *J. Alloys Compd.* **2011**, *509* (9), 3783–3786.

(35) Molenda, J.; Marzec, J.; Świerczek, K.; Ojczyk, W.; Ziemnicki, M.; Molenda, M.; Drozdek, M.; Dziembaj, R. The Effect of 3d Substitutions in the Manganese Sublattice on the Charge Transport Mechanism and Electrochemical Properties of Manganese Spinel. *Solid State Ionics* **2004**, *171* (3–4), 215–227.

(36) Cho, H.-M.; Chen, M. V.; MacRae, A. C.; Meng, Y. S. Effect of Surface Modification on Nano-Structured LiNi 0.5 Mn 1.5 O 4 Spinel Materials. *ACS Appl. Mater. Interfaces* **2015**, *7* (30), 16231–16239.

(37) Lu, J.; Lee, K. S. Spinel Cathodes for Advanced Lithium Ion Batteries: A Review of Challenges and Recent Progress. *Mater. Technol.* **2016**, *31* (11), 628–641.

(38) Padhi, A. K. Effect of Structure on the Fe[Sup 3+]/Fe[Sup 2+] Redox Couple in Iron Phosphates. *J. Electrochem. Soc.* **1997**, *144* (5), 1609.

(39) Padhi, A. K. Phospho-Olivines as Positive-Electrode Materials for Rechargeable Lithium Batteries. *J. Electrochem. Soc.* **1997**, *144* (4), 1188.

(40) Morgan, D.; Van der Ven, A.; Ceder, G. Li Conductivity in Li[Sub x]MPO[Sub 4] (M = Mn, Fe, Co, Ni) Olivine Materials. *Electrochem. Solid-State Lett.* **2004**, *7* (2), A30.

(41) Fisher, C. A. J.; Hart Prieto, V. M.; Islam, M. S. Lithium Battery Materials Li M PO 4 (M = Mn, Fe, Co, and Ni): Insights into Defect Association, Transport Mechanisms, and Doping Behavior. *Chem. Mater.* **2008**, *20* (18), 5907–5915.

(42) Delmas, C.; Maccario, M.; Croguennec, L.; Le Cras, F.; Weill, F. Lithium Deintercalation in LiFePO4 Nanoparticles via a Domino-Cascade Model. *Nat. Mater.* **2008**, *7* (8), 665–671.

(43) Laffont, L.; Delacourt, C.; Gibot, P.; Wu, M. Y.; Kooyman, P.; Masquelier, C.; Tarascon, J. M. Study of the LiFePO 4 /FePO 4 Two-Phase System by High-Resolution Electron Energy Loss Spectroscopy. *Chem. Mater.* **2006**, *18* (23), 5520–5529.

(44) Huang, H.; Yin, S.-C.; Nazar, L. F. Approaching Theoretical Capacity of LiFePO[Sub 4] at Room Temperature at High Rates. *Electrochem. Solid-State Lett.* **2001**, *4* (10), A170.

(45) Jung, K.-N.; Kim, J.; Yamauchi, Y.; Park, M.-S.; Lee, J.-W.; Kim, J. H. Rechargeable Lithium–air Batteries: A Perspective on the Development of Oxygen Electrodes. *J. Mater. Chem. A* **2016**, *4* (37), 14050–14068.

(46) Ulam, D.; Herbert, J. USPat. US3043896, 1962.

(47) Cuisinier, M.; Cabelguen, P. E.; Evers, S.; He, G.; Kolbeck, M.; Garsuch, A.; Bolin, T.; Balasubramanian, M.; Nazar, L. F. Sulfur Speciation in Li-S Batteries Determined by Operando X-Ray Absorption Spectroscopy. *J. Phys. Chem. Lett.* **2013**, *4* (19), 3227–3232.

(48) Cuisinier, M.; Hart, C.; Balasubramanian, M.; Garsuch, A.; Nazar, L. F. Radical or Not Radical: Revisiting Lithium-Sulfur Electrochemistry in Nonaqueous Electrolytes. *Adv. Energy Mater.* **2015**, *5* (16), 1–6.

(49) Wang, Q.; Zheng, J.; Walter, E.; Pan, H.; Lv, D.; Zuo, P.; Chen, H.; Deng, Z. D.; Liaw, B. Y.; Yu, X.; et al. Direct Observation of Sulfur Radicals as Reaction Media in Lithium Sulfur Batteries. *J. Electrochem. Soc.* **2015**, *162* (3), A474–A478.

(50) Kumaresan, K.; Mikhaylik, Y.; White, R. E. A Mathematical Model for a Lithium–Sulfur Cell. *J. Electrochem. Soc.* **2008**, *155* (8), A576.

(51) Huggins, R. A. The Relation between the Gibbs Phase Rule and Reference Electrodes. *Ionics (Kiel).* **1998**, *4* (1–2), 129–140.

(52) Barchasz, C.; Molton, F.; Duboc, C.; Leprêtre, J. C.; Patoux, S.; Alloin, F. Lithium/Sulfur Cell Discharge Mechanism: An Original Approach for Intermediate Species Identification. *Anal. Chem.* **2012**, *84* (9), 3973–3980.

(53) Huff, L. A.; Rapp, J. L.; Baughman, J. A.; Rinaldi, P. L.; Gewirth, A. A. Identification of Lithium-Sulfur Battery Discharge Products Through6Li And33S Solid-State MAS And7Li Solution NMR Spectroscopy. *Surf. Sci.* **2015**, *631*, 295–300.

(54) Bresser, D.; Passerini, S.; Scrosati, B. Recent Progress and Remaining Challenges in Sulfur-Based Lithium Secondary Batteries – a Review. *Chem. Commun.* **2013**, *49* (90), 10545.

(55) Jayaprakash, N.; Shen, J.; Moganty, S. S.; Corona, A.; Archer, L. A. Porous Hollow Carbon@Sulfur Composites for High-Power Lithium-Sulfur Batteries. *Angew. Chemie Int. Ed.* **2011**, *50* (26), 5904–5908.

(56) Liang, X.; Wen, Z.; Liu, Y.; Zhang, H.; Huang, L.; Jin, J. Highly Dispersed Sulfur in Ordered Mesoporous Carbon Sphere as a Composite Cathode for Rechargeable Polymer Li/S Battery. *J. Power Sources* **2011**, *196* (7), 3655–3658.

(57) Li, X.; Cao, Y.; Qi, W.; Saraf, L. V.; Xiao, J.; Nie, Z.; Mietek, J.; Zhang, J.-G.; Schwenzer, B.; Liu, J. Optimization of Mesoporous Carbon Structures for Lithium–sulfur Battery Applications. *J. Mater. Chem.* **2011**, *21* (41), 16603.

(58) Chen, S.-R.; Zhai, Y.-P.; Xu, G.-L.; Jiang, Y.-X.; Zhao, D.-Y.; Li, J.-T.; Huang, L.; Sun, S.-G. Ordered Mesoporous Carbon/Sulfur Nanocomposite of High Performances as Cathode for Lithium–sulfur Battery. *Electrochim. Acta* **2011**, *56* (26), 9549–9555.

(59) Xin, S.; Gu, L.; Zhao, N.-H.; Yin, Y.-X.; Zhou, L.-J.; Guo, Y.-G.; Wan, L.-J. Smaller Sulfur Molecules Promise Better Lithium–Sulfur Batteries. *J. Am. Chem. Soc.* **2012**, *134* (45), 18510–18513.

(60) Ji, X.; Lee, K. T.; Nazar, L. F. A Highly Ordered Nanostructured Carbon–sulphur Cathode for Lithium–sulphur Batteries. *Nat. Mater.* **2009**, *8* (6), 500–506.

(61) Tachikawa, N.; Yamauchi, K.; Takashima, E.; Park, J.-W.; Dokko, K.; Watanabe, M. Reversibility of Electrochemical Reactions of Sulfur Supported on Inverse Opal Carbon in Glyme–Li Salt Molten Complex Electrolytes. *Chem. Commun.* **2011**, *47* (28), 8157.

(62) Guo, J.; Xu, Y.; Wang, C. Sulfur-Impregnated Disordered Carbon Nanotubes Cathode for Lithium–Sulfur Batteries. *Nano Lett.* **2011**, *11* (10), 4288–4294.

(63) Zheng, G.; Yang, Y.; Cha, J. J.; Hong, S. S.; Cui, Y. Hollow Carbon Nanofiber-Encapsulated Sulfur Cathodes for High Specific Capacity Rechargeable Lithium Batteries. *Nano Lett.* **2011**, *11* (10), 4462–4467.

(64) Wang, D.-W.; Zeng, Q.; Zhou, G.; Yin, L.; Li, F.; Cheng, H.-M.; Gentle, I. R.; Lu, G. Q. M. Carbon–sulfur Composites for Li–S Batteries: Status and Prospects. *J. Mater. Chem. A* **2013**, *1* (33), 9382.

(65) Liang, C.; Dudney, N. J.; Howe, J. Y. Hierarchically Structured Sulfur/Carbon Nanocomposite Material for High-Energy Lithium Battery. *Chem. Mater.* **2009**, *21* (19), 4724–4730.

(66) Helen, M.; Reddy, M. A.; Diemant, T.; Golla-Schindler, U.; Behm, R. J.; Kaiser, U.; Fichtner, M. Single Step Transformation of Sulphur to Li2S2/Li2S in Li-S Batteries. *Sci. Rep.* **2015**, *5*, 12146.

(67) Zhang, B.; Qin, X.; Li, G. R.; Gao, X. P. Enhancement of Long Stability of Sulfur Cathode by Encapsulating Sulfur into Micropores of Carbon Spheres. *Energy Environ. Sci.* **2010**, *3* (10), 1531–1537.

(68) Yin, Y. X.; Xin, S.; Guo, Y. G.; Wan, L. J. Lithium-Sulfur Batteries: Electrochemistry, Materials, and Prospects. *Angew. Chemie - Int. Ed.* **2013**, *52* (50), 13186–13200.

(69) Zhu, Q.; Zhao, Q.; An, Y.; Anasori, B.; Wang, H.; Xu, B. Ultra-Microporous Carbons Encapsulate Small Sulfur Molecules for High Performance Lithium-Sulfur Battery. *Nano Energy* **2017**, *33* (January), 402–409.

(70) Wang, Z.; Dong, Y.; Li, H.; Zhao, Z.; Wu, H. Bin; Hao, C.; Liu, S.; Qiu, J.; Lou, X. W. D. Enhancing Lithium-Sulphur Battery Performance by Strongly Binding the Discharge Products on Amino-Functionalized Reduced Graphene Oxide. *Nat. Commun.* **2014**, *5* (May 2014), 5002.

(71) Sun, Z.; Zhang, J.; Yin, L.; Hu, G.; Fang, R.; Cheng, H. M.; Li, F. Conductive Porous Vanadium Nitride/Graphene Composite as Chemical Anchor of Polysulfides for Lithium-Sulfur Batteries. *Nat. Commun.* **2017**, *8*, 1–8.

(72) Chen, T.; Ma, L.; Cheng, B.; Chen, R.; Hu, Y.; Zhu, G.; Wang, Y.; Liang, J.; Tie, Z.; Liu, J.; et al. Metallic and Polar Co 9 S 8 Inlaid Carbon Hollow Nanopolyhedra as Efficient Polysulfide Mediator for Lithium−sulfur Batteries. *Nano Energy* **2017**, *38* (February), 239–248.

(73) Seh, Z. W.; Zhang, Q.; Li, W.; Zheng, G.; Yao, H.; Cui, Y. Stable Cycling of Lithium Sulfide Cathodes through Strong Affinity with a Bifunctional Binder. *Chem. Sci.* **2013**, *4* (9), 3673.

(74) Ling, M.; Zhang, L.; Zheng, T.; Feng, J.; Guo, J.; Mai, L.; Liu, G. Nucleophilic Substitution between Polysulfides and Binders Unexpectedly Stabilizing Lithium Sulfur Battery. *Nano Energy* **2017**, *38* (March), 82–90.

(75) Lacey, M. J.; Jeschull, F.; Edström, K.; Brandell, D. Functional, Water-Soluble Binders for Improved Capacity and Stability of Lithium-Sulfur Batteries. *J. Power Sources* **2014**, *264*, 8–14.

(76) Zhang, S. S. Binder Based on Polyelectrolyte for High Capacity Density Lithium/Sulfur Battery. *J. Electrochem. Soc.* **2012**, *159* (8), A1226–A1229.

(77) Zheng, J.; Tian, J.; Wu, D.; Gu, M.; Xu, W.; Wang, C.; Gao, F.; Engelhard, M. H.; Zhang, J. G.; Liu, J.; et al. Lewis Acid-Base Interactions

between Polysulfides and Metal Organic Framework in Lithium Sulfur Batteries. *Nano Lett.* **2014**, *14* (5), 2345–2352.

(78) Demir-Cakan, R.; Morcrette, M.; Nouar, F.; Davoisne, C.; Devic, T.; Gonbeau, D.; Dominko, R.; Serre, C.; Férey, G.; Tarascon, J. M. Cathode Composites for Li-S Batteries via the Use of Oxygenated Porous Architectures. *J. Am. Chem. Soc.* **2011**, *133* (40), 16154–16160.

(79) Cui, Z.; Zu, C.; Zhou, W.; Manthiram, A.; Goodenough, J. B. Mesoporous Titanium Nitride-Enabled Highly Stable Lithium-Sulfur Batteries. *Adv. Mater.* **2016**, 6926–6931.

(80) Ye, C.; Zhang, L.; Guo, C.; Li, D.; Vasileff, A.; Wang, H.; Qiao, S. Z. A 3D Hybrid of Chemically Coupled Nickel Sulfide and Hollow Carbon Spheres for High Performance Lithium–Sulfur Batteries. *Adv. Funct. Mater.* **2017**, *27* (33), 1–9.

(81) Chen, T.; Zhang, Z.; Cheng, B.; Chen, R.; Hu, Y.; Ma, L.; Zhu, G.; Liu, J.; Jin, Z. Self-Templated Formation of Interlaced Carbon Nanotubes Threaded Hollow Co3S4Nanoboxes for High-Rate and Heat-Resistant Lithium-Sulfur Batteries. *J. Am. Chem. Soc.* **2017**, *139* (36), 12710–12715.

(82) Pang, Q.; Kundu, D.; Cuisinier, M.; Nazar, L. F. Surface-Enhanced Redox Chemistry of Polysulphides on a Metallic and Polar Host for Lithium-Sulphur Batteries. *Nat. Commun.* **2014**, *5* (May), 1–8.

(83) Liang, X.; Hart, C.; Pang, Q.; Garsuch, A.; Weiss, T.; Nazar, L. F. A Highly Efficient Polysulfide Mediator for Lithium-Sulfur Batteries. *Nat. Commun.* **2015**, *6*, 1–8.

(84) Li, Z.; Zhang, J.; Guan, B.; Wang, D.; Liu, L. M.; Lou, X. W. A Sulfur Host Based on Titanium Monoxide@carbon Hollow Spheres for Advanced Lithium-Sulfur Batteries. *Nat. Commun.* **2016**, *7*, 1–11.

(85) Xie, K.; You, Y.; Yuan, K.; Lu, W.; Zhang, K.; Xu, F.; Ye, M.; Ke, S.; Shen, C.; Zeng, X.; et al. Ferroelectric-Enhanced Polysulfide Trapping for Lithium–Sulfur Battery Improvement. *Adv. Mater.* **2017**, *29* (6).

(86) Wei, Y.; Kong, Z.; Pan, Y.; Cao, Y.; Long, D.; Wang, J.; Qiao, W.; Ling, L. Sulfur Film Sandwiched between Few-Layered MoS2electrocatalysts and Conductive Reduced Graphene Oxide as a Robust Cathode for Advanced Lithium-Sulfur Batteries. *J. Mater. Chem. A* **2018**, *6* (14), 5899–5909.

(87) Gao, J.; Lowe, M. A.; Kiya, Y.; Abruña, H. D. Effects of Liquid Electrolytes on the Charge-Discharge Performance of Rechargeable Lithium/Sulfur Batteries: Electrochemical and in-Situ X-Ray Absorption Spectroscopic Studies. *J. Phys. Chem. C* **2011**, *115* (50), 25132–25137.

(88) Barchasz, C.; Leprêtre, J. C.; Patoux, S.; Alloin, F. Electrochemical Properties of Ether-Based Electrolytes for Lithium/Sulfur Rechargeable Batteries. *Electrochim. Acta* **2013**, *89*, 737–743.

(89) Barghamadi, M.; Best, A. S.; Bhatt, A. I.; Hollenkamp, A. F.; Musameh, M.; Rees, R. J.; Rüther, T. Lithium-Sulfur Batteries - The Solution Is in the Electrolyte, but Is the Electrolyte a Solution? *Energy Environ. Sci.* **2014**, *7* (12), 3902–3920.

(90) Scheers, J.; Fantini, S.; Johansson, P. A Review of Electrolytes for Lithium–sulphur Batteries. *J. Power Sources* **2014**, *255*, 204–218.

(91) Rauh, R. D.; Abraham, K. M.; Pearson, G. F.; Surprenant, J. K.; Brummer, S. B.; Corporation,

E. I. C. A Lithium / Dissolved Sulfur Battery with an Organic Electrolyte. *J. Electrochem. Soc.* **1979**, *126*, 523–527.

(92) Yim, T.; Park, M.-S.; Yu, J.-S.; Kim, K. J.; Im, K. Y.; Kim, J.-H.; Jeong, G.; Jo, Y. N.; Woo, S.-G.; Kang, K. S.; et al. Effect of Chemical Reactivity of Polysulfide toward Carbonate-Based Electrolyte on the Electrochemical Performance of Li–S Batteries. *Electrochim. Acta* **2013**, *107*, 454–460.

(93) Tobishima, S. I.; Yamamoto, H.; Matsuda, M. Study on the Reduction Species of Sulfur by Alkali Metals in Nonaqueous Solvents. *Electrochim. Acta* **1997**, *42* (6), 1019–1029.

(94) Shim, J.; Striebel, K. A.; Cairns, E. J. The Lithium/Sulfur Rechargeable Cell. *J. Electrochem. Soc.* **2002**, *149* (10), A1321.

(95) Marmorstein, D.; Yu, T. H.; Striebel, K. A.; Mclarnon, F. R.; Hou, J.; Cairns, E. J. Electrochemical Performance of Lithiumrsulfur Cells with Three Different Polymer Electrolytes. *J. Power Sources* **2000**, *89*, 219–226.

(96) Peled, E. Lithium-Sulfur Battery: Evaluation of Dioxolane-Based Electrolytes. *J. Electrochem. Soc.* **1989**, *136* (6), 1621.

(97) Wang, W.; Wang, Y.; Huang, Y.; Huang, C.; Yu, Z.; Zhang, H.; Wang, A.; Yuan, K. The Electrochemical Performance of Lithium–sulfur Batteries with LiClO4 DOL/DME Electrolyte. *J. Appl. Electrochem.* **2010**, *40* (2), 321–325.

(98) Aurbach, D. Review of Selected Electrode-Solution Interactions Which Determine the Performance of Li and Li Ion Batteries. *J. Power Sources* **2000**, *89* (2), 206–218.

(99) Gao, J.; Lowe, M. A.; Kiya, Y.; Abruna, H. D. Effects of Liquid Electrolytes on the Charge-Discharge Performance of Rechargeable Lithium/Sulfur Batteries: Electrochemical and in-Situ X-Ray Absorption Spectroscopic Studies. *J. Phys. Chem. C* **2011**, *115* (50), 25132–25137.

(100) Kim, H. S.; Jeong, C. S. Electrochemical Properties of Binary Electrolytes for Lithium-Sulfur Batteries. *Bull. Korean Chem. Soc.* **2011**, *32* (10), 3682–3686.

(101) Liang, X.; Wen, Z.; Liu, Y.; Wu, M.; Jin, J.; Zhang, H.; Wu, X. Improved Cycling Performances of Lithium Sulfur Batteries with LiNO 3-Modified Electrolyte. *J. Power Sources* **2011**, *196* (22), 9839–9843.

(102) Lin, Z.; Liu, Z.; Fu, W.; Dudney, N. J.; Liang, C. Phosphorous Pentasulfide as a Novel Additive for High-Performance Lithium-Sulfur Batteries. *Adv. Funct. Mater.* **2013**, *23* (8), 1064–1069.

(103) Wu, F.; Lee, J. T.; Nitta, N.; Kim, H.; Borodin, O.; Yushin, G. Lithium Iodide as a Promising Electrolyte Additive for Lithium-Sulfur Batteries: Mechanisms of Performance Enhancement. *Adv. Mater.* **2015**, *27* (1), 101–108.

(104) Zhang, S. S. Role of LiNO3 in Rechargeable Lithium/Sulfur Battery. *Electrochim. Acta* **2012**, *70*, 344–348.

(105) Aurbach, D.; Pollak, E.; Elazari, R.; Salitra, G.; Kelley, C. S.; Affinito, J. On the Surface Chemical Aspects of Very High Energy Density, Rechargeable Li–Sulfur Batteries. *J. Electrochem. Soc.* **2009**, *156* (8), A694.

(106) Xiong, S.; Xie, K.; Diao, Y.; Hong, X. Properties of Surface Film on Lithium Anode with LiNO3as Lithium Salt in Electrolyte Solution for Lithium-Sulfur Batteries. *Electrochim. Acta* **2012**, *83*, 78–86.

(107) Zhang, S. S. Effect of Discharge Cutoff Voltage on Reversibility of Lithium/Sulfur Batteries with LiNO3-Contained Electrolyte. *J. Electrochem. Soc.* **2012**, *159* (7), A920–A923.

(108) Li, M.; Chen, Z.; Wu, T.; Lu, J. Li_2S- or S-Based Lithium-Ion Batteries. *Adv. Mater.* **2018**, *1801190*, 1801190.

(109) Yang, Y.; Zheng, G.; Misra, S.; Nelson, J.; Toney, M. F.; Cui, Y. High-Capacity Micrometer-Sized Li2S Particles as Cathode Materials for Advanced Rechargeable Lithium-Ion Batteries. *J. Am. Chem. Soc.* **2012**, *134* (37), 15387–15394.

(110) Zhang, K.; Wang, L.; Hu, Z.; Cheng, F.; Chen, J. Ultrasmall Li2S Nanoparticles Anchored in Graphene Nanosheets for High-Energy Lithium-Ion Batteries. *Sci. Rep.* **2014**, *4*, 6467.

(111) Cheng, X.-B.; Huang, J.-Q.; Zhang, Q. Review—Li Metal Anode in Working Lithium-Sulfur Batteries. *J. Electrochem. Soc.* **2018**, *165* (1), A6058–A6072.

(112) Cheng, X. B.; Zhang, R.; Zhao, C. Z.; Zhang, Q. Toward Safe Lithium Metal Anode in Rechargeable Batteries: A Review. *Chem. Rev.* **2017**, *117* (15), 10403–10473.

(113) Nitta, N.; Wu, F.; Lee, J. T.; Yushin, G.; Cheng, X.-B.; Zhang, R.; Zhao, C.-Z.; Wei, F.; Zhang, J. J.-G. G.; Zhang, Q.; et al. Dendrite-Free Lithium Metal Anodes: Stable Solid Electrolyte Interphase for High-Efficiency Batteries. *J. Electrochem. Soc.* **2015**, *3* (3), 7207–7209.

(114) Cheng, X. B.; Zhang, R.; Zhao, C. Z.; Wei, F.; Zhang, J. G.; Zhang, Q. A Review of Solid Electrolyte Interphases on Lithium Metal Anode. *Adv. Sci.* **2015**, *3* (3), 1–20.

(115) Li, Z.; Huang, J.; Yann Liaw, B.; Metzler, V.; Zhang, J. A Review of Lithium Deposition in Lithium-Ion and Lithium Metal Secondary Batteries. *J. Power Sources* **2014**, *254*, 168–182.

(116) Son, Y.; Lee, J.-S.; Son, Y.; Jang, J.-H.; Cho, J. Recent Advances in Lithium Sulfide Cathode Materials and Their Use in Lithium Sulfur Batteries. *Adv. Energy Mater.* **2015**, *5* (16), 1500110.

(117) Lee, S. K.; Lee, Y. J.; Sun, Y. K. Nanostructured Lithium Sulfide Materials for Lithium-Sulfur Batteries. *J. Power Sources* **2016**, *323*, 174–188.

(118) Miao, R.; Yang, J.; Xu, Z.; Wang, J.; Nuli, Y.; Sun, L. A New Ether-Based Electrolyte for Dendrite-Free Lithium-Metal Based Rechargeable Batteries. *Sci. Rep.* **2016**, *6* (February), 2–10.

(119) Cai, K.; Song, M. K.; Cairns, E. J.; Zhang, Y. Nanostructured Li2S-C Composites as Cathode Material for High-Energy Lithium/Sulfur Batteries. *Nano Lett.* **2012**, *12* (12), 6474–6479.

(120) Hwa, Y.; Zhao, J.; Cairns, E. J. Lithium Sulfide (Li_2S)/Graphene Oxide Nanospheres with Conformal Carbon Coating as a High-Rate, Long-Life Cathode for Li/S Cells. *Nano Lett.* **2015**, *15* (5), 3479–3486.

(121) Nan, C.; Lin, Z.; Liao, H.; Song, M. K.; Li, Y.; Cairns, E. J. Durable Carbon-Coated Li2S Core-Shell Spheres for High Performance Lithium/Sulfur Cells. *J. Am. Chem. Soc.* **2014**, *136* (12), 4659–4663.

(122) Wu, F.; Kim, H.; Magasinski, A.; Lee, J. T.; Lin, H. T.; Yushin, G. Harnessing Steric Separation of Freshly Nucleated Li2S Nanoparticles for Bottom-up Assembly of High-Performance Cathodes for Lithium-Sulfur and Lithium-Ion Batteries. *Adv. Energy Mater.* **2014**, *4* (11), 1–7.

(123) Meini, S.; Elazari, R.; Rosenman, A.; Garsuch,

A.; Aurbach, D. The Use of Redox Mediators for Enhancing Utilization of Li2S Cathodes for Advanced Li-S Battery Systems. *J. Phys. Chem. Lett.* **2014**, *5* (5), 915–918.

(124) Bard, A. J.; Faulkner, L. R. *Electrochemical Methods: Fundamentals and Applications*; Wiley, 2001.

(125) Helmholtz, H. Ueber Einige Gesetze Der Vertheilung Elektrischer Ströme in Körperlichen Leitern Mit Anwendung Auf Die Thierisch-Elektrischen Versuche. *Ann. der Phys. und Chemie* **1853**, *165* (6), 211–233.

(126) Warburg, E. Ueber Das Verhalten Sogenannter Unpolarisirbarer Elektroden Gegen Wechselstrom. *Ann. der Phys. und Chemie* **1899**, *303* (3), 493–499.

(127) Tsividis, Y.; Milios, J. A Detailed Look at Electrical Equivalents of Uniform Electrochemical Diffusion Using Nonuniform Resistance-Capacitance Ladders. *J. Electroanal. Chem.* **2013**, *707*, 156–165.

(128) Randles, J. E. B. Kinetics of Rapid Electrode Reactions. *Discuss. Faraday Soc.* **1947**, *1*, 11.

(129) Bai, L.; Conway, B. E. AC Impedance of Faradaic Reactions Involving Electrosorbed Intermediates: Examination of Conditions Leading to Pseudoinductive Behavior Represented in Three-Dimensional Impedance Spectroscopy Diagrams. *J. Electrochem. Soc.* **1991**, *138* (10), 2897.

(130) Díaz, S. L.; Calderón, J. A.; Barcia, O. E.; Mattos, O. R. Electrodeposition of Iron in Sulphate Solutions. *Electrochim. Acta* **2008**, *53* (25), 7426–7435.

(131) Orazem, M. E.; Tribollet, B. *Electrochemical Impedance Spectroscopy*; 2008.

(132) Barsoukov, E.; Macdonald, J. R. *Impedance Spectroscopy Theory, Experiment, and Applications*, Second Edi.; Wiley, 2005.

(133) Long, D. A. *The Raman Effect - A Unified Treatment of the Theory of Raman Scattering by Molecules*; Wiley, 2002.

(134) Watts, J. F.; Wolstenholme, J. *An Introduction to Surface Analysis by XPS and AES*; Wiley, 2003.

(135) Goldstein, J. I. *Scanning Electron Microscopy and X-Ray Microanalysis*, Third Edit.; Springer, 2007.

(136) Dinnebier, R. E. *Powder Diffraction : Theory and Practice*; Royal Society of Chemistry, 2008.

(137) Pavia, D. L.; Lampman, G. M.; Kriz, G. S.; Vyvyan, J. R. *Introduction to Spectroscopy*, Fourth Edi.; 2009.

(138) Skoog, D. A. *Fundamentals of Analytical Chemistry*, Ninth Edit.; 2014.

(139) McCloskey, B. D.; Bethune, D. S.; Shelby, R. M.; Girishkumar, G.; Luntz, A. C. Solvents' Critical Role in Nonaqueous Lithium–Oxygen Battery Electrochemistry. *J. Phys. Chem. Lett.* **2011**, *2* (10), 1161–1166.

(140) Christensen, J.; Albertus, P.; Sanchez-Carrera, R. S.; Lohmann, T.; Kozinsky, B.; Liedtke, R.; Ahmed, J.; Kojic, A. A Critical Review of Li/Air Batteries. *J. Electrochem. Soc.* **2012**, *159* (2), R1.

(141) Imanishi, N.; Yamamoto, O. Rechargeable Lithium-Air Batteries: Characteristics and Prospects. *Mater. Today* **2014**, *17* (1), 24–30.

(142) Freunberger, S. A.; Chen, Y.; Drewett, N. E.; Hardwick, L. J.; Bardé, F.; Bruce, P. G. The Lithium-Oxygen Battery with Ether-Based Electrolytes. *Angew. Chemie Int. Ed.* **2011**, *50* (37), 8609–8613.

(143) Mc Murry, J. Ester Cleavages via S N 2-Type

Dealkylation. In *Organic Reactions*; John Wiley & Sons, Inc.: Hoboken, NJ, USA, 2011; Vol. 24, pp 187–224.

(144) Yoshida, H.; Matsuura, H. Density Functional Study of the Conformations and Vibrations of 1, 2-Dimethoxyethane. *J. Phys. Chem. A* **1998**, *102* (16), 2691–2699.

(145) Makarewicz, J.; Ha, T. Ab Initio Study of the Pseudorotation in 1,3-Dioxolane. *J. Mol. Struct.* **2001**, *599* (1–3), 271–278.

(146) Read, J. Characterization of the Lithium/Oxygen Organic Electrolyte Battery. *J. Electrochem. Soc.* **2002**, *149* (9), A1190–A1195.

(147) Berman, Y. L.; Lyudvig, Y. B.; Ponomarenko, V. A.; Medvedev, S. S. Mechanism of the Polymerization of 1,3-Dioxolane. *Polym. Sci. U.S.S.R.* **1969**, *11* (1), 225–231.

(148) Okada, M.; Yamashita, Y.; Ishii, Y. Polymerization of 1,3-Dioxolane. *Makromolekulare* **1964**, 196.

(149) Bailey, W. J. Free Radical Ring-Opening Polymerization. *Die Makromol. Chemie* **1985**, *13* (S19851), 171–190.

(150) Zambonin, P. G. Oxide Chemistry and Electroreduction of NO3− in Molten Alkali Nitrates. *J. Electroanal. Chem. Interfacial Electrochem.* **1970**, *24* (2–3), 365–377.

(151) Yang, Y.; Mikeš, F.; Okamoto, Y. Polymerization of Cyclic Acetals by a Free Radical Initiator, Perfluorodibenzoyl Peroxide, in the Presence of Oxygen. *Macromolecules* **2005**, *38* (14), 5841–5843.

(152) Aurbach, D.; Youngman, O.; Dan, P. The Electrochemical Behavior of 1,3-Dioxolane—LiClO4 Solutions—II. Contaminated Solutions. *Electrochim. Acta* **1990**, *35* (3), 639–655.

(153) Aurbach, D.; Pollak, E.; Elazari, R.; Salitra, G.; Kelley, C. S.; Affinito, J. On the Surface Chemical Aspects of Very High Energy Density, Rechargeable Li–Sulfur Batteries. *J. Electrochem. Soc.* **2009**, *156* (8), A694.

(154) Chang, D. R.; Lee, S. H.; Kim, S. W.; Kim, H. T. Binary Electrolyte Based on Tetra(Ethylene Glycol) Dimethyl Ether and 1,3-Dioxolane for Lithium-Sulfur Battery. *J. Power Sources* **2002**, *112* (2), 452–460.

(155) Ganesan, A.; Varzi, A.; Passerini, S.; Shaijumon, M. M. Graphene Derived Carbon Confined Sulfur Cathodes for Lithium-Sulfur Batteries: Electrochemical Impedance Studies. *Electrochim. Acta* **2016**, *214*, 129–138.

(156) Siriwardane, R. V.; Cook, J. M. Interactions of SO2 with Sodium Deposited on CaO. *J. Colloid Interface Sci.* **1986**, *114* (2), 525–535.

(157) Diao, Y.; Xie, K.; Xiong, S.; Hong, X. Insights into Li-S Battery Cathode Capacity Fading Mechanisms: Irreversible Oxidation of Active Mass during Cycling. *J. Electrochem. Soc.* **2012**, *159* (11), A1816–A1821.

(158) Manocha, A. S.; Park, R. L. Flotation Related ESCA Studies on PbS Surfaces. *Appl. Surf. Sci.* **1977**, *1* (1), 129–141.

(159) Carroll, T. X.; Ji, D.; Maclaren, D. C.; Thomas, T. D.; Saethre, L. J. Relativistic Corrections to Reported Sulfur 1s Ionization Energies. *J. Electron Spectros. Relat. Phenomena* **1987**, *42* (3), 281–284.

(160) Sun, B.; Xu, C.; Mindemark, J.; Gustafsson, T.; Edström, K.; Brandell, D. At the Polymer Electrolyte Interfaces: The Role of the Polymer Host in Interphase Layer Formation in Li-Batteries. *J. Mater. Chem. A* **2015**, *3* (26),

13994–14000.

(161) Clark, D. T.; Feast, W. J.; Kilcast, D.; Musgrave, W. K. R. Applications of ESCA to Polymer Chemistry. III. Structures and Bonding in Homopolymers of Ethylene and the Fluoroethylenes and Determination of the Compositions of Fluoro Copolymers. *J. Polym. Sci. Polym. Chem. Ed.* **1973**, *11* (2), 389–411.

(162) Ryu, H. S.; Ahn, H. J.; Kim, K. W.; Ahn, J. H.; Cho, K. K.; Nam, T. H.; Kim, J. U.; Cho, G. B. Discharge Behavior of Lithium/Sulfur Cell with TEGDME Based Electrolyte at Low Temperature. *J. Power Sources* **2006**, *163* (1 SPEC. ISS.), 201–206.

(163) Fulvio, P. F.; Lee, J. S.; Mayes, R. T.; Wang, X.; Mahurin, S. M.; Dai, S. Boron and Nitrogen-Rich Carbons from Ionic Liquid Precursors with Tailorable Surface Properties. *Phys. Chem. Chem. Phys.* **2011**, *13* (30), 13486–13491.

(164) Guo, B.; Sun, X. G.; Veith, G. M.; Bi, Z.; Mahurin, S. M.; Liao, C.; Bridges, C.; Paranthaman, M. P.; Dai, S. Nitrogen-Enriched Carbons from Alkali Salts with High Coulombic Efficiency for Energy Storage Applications. *Adv. Energy Mater.* **2013**, *3* (6), 708–712.

(165) Davis, R. E.; Nakshbendi, H. F. Sulfur in Amine Solvents. *J. Am. Chem. Soc.* **1962**, *84* (11), 2085–2090.

(166) MacColl, R.; Windwer, S. Spectroscopy of Sulfur in Ethylenediamine. *J. Phys. Chem.* **1970**, *74* (6), 1261–1266.

(167) Giorgini, M. G.; Pelletti, M. R.; Paliani, G.; Cataliotti, R. S. Vibrational Spectra and Assignments of Ethylene-Diamine and Its Deuterated Derivatives. *J. Raman Spectrosc.* **1983**, *14* (1), 16–21.

(168) Woodward, P.; Clarke, A.; Greenland, B. W.; Hermida Merino, D.; Yates, L.; Slark, A. T.; Miravet, J. F.; Hayes, W. Facile Bisurethane Supramolecular Polymers Containing Flexible Alicyclic Receptor Units. *Soft Matter* **2009**, *5* (10), 2000–2010.

(169) Kiefer, J.; Noack, K.; Penna, T. C.; Ribeiro, M. C. C.; Weber, H.; Kirchner, B. Vibrational Signatures of Anionic Cyano Groups in Imidazolium Ionic Liquids. *Vib. Spectrosc.* **2017**, *91*, 141–146.

(170) Mao, J. X.; Nulwala, H. B.; Luebke, D. R.; Damodaran, K. Spectroscopic and Computational Analysis of the Molecular Interactions in the Ionic Liquid Ion Pair [BMP] +[TFSI] -. *J. Mol. Liq.* **2012**, *175*, 141–147.

(171) Finger, L. H.; Wohde, F.; Grigoryev, E. I.; Hansmann, A.-K.; Berger, R.; Roling, B.; Sundermeyer, J. Access to Pure and Highly Volatile Hydrochalcogenide Ionic Liquids. *Chem. Commun.* **2015**, *51* (90), 16169–16172.

(172) *CRC Handbook of Chemistry and Physics - 95th Edition*; 2014.

(173) Kang, E. T.; Neoh, K. G.; Zhang, X.; Tan, K. L.; Liaw, D. J. Surface Modification of Electroactive Polymer Films by Ozone Treatment. *Surf. Interface Anal.* **1996**, *24* (1), 51–58.

(174) Tan, K. L.; Tan, B. T. G.; Kang, E. T.; Neoh, K. G. X-Ray Photoelectron Spectroscopy Studies of the Chemical Structure of Polyaniline. *Phys. Rev. B* **1989**, *39* (11), 8070–8073.

(175) Ferrari, A. C. Raman Spectroscopy of Graphene and Graphite: Disorder, Electron–phonon Coupling, Doping and Nonadiabatic Effects. *Solid State Commun.* **2007**, *143* (1–2), 47–57.

(176) Zaghib, K.; Julien, C. M.; Prakash, J. New

Trends in Intercalation Compounds for Energy Storage and Conversion. In *New Trends in Intercalation Compounds for Energy Storage and Conversion*; 2003; pp 110–112.

(177) Blint, R. J. Binding of Ether and Carbonyl Oxygens to Lithium Ion. *J. Electrochem. Soc.* **1995**, *142* (3), 696–702.

(178) Xu, R.; Lu, J.; Amine, K. Progress in Mechanistic Understanding and Characterization Techniques of Li-S Batteries. *Adv. Energy Mater.* **2015**, n/a-n/a.

(179) Song, J. Y.; Lee, H. H.; Wang, Y. Y.; Wan, C. C. Two- and Three-Electrode Impedance Spectroscopy of Lithium-Ion Batteries. *J. Power Sources* **2002**, *111* (2), 255–267.

(180) Boukamp, B. A. Interpretation of an "inductive Loop" in the Impedance of an Oxygen Ion Conducting Electrolyte/Metal Electrode System. *Solid State Ionics* **2001**, *143* (1), 47–55.

(181) Chen, C.-F.; Mistry, A.; Mukherjee, P. P. Probing Impedance and Microstructure Evolution in Lithium–Sulfur Battery Electrodes. *J. Phys. Chem. C* **2017**, *121* (39), 21206–21216.

(182) Deng, Z.; Zhang, Z.; Lai, Y.; Liu, J.; Li, J.; Liu, Y. Electrochemical Impedance Spectroscopy Study of a Lithium/Sulfur Battery: Modeling and Analysis of Capacity Fading. *J. Electrochem. Soc.* **2013**, *160* (4), A553–A558.

(183) Ca??as, N. A.; Hirose, K.; Pascucci, B.; Wagner, N.; Friedrich, K. A.; Hiesgen, R. Investigations of Lithium-Sulfur Batteries Using Electrochemical Impedance Spectroscopy. *Electrochim. Acta* **2013**, *97*, 42–51.

(184) Noh, H.; Song, J.; Park, J.-K.; Kim, H.-T. A New Insight on Capacity Fading of Lithium–sulfur Batteries: The Effect of Li2S Phase Structure. *J. Power Sources* **2015**, *293*, 329–335.

Acknowledgements

First and foremost, I would like to express my sincerest gratitude to Prof. Dr. Passerini, for accepting me as a PhD candidate and mentoring me during my stay in the Helmholtz Institut Ulm. Without his knowledge, wisdom, and trust on me, I would not be able to finish this work. I take this opportunity to also show my gratitude to Prof. Dr. Helmut Ehrenberg for accepting to be my co-advisor, and the other members of examiners board, for agreeing to evaluate this work. I am also grateful for the financial support of the Science without Borders program, which allowed this work to be realized.

Dr. Alberto Varzi receives my sincerest appreciation for generously helping me with his hands-on knowledge as well as his time, in the form of many fruitful discussions and recommendations. This sentiment extends to all my co-workers in HIU, who assisted this work both professionally and personally, in particular Dr. Varvara Sharova, Dr. Marlou Keller, and Peter Ruschhaupt.

I am grateful for the support of Dr. Vitor Leite Martins, who, despite the many miles, still sits beside me. I also thank Professors Roberto and Susana Torresi, and dedicate this thesis to the memory of Professor Paulo Teng An Sumodjo, for their importance in my formative years as an electrochemist.

Finally, I would like to thank my family and friends, who helped shape who I am today, and whose backing were paramount to make this journey easier. In special, I thank my parents, Mauro and Angela, my brother Cesar, and my relatives Regina, Wilson, Gabriel, Ricardo, and Andre.